

Surface Science Studies on the Adsorption and Reaction of Small Molecules on Rhodium(111) and Two-Dimensional Materials

* * *

Oberflächenwissenschaftliche Untersuchungen der
Adsorption und Reaktion von kleinen Molekülen
auf Rhodium(111) und Zweidimensionalen Materialien

Der Naturwissenschaftlichen Fakultät
der Friedrich-Alexander-Universität Erlangen-Nürnberg
zur Erlangung des Doktorgrades Dr. rer. nat.

vorgelegt von

EVA MARIE FREIBERGER

Als Dissertation genehmigt
von der Naturwissenschaftlichen Fakultät
der Friedrich-Alexander-Universität Erlangen-Nürnberg

Tag der mündlichen Prüfung: 12.07.2024

Gutachter: Prof. Dr. Christian Papp
Prof. Dr. Andreas Görling

Table of Contents

| | | |
|----------|--|-----------|
| 1 | Introduction | 1 |
| 1.1 | Surface Science | 1 |
| 1.2 | Adsorption of Small Molecules and Model Catalysis | 2 |
| 1.3 | 2D Materials: Growth, Properties and Chemical Modification..... | 5 |
| 2 | Fundamentals | 11 |
| 2.1 | Synchrotron Radiation | 11 |
| 2.2 | X-Ray Photoelectron Spectroscopy | 15 |
| 2.3 | Near-Edge X-Ray Absorption Fine Structure | 22 |
| 2.4 | Low-Energy Electron Diffraction..... | 26 |
| 3 | Experimental | 30 |
| 3.1 | Experimental Setup | 30 |
| 3.2 | Data Acquisition and Processing..... | 32 |
| 3.3 | “ARPES Chamber” | 33 |
| 4 | The Surface Chemistry of Small Molecules on Rh(111) | 37 |
| 4.1 | A High-Resolution X-Ray Photoelectron Spectroscopy Study on the Adsorption and Reaction of Ethylene on Rh(111) [P1]..... | 37 |
| 4.2 | <i>h</i> -BN in the Making: The Surface Chemistry of Borazine on Rh(111) [P2]..... | 40 |
| 4.3 | Bromine Adsorption and Thermal Stability on Rh(111): A Combined XPS, LEED and DFT Study [P3] | 43 |
| 5 | Bromination of 2D Materials [P4] | 48 |
| 6 | Summary and Outlook | 54 |

| | | |
|----|--|----|
| 7 | Zusammenfassung und Ausblick | 58 |
| 8 | Bibliography | 63 |
| 9 | Danksagung..... | 75 |
| 10 | List of Publications..... | 77 |
| | Appendix A: Full Articles [P1] – [P4]..... | A1 |
| | Appendix B: Technical Drawings | B1 |

Abbreviations

| | |
|--------------------|---|
| 2D | Two-dimensional |
| 2DM | Two-dimensional material |
| AES | Auger electron spectroscopy |
| AEY | Auger electron yield |
| AFM | Atomic force microscopy |
| ARPES | Angle-resolved photoemission spectroscopy |
| BESSY II | Berliner Elektronenspeicherring-Gesellschaft für Synchrotronstrahlung II |
| CVD | Chemical vapor deposition |
| DFT | Density functional theory |
| EXAFS | Extended X-ray absorption fine structure |
| GI | Grazing incidence |
| <i>h</i>-BN | Hexagonal boron nitride |
| HOMO | Highest occupied molecular orbital |
| HREELS | High-resolution electron energy loss spectroscopy |
| HZB | Helmholtz-Zentrum Berlin für Materialien und Energie |
| IP | Ionization potential |
| IRRAS | Infrared reflection absorption spectroscopy |
| LEED | Low-energy electron spectroscopy |
| LINAC | Linear accelerator |
| LOHC | Liquid organic hydrogen carrier |
| LUMO | Lowest unoccupied molecular orbital |

| | |
|---------------|---|
| MD | Molecular dynamics |
| ML | Monolayer |
| NEXAFS | Near-edge X-ray absorption fine structure |
| NI | Normal incidence |
| PED | Photoelectron diffraction |
| PES | Photoemission spectroscopy |
| PEY | Partial electron yield |
| PVD | Physical vapor deposition |
| QCM | Quartz crystal microbalance |
| QMS | Quadrupole mass spectrometer |
| STM | Scanning tunneling microscopy |
| RF | Radio frequency |
| TEY | Total electron yield |
| TPD | Temperature-programmed desorption |
| TPXPS | Temperature-programmed X-ray photoelectron spectroscopy |
| UHV | Ultra-high vacuum |
| UPS | Ultraviolet photoelectron spectroscopy |
| UV | Ultraviolet |
| XANES | X-ray absorption near-edge spectroscopy |
| XAS | X-ray absorption spectroscopy |
| XPS | X-ray photoelectron spectroscopy |
| XRF | X-ray fluorescence |

1 Introduction

1.1 Surface Science

The beauty of surface science is that complicated systems can be simplified to such degree that it becomes possible to elucidate chemical, physical, mechanical, magnetic and optical surface phenomena on the molecular level.[1,2] For example, surface science allows for the detailed investigation of the adsorption and reaction of atoms and molecules on metals, which is a promising strategy to further our understanding of real-world industrial processes. To reduce complexity, defined low-index single-crystal surfaces are popular substrates since defects can lead to severe changes of the surface chemistry of adsorbed species. Moreover, surface science is mostly performed under ultra-high vacuum (UHV) conditions, which provide an almost contaminant-free environment to avoid undesired influences and side reactions. This enables the unadulterated investigation of surfaces and surface adsorbates.

Nowadays, a plethora of modern surface science techniques is available, including spectroscopic methods, such as photoemission spectroscopy (PES) and infrared reflection absorption spectroscopy (IRRAS), microscopic tools, such as scanning tunneling microscopy (STM) and atomic force microscopy (AFM), and diffraction techniques, such as low-energy electron diffraction (LEED) and photoelectron diffraction (PED).[1,3,4] By means of these techniques, information about adsorption-induced surface phenomena, e.g., restructuring and poisoning, and the characteristics of the adsorbate can be obtained. The latter include, *inter alia*, the chemical identity of surface species, adsorption geometries, adsorption sites, structural periodicity, thermal stabilities and reaction pathways. A profound understanding in this regard is of fundamental importance for any surface-related process; only with this knowledge at hand, the improvement of established industrial processes and the purposeful design of new applications can be achieved. This rational strategy may replace the widespread, cost- and time-consuming “trial and error” approach, e.g., in the context of the development of new heterogeneous

catalysts. Figure 1 illustrates a conventional surface science experiment, including sample cleaning, adsorption, characterization of the respective surface species and possible subsequent modification or reaction.

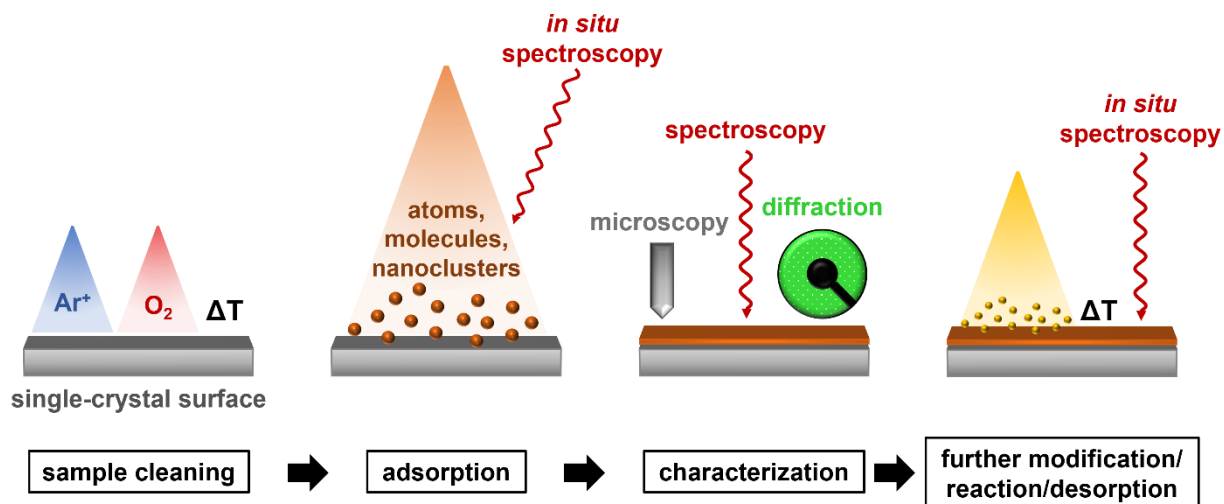


Figure 1. Illustration of the typical steps constituting a standard surface science experiment.

Due to the advanced vacuum technology and the sophisticated analytical techniques required, surface science, however, appears to be very demanding. Nevertheless, the experienced researcher willingly undertakes these efforts as he/she will be rewarded a fundamental understanding of surface-related processes, which are often not accessible for investigation under ambient conditions. Consequently, surface science plays an essential role in various research fields, providing valuable insights into, for example, heterogeneous catalysis [1,5-11], electrochemistry [12-14], energy storage [15-18] and the preparation of new nanostructures and low-dimensional materials (on-surface synthesis) [19-26].

1.2 Adsorption of Small Molecules and Model Catalysis

Hydrocarbons play a significant role in many industrial processes, e.g., as feedstock for the chemical industry or as energy materials. Their synthesis and further processing often rely on heterogeneous catalysis, in which predominantly noble metals, such as platinum, palladium, rhodium and iridium, act as catalytically active compound. Unfortunately, the mechanistic details of heterogeneous catalysis are so far still insufficiently

investigated. In this context, the undesired coking of the catalyst, that is, its deactivation due to accumulation of carbidic species on the catalyst's surface, is a major issue, which must be prevented for efficient catalysis.[27] To grasp a deeper understanding of heterogeneous catalysis, in particular of the interplay between adsorbate and catalytically active metal, the adsorption and reaction of hydrocarbons and other small molecules on single crystal surfaces are studied by means of surface science (Figure 1). Such model catalytic studies have, for example, addressed the chemistry of methane and ethylene on Pt(111) [28], of SO₂ on clean and oxygen pre-covered Pt(111) [29] and of ethylene on Rh(111) [30], with the latter being part of this dissertation (Chapter 4.1). Also, larger molecules, such as liquid organic hydrogen carriers (LOHCs) [15,31-35] and molecular solar thermal energy storage systems [18,36,37] were investigated in the scope of surface science-based model catalysis. These rather simple reference systems pave the way for more complex catalytic approaches with the overall aim of a knowledge-driven design of heterogeneous catalysts.[38]

Chemistry on metal supports also opens up new avenues for synthetic chemists. In so-called on-surface synthesis, the self-assembly and controlled reaction of suitable precursor molecules shows great potential for the production of low-dimensional materials. The deposition of ethylene and borazine on hot, catalytically active metal substrates, for example, enables the preparation of supported graphene and hexagonal boron nitride (*h*-BN). This method is referred to as chemical vapor deposition (CVD) and represents an easy and versatile route towards the synthesis of high-quality two-dimensional materials (2DMs). In Figure 2, the CVD growth of metal-supported *h*-BN is visualized. Successful CVD growth of graphene and *h*-BN was performed on various metal surfaces, such as Pt(111) [39,40], Ni(111) [41,42], Pd(111) [43,44], Rh(111) [45,46], Ir(111) [47,48], Ru(0001) [49-51] and Cu(111) [52,53]. Our study on the surface chemistry of borazine on Rh(111) [54], which is discussed within the scope of this dissertation (Chapter 4.2), sheds light on the mechanistic details of the evolution of *h*-BN from borazine on the molecular level.

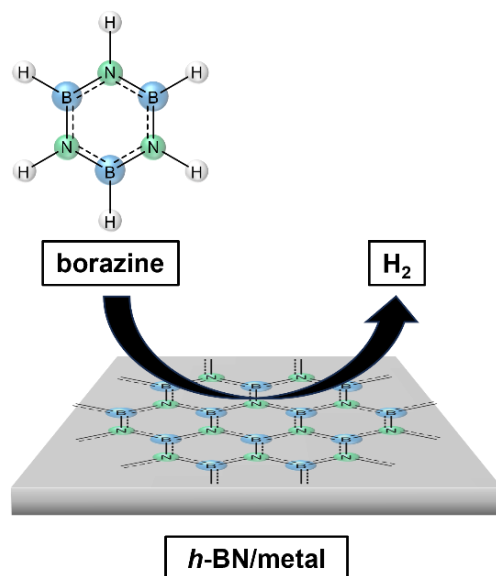


Figure 2. Illustration of the CVD growth of *h*-BN on a hot metal substrate using borazine as precursor.

Other small molecules that are quite important as common reactants and/or by-products in numerous chemical processes are halogens (Cl₂, Br₂ and I₂). In on-surface synthesis, several reactions used to build up larger nanostructures, e.g., Ullman coupling, result in halogen atoms as by-product, which might accumulate on the surface and thereby hinder proper propagation of the coupling reaction.[23,55-58] Similarly, in electrochemistry, the adsorption of halogen atoms from the electrolyte at the electrodes may influence their performance.[59-64] Furthermore, halogens are, for example, used as promoters in the silver-catalyzed epoxidation of ethylene.[65-68] Taking this ubiquity of halogens into consideration, it is evident that a detailed understanding of the role of halogens in surface-related processes is required. Also in this case, surface science is the method of choice as it provides a deep insight into the adsorption and thermal stability of halogens on metal surfaces. Consequently, many studies on this topic have already been published. The adsorption of bromine was investigated on Pt(111) [69], Pd(111) [70], Cu(111) [71], Ni(110) [72] and Ag(111) [73]. We contribute to this research by a thorough investigation of bromine on Rh(111) [74], which is addressed in Chapter 4.3 of this dissertation.

1.3 2D Materials: Growth, Properties and Chemical Modification

In 2004, Novoselov and Geim were the first to isolate graphene, a two-dimensional (2D) layer built up from sp^2 -hybridized carbon atoms arranged in a honeycomb fashion, for which they were awarded the 2010 Nobel prize in Physics.[75,76] This marked the dawn of a new era in materials research. The zero-bandgap semiconductor graphene exhibits many thrilling characteristics, including high charge carrier mobility [77,78], an ambipolar electric field effect [75], good thermal conductivity [79], an abnormal quantum hall effect at room temperature [80,81], chemical inertness and impermeability [82], outstanding strength [83] and stretchability as well as transparency [84]. Due to these properties, graphene is a promising candidate for many applications, e.g., the development of new electronic and optoelectronic devices, exceeding the state-of-the-art regarding size limitations, efficiency and design.[85-91] Furthermore, graphene-based approaches are also discussed in the context of carbocatalysis [92,93], energy storage [94-96], membranes [97,98], coatings [99-101], sensors [102,103] and biomedicine [104-107].

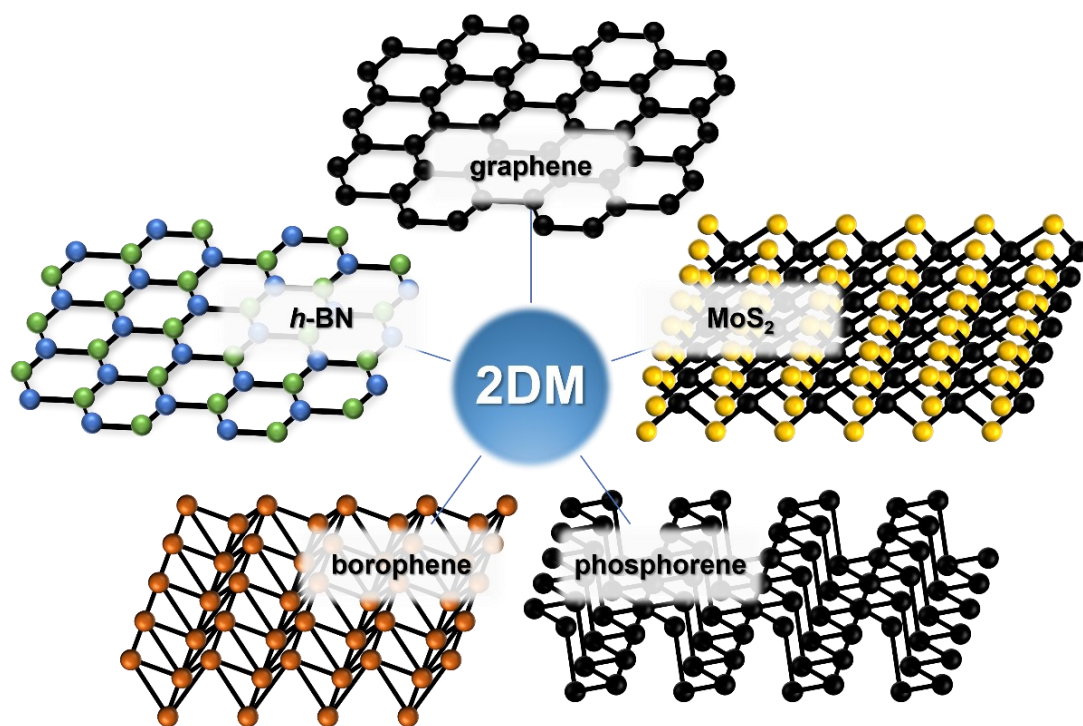


Figure 3. Some prominent mono- and heteronuclear members of the 2D family.

The intriguing chemical, physical and mechanical properties of graphene motivated a huge research interest in the field of 2DMs. Thus, over the last two decades, manyfold 2DMs were theoretically predicted, experimentally realized and thoroughly investigated. Figure 3 provides schematic drawings of some prominent representatives of this class. In general, the 2D family comprises mononuclear, such as graphene, silicene [108], germanene [109], borophene [110] and phosphorene [111], and heteronuclear members, such as *h*-BN [45] and transition metal dichalcogenides [112].

One specifically well-studied 2DM is *h*-BN. Consisting of sp^2 -hybridized alternating boron and nitrogen atoms organized in a hexagonal lattice, it is considered a heteronuclear graphene analog.[113,114] *h*-BN exhibits a row of astonishing properties. Amongst these, some are similar to graphene, such as its structure [113], optical transparency [115] and high mechanical strength [116], others differ substantially from graphene, such as its large band gap of about 6 eV [117], basically rendering it an insulator, and its high thermal stability in air [118,119]. Due to its robustness, *h*-BN is suitable for the development of highly durable, protective coatings.[118,120,121] Moreover, its insulating character in combination with its smooth surface and structural similarity to graphene render it the ideal dielectric substrate for graphene in future electronics.[122-124] In terms of optical properties, BN nanosheets, exhibiting an absorption peak at about 210 – 220 nm in the deep ultraviolet (UV) range [113,117], might be used for the design of new deep-UV light-emitting devices that are able to withstand extreme environmental conditions.[125]

The first intentional preparation of a 2DM, that is, the isolation of graphene by Novoselov and Geim in 2004, was achieved via the so-called scotch tape method, in which a single layer of graphene is obtained by micromechanical cleavage of graphite using adhesive tape.[75,126] This method can generally be applied to layered bulk materials to isolate few- and single-layer materials. Further preparation methods, such as liquid-phase exfoliation and CVD, are described in comprehensive review articles.[113,114,126-129] CVD synthesis of 2DMs is particularly well-suited for their preparation in a surface

science approach under UHV conditions. As precursors, small hydrocarbons, such as propylene or ethylene, and boron- as well as nitrogen-containing compounds, e.g., ammonia borane and borazine, are commonly used for graphene and *h*-BN, respectively.

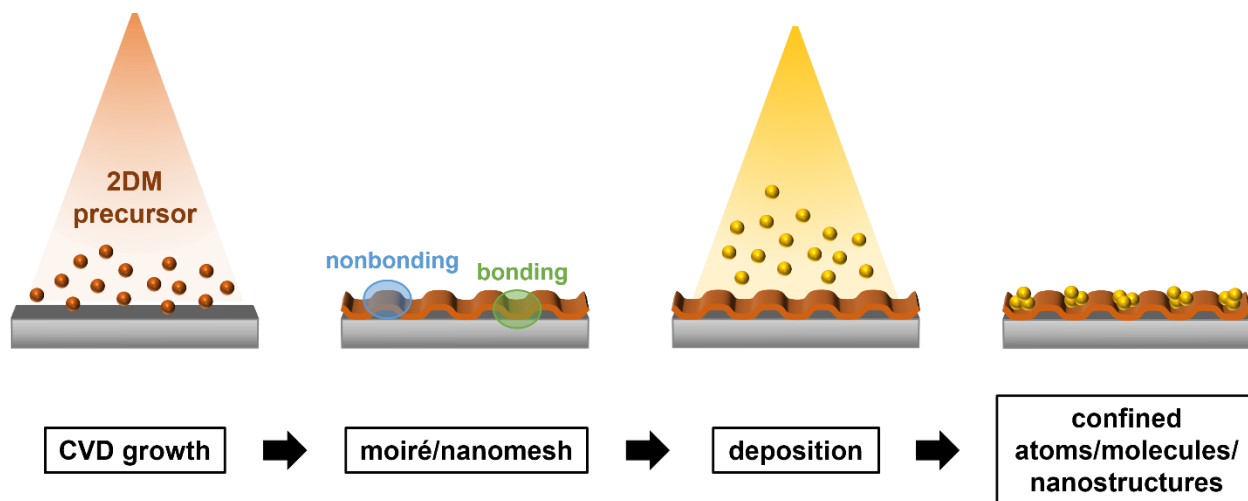


Figure 4. CVD growth of a corrugated 2DM on a single-crystal surface. The resulting moiré/nanomesh can be used as template for directed deposition of atoms and molecules and the confined growth of nanostructures.

Dealing with supported 2DMs, it needs to be considered that the substrate alters the structure and electronic properties of the 2DM, depending on the interaction strength, i.e., the degree of band hybridization.[130-132] If the lattice parameters of the 2DM match the substrate, a flat morphology is obtained.[130,132] In the case of a lattice mismatch, a buckling of the overlayer occurs, which is referred to as moiré or, speaking of *h*-BN on Rh(111), as so-called nanomesh. This corrugation becomes more prominent with increasing interaction strength, as demonstrated by Preobrajenski *et al.* for graphene and *h*-BN on Pt(111), Ir(111), Rh(111) and Ru(0001); while for Pt(111) nearly no buckling is observed, it increases for Ir(111) and Rh(111) and is largest for Ru(0001).[133,134] In a moiré, the regions in close proximity to the substrate undergo strong interaction, leading in general to a pronounced reactivity. The elevated parts of the moiré, on the other hand, hardly interact with the substrate and thus behave almost like freestanding graphene/*h*-BN, i.e., are chemically inert. Due to the different nature of these two regions, corrugated metal-supported graphene and *h*-BN can act as templates for the directed deposition of atoms/molecules and the confined growth of metal clusters.[132,135] The

latter is a promising approach to develop advanced model catalytic systems for the investigation of phenomena in the field of heterogeneous catalysis.[38,136-142] Figure 4 schematically depicts the CVD growth of a corrugated 2DM on a single-crystal surface and illustrates its template effect. A more realistic depiction of the nanomesh/moiré structures of Rh(111)-supported *h*-BN and graphene is provided in Figure 5.

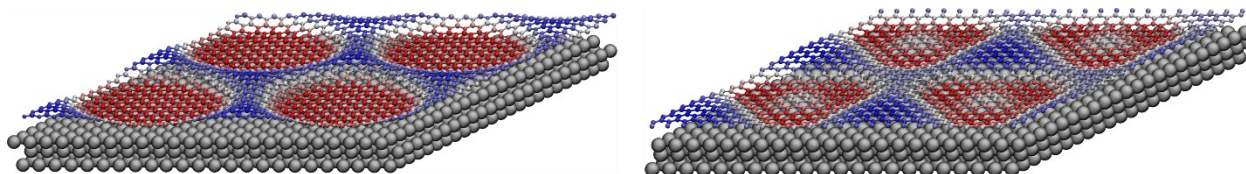


Figure 5. Side view of the *h*-BN/Rh(111) nanomesh (left) and the graphene/Rh(111) moiré (right).

The above-described unique properties of 2DMs might be employed in various fields. To this end, however, the pristine 2DM often needs to be adapted to the respective real-world application, e.g., by controlled chemical modification. In the following, some selected examples of the chemical modification of 2DMs are given; a full overview would by far exceed the scope of this work.

The wet chemical preparation of graphene oxide has already been known since the late 1950s, when the so-called Hummer’s method was established.[143] This method, or an enhanced version of it [144], is nowadays still applied and introduces functional oxo-groups into graphene. Oxo-functionalized graphene might then, for example, serve as a starting point for alkylation via reductive functionalization.[145] Another stable graphene derivative with interesting properties is fluorographene, whose synthesis is comprehensively described in a review article by Feng *et al.*[146] A rather new approach for the chemical functionalization of graphene is direct laser writing. This was demonstrated by Wei *et al.*, who exploited the laser-induced photolysis of silver trifluoroacetate to selectively react graphene with trifluoromethyl groups.[147] Such lithography-based functionalization may be combined with a subsequent post-functionalization step to realize molecular stacking on graphene.[148] Further protocols for the wet- and dry-chemical modification of graphene, *h*-BN and other 2DMs are presented in several thorough review articles.[149-154]

Chemical modification performed under UHV conditions bears the special advantage that the pristine 2DM, its modification and the resulting, chemically modified 2DM can be studied using advanced surface science techniques. Figure 6 illustrates the common strategies (I – III) for chemical modification of supported 2DMs in an UHV approach.

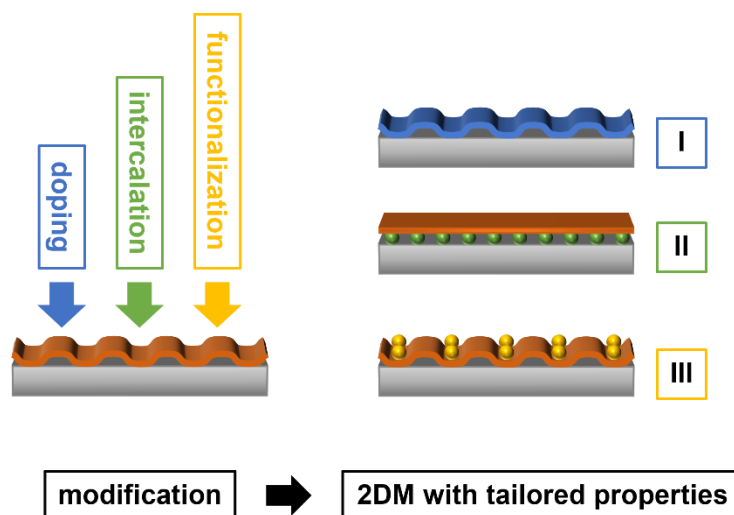


Figure 6. Common strategies for chemical modification of transition metal-supported 2DMs.

In the literature, several studies on the doping (I) of transition metal-supported graphene with heteroatoms are reported, e.g., the doping of Ni(111)-supported graphene with nitrogen and boron.[155-157] Intercalation (II), on the other hand, can be used to tune the coupling strength between 2DM and substrate. The strongly interacting system *h*-BN/Ni(111) can, for example, be decoupled by gold intercalation to obtain “quasi-freestanding” *h*-BN, which may subsequently serve as a substrate for graphene growth.[158] Interestingly, for hydrogen intercalation of the *h*-BN/Rh(111) nanomesh, Brugger *et al.* even observed a flattening of the corrugated overlayer.[159] Another, especially versatile tool for the chemical modification of 2DMs is covalent functionalization (III) with atoms and molecules. In this context, the functionalization of graphene on Ir(111) with atomic hydrogen was found to open its bandgap.[160] Moreover, graphene on Ni(111) was hydrogenated, yielding so-called “graphone”, to test the applicability of graphene in terms of hydrogen storage.[161] Due to the chemical inertness of *h*-BN, it is quite difficult to react this 2DM intentionally with functional groups. Nevertheless, the hydrogen and oxygen functionalization of *h*-BN/Ni(111) was

shown to be possible by Späth *et al.*[162,163] Building up on this work, we conducted selective hydrogen and oxygen functionalization of the *h*-BN/Rh(111) nanomesh, which has been described in my master's thesis and a corresponding publication.[164] In this study, we achieved the spatially defined adsorption of atomic hydrogen and molecular oxygen in the pores of the nanomesh, thereby demonstrating its template effect and proving the crucial influence of the 2DM substrate interaction on covalent functionalization. This template effect was also observed for the bromination of Rh(111)-supported *h*-BN (Chapter 5).[165]

This dissertation deals with the adsorption and reaction of small molecules on Rh(111) and Rh(111)-supported 2DMs, investigated by means of surface science. After Chapter 1, introducing the subject of the work, Chapter 2 will give a brief overview of synchrotron radiation and the surface science techniques applied in our experiments, which were XPS, near-edge X-ray absorption fine structure (NEXAFS) and LEED. In Chapter 3, the reader will be introduced to the experimental setup used for the measurements presented in the scope of this work. Moreover, some information about the data acquisition and processing is given, and another apparatus, which will be used for future experiments, is described. Chapters 4 and 5 provide summaries of the four publications constituting this cumulative dissertation. The full articles and the corresponding supplementary materials can be accessed on the websites of the respective journals; see Appendix A for the corresponding links. Chapters 6 and 7 contain the conclusions and an outlook regarding future projects in English and German language, respectively. Technical drawings are provided in Appendix B.

2 Fundamentals

The research presented in this work was performed under UHV conditions ($\sim 10^{-10}$ mbar) by means of state-of-the-art laboratory- and synchrotron radiation-based surface science. In this context, UHV is indispensable since it guarantees a clean sample environment. Furthermore, it needs to be noted that most surface science techniques require to be performed under UHV conditions. In the following, a brief overview of the fundamental principles of synchrotron radiation and the utilized techniques is given.

2.1 Synchrotron Radiation

The majority of data presented within this dissertation was gathered at the electron storage ring BESSY II of the Helmholtz-Zentrum Berlin (HZB) using synchrotron radiation. Its generation and properties will thus be briefly described.

In 1947, synchrotron radiation was first observed at the General Electric Research Laboratory in Schenectady, USA. Back then, it was an unavoidable energy loss upon deflection, that is, radial acceleration, of charged particles in a ring-shaped accelerator.[166] This deflection of charged particles, e.g., induced via a magnet, is the prerequisite for emission of electromagnetic radiation and the basic principle of a synchrotron facility. The radiation power P_r emitted by a charged particle in a magnetic field can be expressed by:[167]

$$P_r = \frac{cq^2E^4}{6\pi\epsilon_0r^2(mc^2)^4} \quad \text{Equation 1}$$

c = speed of light

q = charge of the particle

E = energy of the particle

ϵ_0 = dielectric constant

r = radius of the curved flight path of the particle

m = mass of the particle

2 Fundamentals

According to Equation 1, due to their low mass and facile generation (usually from a hot cathode), electrons are the most suitable candidates for the efficient production of synchrotron radiation.

In the early days of synchrotron radiation research, accelerators capable of the production of synchrotron radiation would be mainly used for nuclear physics (first generation). Only later, facilities specifically dedicated to the production of synchrotron radiation, so-called second-generation synchrotron sources, were provided, which relied on the usage of bending magnets to force the electrons on a curved flight path. Further improvements came along with the development of insertion devices, such as wigglers and undulators, leading to a significant increase in brilliance with the latter being defined as amount of power (photons per second) per unit frequency, surface area and solid angle. As brilliance is a measure of the amount of light that can be concentrated in a small spot, it is commonly used to rate the performance of synchrotron facilities. Introducing insertion devices into the straight parts of the accelerators, third-generation synchrotron sources were born. The electron storage ring BESSY II is one of these third-generation facilities.[166,167]

The production of synchrotron radiation in a third-generation facility is a multi-step process. First, the electrons are generated via thermionic emission from a hot cathode and pre-accelerated in a linear accelerator (LINAC). Thereupon, the electrons are transferred into a booster ring, in which they are accelerated to the energies required in the storage ring (typically 500 MeV – 20 GeV; BESSY II: 1.7 GeV). After gaining a sufficiently high energy, the electrons are injected into the storage ring. The most important parts of the storage ring are bending magnets to force the electrons onto a closed orbit, quadrupoles to focus the electron beam, insertion devices to generate highly brilliant synchrotron radiation and radio frequency (RF) cavities to make up for energy losses of the electrons. Due to continuous losses, the ring current exhibits a limited lifetime. In modern facilities, this can be avoided by electrons being periodically injected to maintain a constant ring current (top-up mode).[166,167] Figure 7 visualizes the setup of a third-generation synchrotron facility.

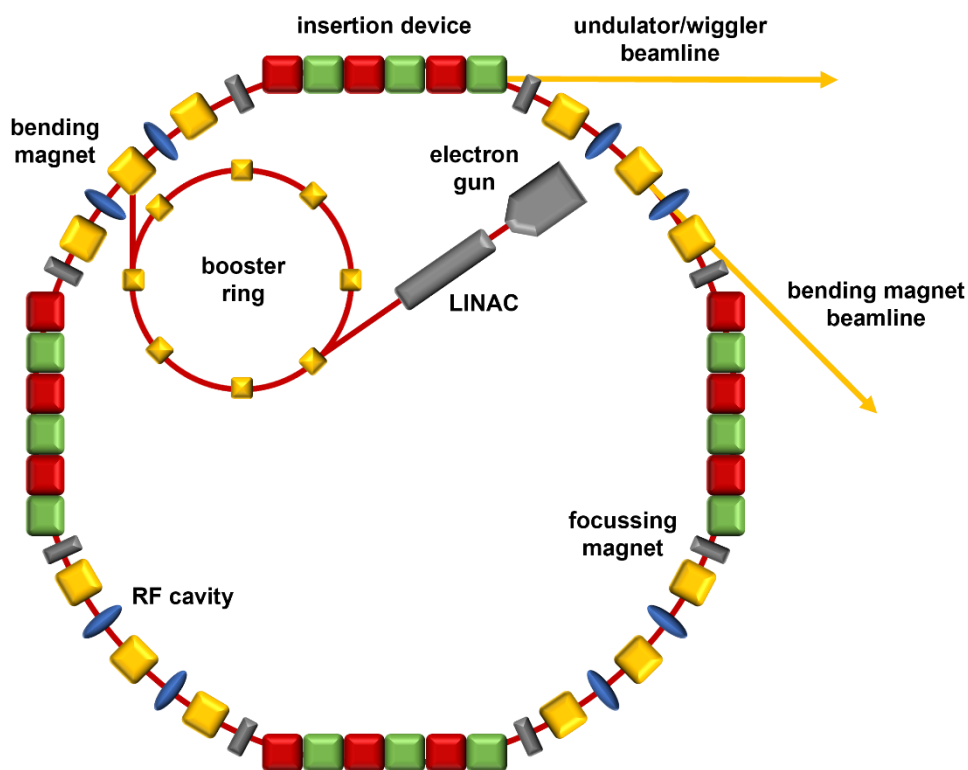


Figure 7. Schematic setup of a third-generation synchrotron facility, including an electron source, devices for pre-acceleration and the electron storage ring.

In comparison to conventional laboratory-based radiation sources, such as X-ray tubes and UV lamps, bending magnets provide radiation with a significantly enhanced brilliance. As already mentioned above, insertion devices enable production of even more intensive/brilliant radiation. Schemes of such insertion devices, i.e., of a wiggler and an undulator, are depicted in Figure 8.

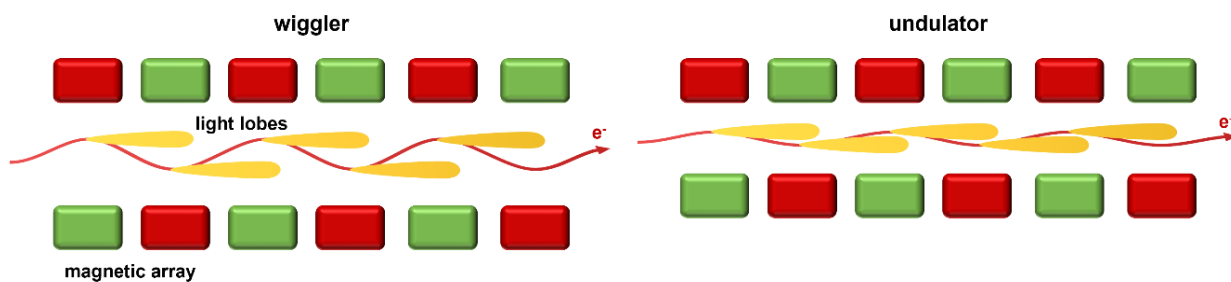


Figure 8. Insertion devices for the generation of synchrotron radiation: wiggler (left) and undulator (right).

Wigglers and undulators work according to the same principle: An upper and a lower magnetic array with alternating poles force the electrons in between on an oscillatory flight path, leading to emission of light in each curve and thereby to an increase in

brilliance in comparison to bending magnets. Bending magnets and wigglers both deliver a continuous spectrum. In the case of undulators, however, the upper and lower magnetic array are placed closer together. Consequently, the amplitude of the oscillation of the electron beam is smaller, and the light lobes produced in each curve can overlap and interfere, with only certain wavelengths undergoing constructive interference. The undulator spectrum thus shows a fundamental frequency and its higher (odd) harmonics.[166,167] The spectral characteristics of the radiation produced by bending magnets, wigglers and undulators are shown in Figure 9.

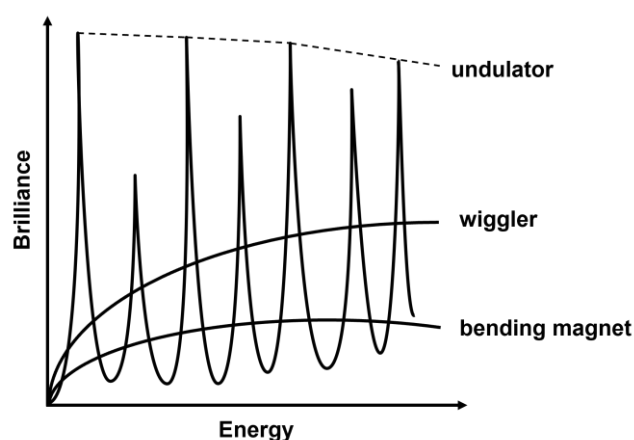


Figure 9. Bending magnet, wiggler and undulator: Spectral characteristics.

The usage of synchrotron radiation offers several advantages over laboratory-based methods: a large spectral range from IR to hard X-rays (10 eV – 100 keV), outstanding brilliance (see above), a high photon flux, coherence, a well-defined time structure and variable polarization.[167,168] The adjustable photon energy is key to special techniques, such as NEXAFS, which require scanning of the photon energy. In addition, this allows for selection of an appropriate photon energy in XPS to achieve the optimum cross sections for the core levels of interest, resulting in a significantly enhanced signal intensity. The brilliance of synchrotron radiation, on the other hand, leads to a superior spectral resolution in XPS, making a detailed interpretation of the data on the molecular level feasible. Also, the high photon flux is of utmost importance to realize fast data acquisition, which is crucial to perform *in situ* experiments.

2.2 X-Ray Photoelectron Spectroscopy

A photon impinging on a solid sample leads to emission of a photoelectron given that the photon energy exceeds the work function of the respective sample (Figure 10).[3]

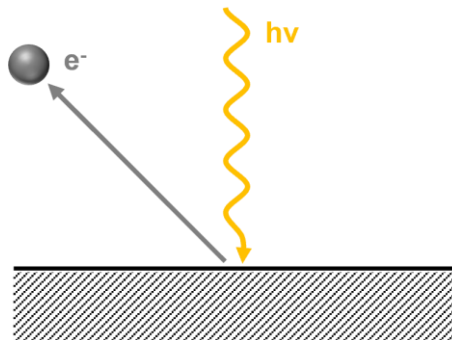


Figure 10. Schematic visualization of the photoelectric effect.

This so-called photoelectric effect, also referred to as photoeffect, forms the basis of XPS. The genesis of XPS thus reaches back to the late 19th century when Hertz was the first to experimentally observe the photoelectric effect.[169] Almost 20 years later, in 1905, Einstein was able to explain Hertz's observation in his revolutionary publication "Über einen die Erzeugung und Verwandlung des Lichtes betreffenden Heuristischen Gesichtspunkt".[170] For his groundbreaking contribution to the understanding of the photoelectric effect, Einstein was awarded the 1921 Nobel prize in Physics. Later, in the 1950s, Siegbahn *et al.* paved the way for the method of XPS as it is performed today. For his pioneering work in the field of electron spectroscopy, Siegbahn was awarded the Nobel prize in Physics in 1981.[171,172]

In XPS, X-ray photons, produced by standard laboratory-based X-ray tubes or synchrotron light sources (see above), are used to eject core electrons from a sample. The so-called three-step model can be used to describe the emission of a photoelectron upon absorption of a photon with energy $h\nu$ in a simplified manner: First, a (core) electron is excited (photoionization). Second, the photoelectron is transported to the surface. Third, transmission of the photoelectron through the surface into the vacuum takes place.[4,173] This process and a schematic XP spectrum are visualized in Figure 11.

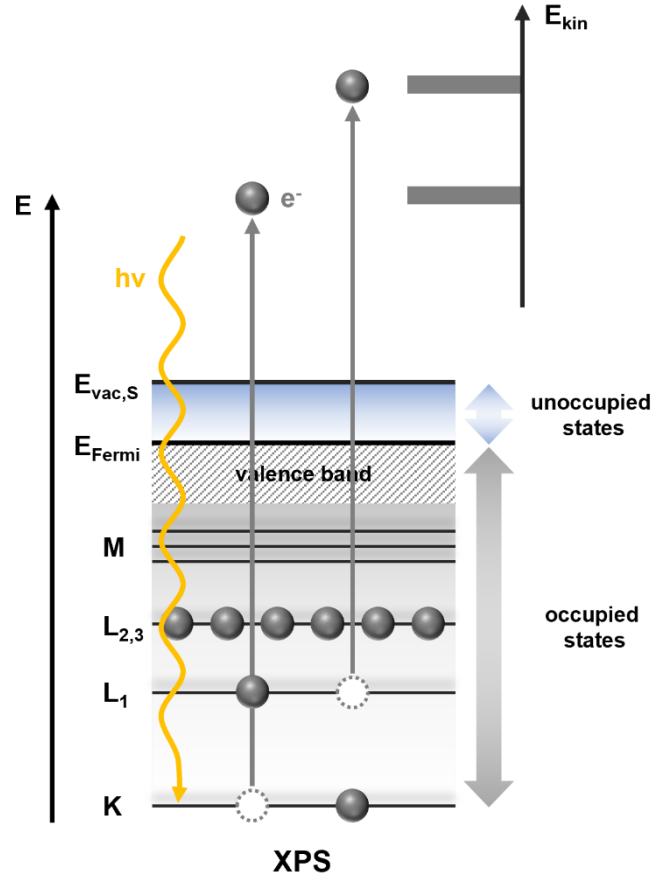


Figure 11. XPS process: Absorption of a photon leads to emission of a core electron into to the vacuum. Additionally, a schematic XPS spectrum is shown.

To escape into the vacuum, the work function ϕ_S of the sample, corresponding to the difference between the vacuum level of the sample $E_{vac,S}$ and the Fermi level E_{Fermi} , needs to be overcome. Accordingly, the kinetic energy $E_{kin,S}$ of the resulting photoelectron, which is eventually analyzed, can be expressed by:[173,174]

$$E_{kin,S} = h\nu - E_B - \phi_S \quad \text{Equation 2}$$

The emitted photoelectron carries valuable information about the sample of interest as the binding energy E_B of the core electron is element-specific and sensitive to the chemical environment of the probed atom. Thus, one aims for the determination of E_B . According to Equation 2, $E_{kin,S}$, $h\nu$ and ϕ_S need to be known to calculate E_B . In the experimental setup (Figure 12), the sample and the electron analyzer are conductively connected. Thus, both have the same E_{Fermi} , which is usually taken as the reference level (set to 0 eV). The work functions of the sample and the analyzer, however, differ from each other, with the

work function of the analyzer ϕ_A being in general known.[174] The kinetic energy of the photoelectrons as measured by the analyzer $E_{kin,A}$ can then be described by:

$$E_{kin,A} = E_{kin,S} + \phi_S - \phi_A \quad \text{Equation 3}$$

Taking Equations 2 and 3 into consideration, E_B can be determined according to:[174]

$$E_B = h\nu - E_{kin,A} - \phi_A \quad \text{Equation 4}$$

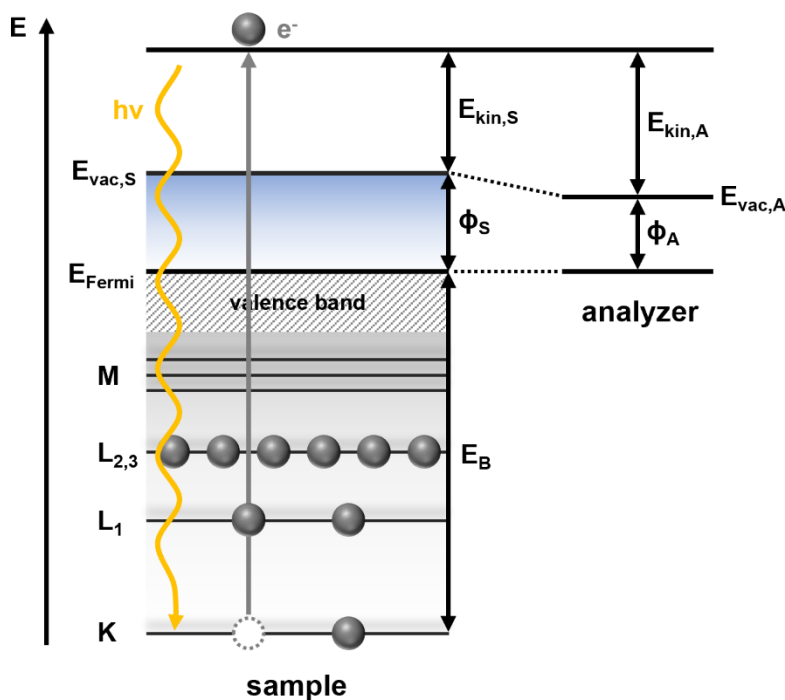


Figure 12. Scheme visualizing how the binding energy of the photoelectrons relates to the work function of the analyzer and the kinetic energy as measured by the analyzer.

The inelastic mean free path λ_{IMFP} of electrons is very limited within matter. Consequently, only electrons from the outermost layers of a sample can escape into the vacuum and be detected. This causes XPS to be a highly surface-sensitive method, rendering it a very valuable tool in surface science. The universal curve, established by Seah and Dench, visualizes how the inelastic mean free path of photoelectrons depends on their kinetic energy, leading to the conclusion that the highest surface sensitivity can be achieved for kinetic energies between 70 and 100 eV.[175] Therefore, given that an adjustable photon energy is available (synchrotron radiation), the incident photon energy is chosen such that the outgoing photoelectron exhibits a kinetic energy within this

optimum range. To enhance the surface sensitivity in a standard laboratory approach, XPS can be applied in an angle-resolved manner. The sampling depth d of a photoelectron is given by:[174]

$$d = 3\lambda_{IMFP} \cos \theta \quad \text{Equation 5}$$

Accordingly, decreasing the electron take-off angle θ (angle of electron exit relative to the sample surface) decreases d and thus increases the surface sensitivity.[171,174]

Due to the binding energy of the photoelectrons being element-specific, the chemical composition of a surface species can be determined by XPS. Moreover, deviations regarding the chemical environment of the atoms lead to distinct shifts of the corresponding binding energies. These so-called chemical shifts result from the superposition of initial and final state effects. Initial state effects are due to intra- (from within the atom) and inter-atomic (from neighboring atoms) ground state polarization and spin-orbit-splitting. Typical examples are the oxidation state of the emitting atom, electronegativity of neighboring atoms and bond distances within the molecule. The spin orbit splitting arises for photoelectrons from orbitals with nonzero angular momentum quantum number and is observed, given that the spectral resolution is high enough, as a doublet with a distinct ratio, e.g., 1:2 for a photoelectron from a p orbital. Final state effects appear as a consequence of the creation of a core hole upon photoemission, which induces perturbation of the electronic structure, leading to polarization (electrostatic and magnetic effects) and intra-/inter-atomic electronic rearrangement (excitation and relaxation processes). Core hole-induced polarization can, for example, be observed as multiplet splitting. Rearrangement, on the other hand, gives rise to modified/additional signals in the XP spectrum, such as peak asymmetry or satellite peaks, plasmon loss features and Auger electron peaks (see below). Shake-up and shake-off satellites occur if the photoelectron loses kinetic energy on its way out of the sample by exciting another electron to a bound state close to the Fermi edge (shake-up) or even to an unbound continuum state (shake-off). These features appear, due to the loss of kinetic energy, at higher binding energies than the main photoelectron peak. The relaxation of the core hole

might also be affected by screening effects, e.g., via charge transfer from the substrate, causing lower binding energies as the “stabilization” of the core hole facilitates the ejection of the photoelectron, i.e., the photoelectron exhibits a higher kinetic energy. Overall, it needs to be noted that initial and final states are often difficult to separate. Hence, XPS signals are usually discussed taking the total chemical shift into consideration.[174,176]

Another final state effect that can be observed in high-resolution XP spectra of small hydrocarbons is the excitation of vibrations in the ionic final state according to the Franck-Condon principle, leading to a distinct satellite structure. The latter is referred to as vibrational fine structure, which can be analyzed in a simplified manner using the linear coupling model, introduced by Cederbaum and Domcke.[177] According to this model the intensity distributions follows a Poisson function:[176,178-180]

$$I(0 \rightarrow \nu) = e^{-S} \frac{S^\nu}{\nu!} \quad \text{Equation 6}$$

ν = vibrational quantum number in the ionic final state

S = S factor (average quantum number for vibrational excitation)

For $\nu = 1$, the S factor can be determined as the intensity ratio between the first vibrationally excited ($I(0 \rightarrow 1)$) and the adiabatic peak ($I(0 \rightarrow 0)$):[176,179]

$$S = \frac{I(0 \rightarrow 1)}{I(0 \rightarrow 0)} \quad \text{Equation 7}$$

Within the linear coupling model, assuming that the vibrational frequencies ω in the ground and excited state are the same, the S factor is given by:[176,178-180]

$$S = \frac{\mu\omega m(\Delta r)^2}{2\hbar} \quad \text{Equation 8}$$

μ = reduced mass

Δr = change of the minimum in the potential energy curve upon excitation

m = number of equivalent C-H bonds

2 Fundamentals

Equation 8 shows that the intensity of the first vibrationally excited state linearly depends on the number of C-H bonds, which enables fingerprinting via analysis of the vibrational signature.

XPS also provides quantitative information since the signal intensity I (peak height/area) is directly proportional to the concentration c of the emitting atom in the sample:[174]

$$I = Jc\sigma K\lambda_{IMFP} \quad \text{Equation 9}$$

J = X-ray flux

σ = photoelectron cross section

K = instrumental factor

Quantification errors may arise from inadequate background treatment, final state effects, such as shake-up and shake-off processes, and PED. The latter is likely to occur when working with low-energy electrons (~ 100 eV), having a wavelength on the order of atomic distances, and causes deviations of the observed signal intensity. As PED is sensitive to the chosen electron take-off angle and the photon energy, these parameters may be varied to clarify whether PED is to be considered.[4,174] An easy approach for the determination of surface coverages is the comparison of the peak area of a species of interest to the peak area of a reference compound with the surface coverage of the latter being known.

Prior to ejection from the sample, some photoelectrons undergo interaction with matter, i.e., are inelastically scattered. In the XP spectrum, this leads to a broad background at the high binding energy side. Hence, in terms of data processing, a background correction is usually performed. To this end, most commonly a linear, Shirley [181] or Tougaard [182] background is subtracted from the spectrum.[174] In addition, for a thorough analysis of the XPS signals, deconvolution of the spectrum, that is, peak fitting, is required. The line width in XPS is determined by instrumental factors, such as the energy resolution of the electron analyzer and the full width at half maximum of the photon source, and the lifetime of the core hole, i.e., the uncertainty principle. The former

causes a Gaussian line shape while the latter broadens the peak and results in a Lorentzian line shape. Overall, the observed XPS peak shape is thus a convolution of a Gaussian and a Lorentzian function.[183] However, if an asymmetry of the peaks arises, this is not sufficient for a qualitatively good fit. In this case, peak fitting can be performed using Doniach-Sunjić profiles [184] convoluted with a Gaussian function.

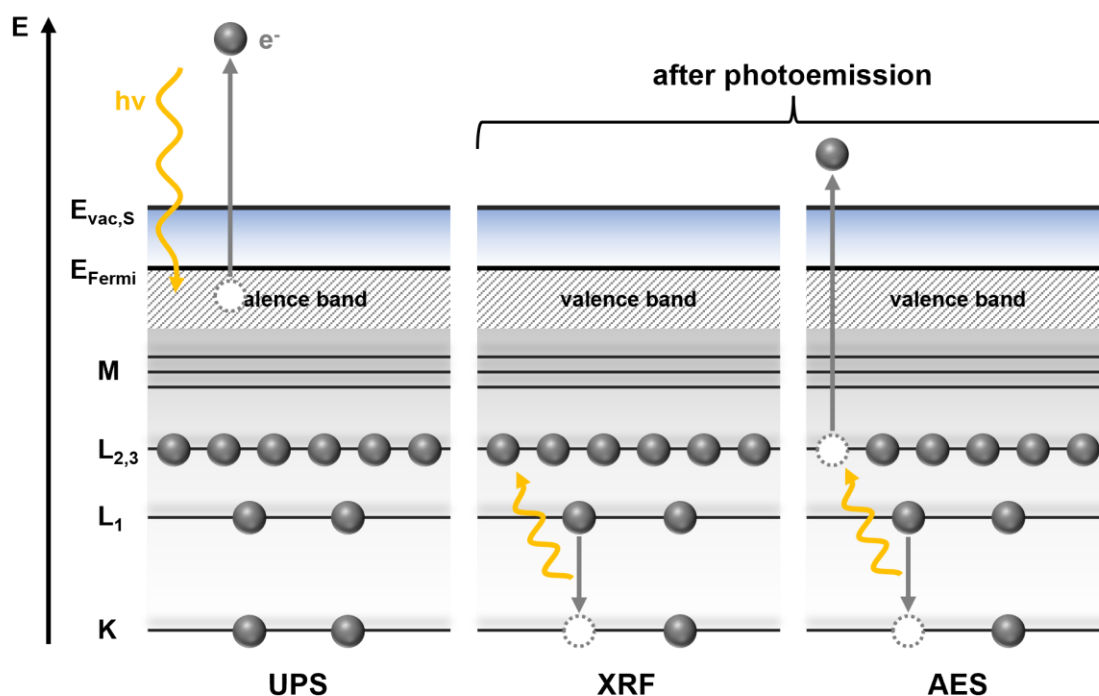


Figure 13. XPS-related techniques: UPS uses UV light to evoke photoemission from the valence band. XRF is detected upon radiative relaxation of the core hole created by photoemission. AES is based on Auger electrons that are emitted upon non-radiative relaxation of the core hole created by photoemission.

Besides XPS, photoemission lays the foundation for several related techniques (Figure 13). If, instead of X-ray photons, UV light, typically produced by a gas discharge lamp, is used to evoke photoemission, electrons from the valence band (0 – 20 eV) will be emitted with high cross section. This method is called UPS and allows for gathering information about the filled bonding orbitals of adsorbed molecules.[185] In addition, the core hole created upon photoemission gives rise to two further techniques as it can be filled by two competing processes: radiatively by X-ray fluorescence (XRF), or non-radiatively by emission of an Auger electron. In XRF, an electron from a higher-lying core level fills the core hole, and the excess energy is emitted as a characteristic X-ray photon

of energy ($E_K - E_{L_1}$). In Auger electron spectroscopy (AES), on the other hand, the excess energy is given to another electron, which is thereupon ejected with energy ($E_K - E_{L_1} - E_{L_{2,3}}$). These Auger electrons lead to additional signals in XP spectra. Auger and XPS signals can, however, be easily distinguished from each other since an Auger peak appears always at the same energy while the XPS peak shifts upon variation of the incident photon energy. For elements with low atomic numbers Z , the relaxation of 1s core holes via the Auger process is much more likely than XRF, while the situation is reversed for high Z values. Both methods, XRF and AES, are useful for the determination of elemental compositions.[4,171]

2.3 Near-Edge X-Ray Absorption Fine Structure

X-ray absorption spectroscopy (XAS) is based on the absorption of X-ray photons. If the energy of the photon equals the energy difference between two states involved in an according to symmetry selection rules allowed electronic transition, a corresponding resonance can be observed. To excite such resonant transitions, an adjustable photon energy is a prerequisite. Thus, the development of XAS-related techniques is closely intertwined with the rise of synchrotron radiation-based research.[166]

In XAS, a specific absorption edge is investigated, e.g., the K-edge. To this end, the photon energy is scanned in the regime of the ionization potential (IP) of the 1s electron of the element of interest. The IP represents the threshold for transitions of the 1s electron into the continuum. Notably, modulations of the absorption edge might occur, which are referred to as X-ray absorption fine structure. This fine structure is distinguished into the near-edge fine structure up to about 50 eV above the edge, arising due to electronic transitions into unoccupied states, and the extended fine structure beyond 50 eV above the edge, which results from interference effects due to backscattering of neighboring atoms. If the near-edge region is examined, one speaks of NEXAFS (or also of XANES – X-ray absorption near-edge spectroscopy). The analysis of the extended fine structure, on the other hand, is subject to extended X-ray absorption fine structure (EXAFS). NEXAFS can be used to learn about the oxidation state of the absorber, the molecular orientation

and the sample composition while EXAFS provides information on interatomic distances and coordination numbers. As EXAFS was not employed in the scope of this work, it will not be described in further detail.[4,166,186,187]

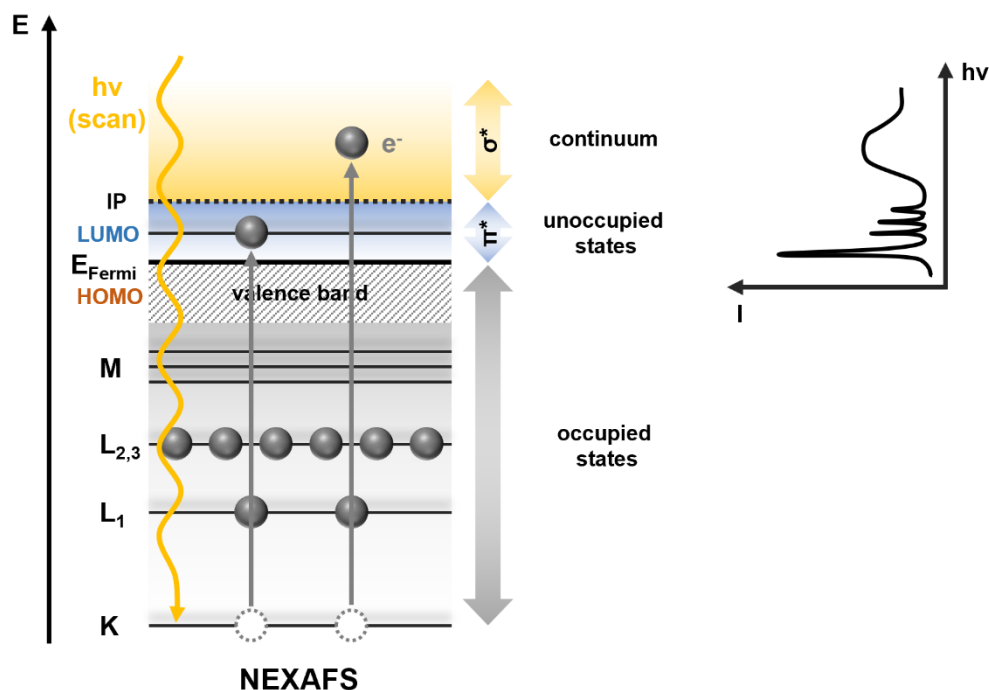


Figure 14. NEXAFS process: Absorption of a photon leads to excitation of core electrons into unoccupied bound and quasi-bound states. Additionally, an exemplary, simplified NEXAFS spectrum, including π^* , Rydberg and σ^* resonances, is shown.

NEXAFS probes bound ($< IP$) and “quasi-bound” ($> IP$) unoccupied states. “Quasi-bound” refers to states that lie above the IP but are still trapped within the molecular potential. In molecules featuring a double/triple bond, the lowest unoccupied molecular orbital (LUMO) corresponds to a π^* state. Upon investigation of such molecules by NEXAFS, $1s \rightarrow \pi^*$ transitions are commonly observed as the lowest-energy structures, located below the IP. The π^* resonances are in general quite sharp and often the most prominent features. Above the $1s$ to IP energy, usually rather broad σ^* (shape) resonances arise. The shape of the observed resonances depends on the finite lifetime of the excited quasi-bound state, the vibrational motion of the atoms in the molecule, leading to peak broadening, and the resolution of the instrument. Probing unoccupied states located above the IP, the lifetime broadening increases as it becomes more and more probable

that the excited electron decays into the continuum.[4,187,188] In Figure 14, the NEXAFS process is schematically depicted, and an exemplary NEXAFS spectrum is shown.

From NEXAFS, manifold information can be gained. For example, given that the spectra of suitable reference compounds are available, one can identify the respective surface species by its characteristic spectral fingerprint. Moreover, the oxidation state of the species of interest may be determined as the position of the absorption edge is sensitive to the charge of the respective absorber. Even a correlation between the bond length and the position of the σ^* resonance has been discussed.[188] For our research, the most interesting aspect is that NEXAFS allows for the elucidation of the molecular orientation of an adsorbed surface species, a method which was first introduced by Stöhr and Jaeger in 1982.[189] This is due to the transition probability depending on the polarization of the incident light. According to Fermi's Golden Rule, the absorption cross section σ_x relates as follows to the initial state Ψ_i and the final state Ψ_f : [188]

$$\sigma_x \propto |\langle \Psi_f | \mathbf{e} \mathbf{p} | \Psi_i \rangle|^2 \rho_f(E) \quad \text{Equation 10}$$

\mathbf{e} = unit electric field vector

\mathbf{p} = dipole transition operator

$\rho_f(E)$ = density of final states

The orientation of bonds and their corresponding molecular orbitals relative to the orientation of the electric field vector thus determines the transition probability (dipole selection rule). When linearly polarized synchrotron radiation excites a 1s electron into a final state with a defined direction, the resonance intensity I depends on the angle δ between the electric field vector and the direction of the final state orbital \mathbf{O} : [188]

$$I \propto |\mathbf{e} \langle \Psi_f | \mathbf{p} | \Psi_i \rangle|^2 \propto |\mathbf{e} \mathbf{O}|^2 \propto \cos^2 \delta \quad \text{Equation 11}$$

Hence, the maximum resonance intensity is attained for the electric field vector pointing in the direction of the respective final state orbital while the intensity vanishes for the electric field vector being perpendicular to the orbital. To learn about the molecular orientation of an adsorbate, the intensity of the NEXAFS features is recorded as a function

of the angle of the incident light. For a molecule including a double bond, the direction of the σ orbitals coincides with the bond axis whereas the π orbitals are perpendicular to the bond axis. Let us assume that a molecule is adsorbed with the double bond parallel to the surface, as depicted in Figure 15. Taking a NEXAFS spectrum at normal incidence (NI, 0° with respect to the surface normal), the electric field vector, which is perpendicular to the propagation direction of the light, matches the direction of the σ orbitals. Thus, a maximum intensity of the σ^* resonances can be observed in the corresponding spectrum, and the π^* resonances disappear. In the case of grazing incidence (GI, large angle with respect to the surface normal), on the other hand, the electric field vector is almost parallel to the π bond of the molecule, leading to significant enhancement of the π^* resonances and decrease of the σ^* resonances.[4,187,188,190]

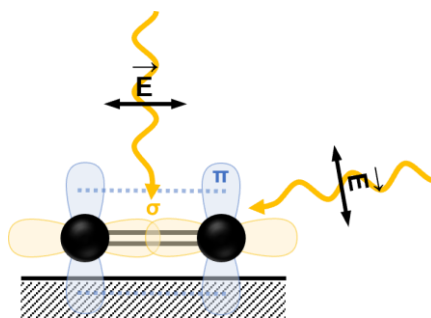


Figure 15. Dipole selection rule: A molecule is adsorbed with its double bond parallel to the surface. At NI, the electric field vector aligns with the σ orbitals, leading to enhancement of the σ^* resonances in the NEXAFS spectrum. At GI, the electric field vector aligns with the π orbitals, leading to enhancement of the π^* resonances in the NEXAFS spectrum. Please note that the σ^*/π^* orbitals exhibit the same symmetry as the corresponding σ/π orbitals.

Due to the photoabsorption process, a core hole and an excited electron are produced. Subsequently, the core hole is filled either radiatively via emission of fluorescence or non-radiatively via emission of an Auger electron (Figure 13). Accordingly, in terms of measuring the X-ray absorption signal, one distinguishes between electron and fluorescence yield detection. In our experiments, we used electron yield detection, which can be divided into three different techniques: Auger electron yield (AEY), partial electron yield (PEY) and total electron yield (TEY). In AEY, only Auger electrons are detected by use of an electron energy analyzer. This method ensures a high surface sensitivity. However, only few electrons are detected, leading to a poor count rate. To

increase the latter, PEY might be used instead. PEY detection collects all electrons with a kinetic energy larger than a distinct threshold energy. To this end, a retarding grid detector is used. All our NEXAFS measurements were performed in PEY mode. The highest count rate at the cost of the lowest surface sensitivity is obtained for TEY, in which all emitted electrons, also slow electrons from the bulk, are detected.[187,190]

2.4 Low-Energy Electron Diffraction

Diffraction methods are versatile tools for the investigation of the lateral long-range periodicity of surfaces and adsorbates. To enable diffraction, the wavelength of the respective irradiated wave/particle needs to be in the same order of magnitude as the interatomic distances of the sample, which measure typically only a few Ångström (Å; $1 \text{ Å} = 10^{-10} \text{ m}$). According to de Broglie, the wavelength λ of electrons is calculated according to the following formula:[191]

$$\lambda = \frac{h}{p} = \frac{h}{mv} = \frac{h}{\sqrt{2mE_{kin}}} \quad \text{Equation 12}$$

h = Planck's constant

m = mass of the electron

v = velocity of the electron

E_{kin} = kinetic energy of the electron

From Equation 12 it can be deduced that electrons with an energy of about 150 eV have a wavelength of 1 Å. Therefore, low-energy electrons seem to fulfill the requirement for diffraction from solid matter. The successful diffraction of such electrons and therewith their wave character was first observed by Davisson and Germer in 1927.[192] However, it took almost another 50 years until LEED was finally used for the structure determination of surfaces. Since then, LEED has become a standard technique in surface science. The latter can be explained by its high surface sensitivity, which is caused by the small inelastic mean free path of electrons in matter.[193]

Every real-space lattice has a counterpart in reciprocal space. These relate to each other as follows:[191]

$$\vec{a}_i^* \times \vec{a}_j = \delta_{ij} \quad \text{Equation 13}$$

\vec{a}_i^* = unit vector of the reciprocal lattice

\vec{a}_j = unit vector of the real-space lattice

δ_{ij} = Kronecker delta

Accordingly, the reciprocal unit vectors are orthogonal and regarding their length reciprocal to the corresponding real-space vectors, i.e., large distances in real space are small in reciprocal space (Figure 16). Diffraction is easily described in reciprocal space since a diffraction pattern can be understood as the projection of the reciprocal lattice.

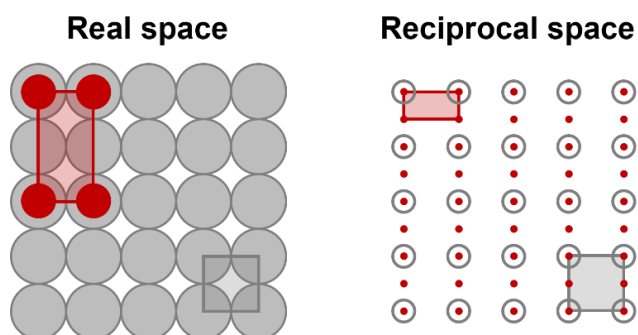


Figure 16. Unit cells of a surface/adsorbate in real and reciprocal space.

To be able to observe a diffraction pattern, two prerequisites need to be given: First, the sample of interest must exhibit a long-range periodic order. Second, the incoming and outgoing waves need to undergo constructive interference. In the reciprocal space, the latter is fulfilled if the Laue condition applies:[193,194]

$$\Delta\vec{k} = \vec{k}' - \vec{k} = \vec{g} \quad \text{Equation 14}$$

\vec{k} = incident wave vector

\vec{k}' = diffracted wave vector

\vec{g} = reciprocal lattice vector

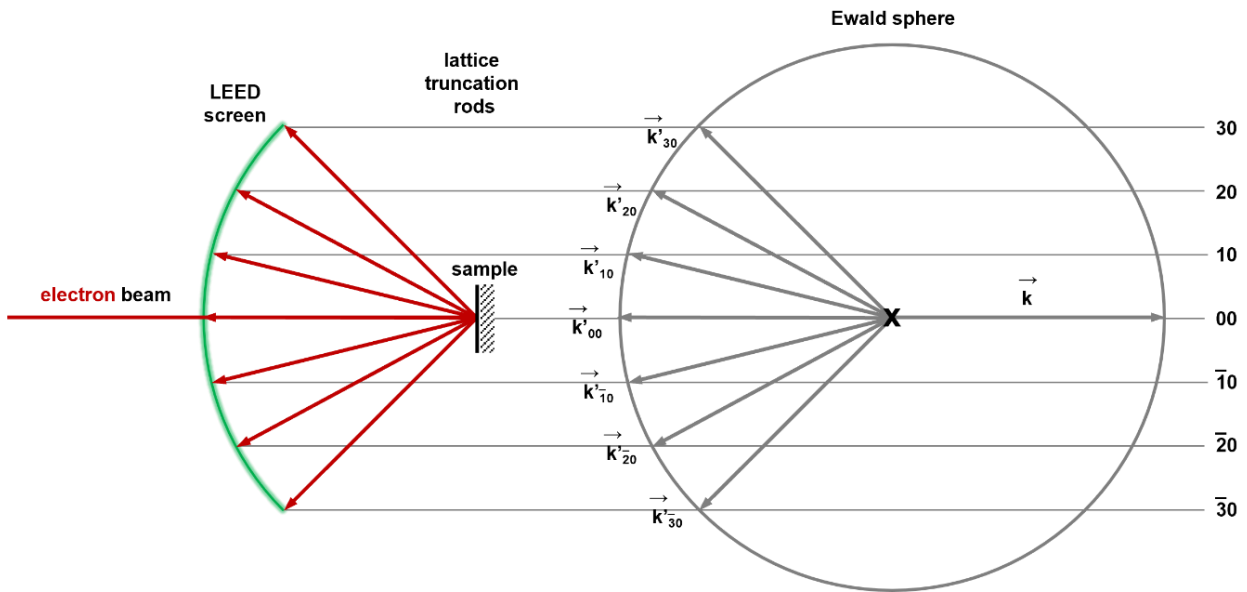


Figure 17. Construction of the Ewald sphere for the 2D case.

The diffraction directions of a given \vec{k} can be determined by construction of the Ewald sphere. To this end, a sphere with the radius $r = |\vec{k}| = \frac{2\pi}{\lambda}$ is drawn around the origin of \vec{k} , pointing towards the origin of the reciprocal lattice. Only lattice points on this sphere fulfill the Laue condition and will be observed as diffraction spots. For the 2D case, no translational symmetry exists perpendicular to the surface, leading instead of lattice points to so-called lattice truncation rods in the reciprocal space. If these are intersected by the Ewald sphere, corresponding diffraction spots are visible. This is visualized in Figure 17. Decreasing the wavelength of the incident electron results in an increasing size of the Ewald sphere, i.e., more diffraction spots can be observed (first and higher order diffraction).

Typical LEED optics consist of an electron gun, two to four grids and a fluorescent screen. Figure 18 shows the setup of a conventional four-grid LEED optic. The electron gun comprises a cathode to generate electrons, an electrostatic lens built up from a Wehnelt cylinder and an anode to extract a focused electron beam, an electrostatic einzel lens ($L_1 - L_3$) to further focus the beam and a grounded lens (L_4) to guide the electrons towards the sample within a field-free space. Upon impinging on the grounded sample, the electrons are diffracted and travel towards the grids. The first grid is also grounded to

maintain a field-free space, thereby avoiding undesired deflection of the electrons. To filter out inelastically scattered and secondary electrons, a negative retarding voltage is applied to the next two grids. The grid in front of the fluorescent screen is grounded, and a high voltage (5 – 6 kV) is applied to the screen to accelerate the elastically scattered electrons. Upon impact on the screen diffraction spots become visible due to luminescence. From the obtained LEED pattern, the long-range order of the surface/adsorbate can be determined.[191,193,194]

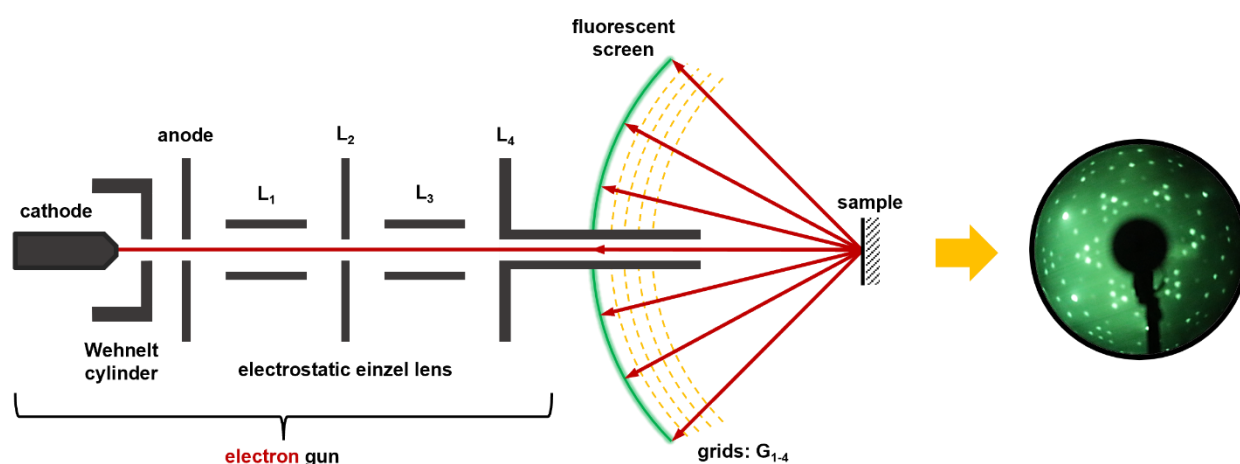


Figure 18. Schematic representation of the setup of a conventional four-grid LEED optic, including an electron gun, four grids and a fluorescent screen. In addition, an exemplary LEED pattern is shown.

Standard LEED can only give insights into the long-range periodicity of a surface/adsorbate while the arrangement of atoms within the unit cell cannot be accessed. To obtain information regarding interlayer distances, adsorption sites and bond lengths, LEED can be performed such that the diffraction spot intensity is measured as a function of the electron energy.[186,195-197] This method is referred to as LEED-IV structure analysis, which was, however, not applied in the present work and is thus not described in detail.

3 Experimental

3.1 Experimental Setup

The experimental data discussed in [P1] – [P4] were obtained using a transportable, two-chamber UHV apparatus called “Sync chamber” (Figure 19), which is described in greater detail in the dissertation of M. Kinne.[198] All experiments were carried out under UHV conditions (base pressure of $\sim 1 \times 10^{-10}$ mbar), provided by an array of pumps, including diaphragm pumps to generate the pre-vacuum as well as turbomolecular, titanium sublimation and ion getter pumps to achieve UHV. The “Sync chamber” comprises a preparation and an analyzer chamber, interconnected by a gate valve, a dosing system, a supersonic molecular beam and a manipulator.

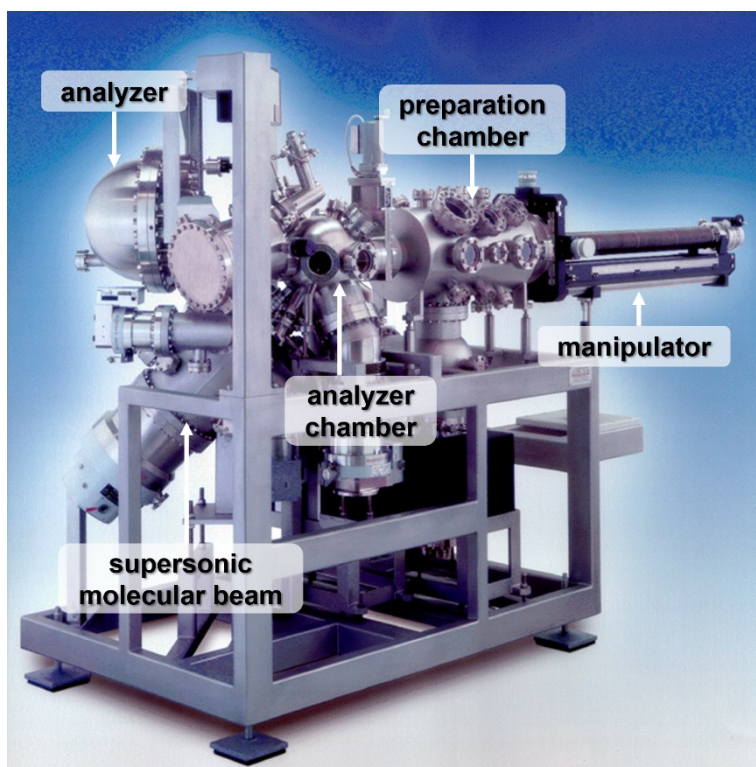


Figure 19. Photography of the “Sync chamber”, adapted from the dissertation of M. Kinne.[198]

The preparation chamber is equipped with an ion gun (Specs IQE 11/35) for Ar^+ sputtering, used for sample cleaning, LEED optics (Specs ErLEED), several electron beam evaporators (Focus) for metal deposition and a quartz crystal microbalance (QCM, Inficon SQM-160) for the determination of deposition rates. For analysis, a hemispherical

electron energy analyzer (Omicron EA 125 U7 HR), a home-built PEY NEXAFS detector and a quadrupole mass spectrometer (QMS, Pfeiffer Vacuum Prisma QME 200) are attached to the analyzer chamber. The NEXAFS detector is described in detail in the dissertation of C. Gleichweit.[199] Being operated at a synchrotron facility, the analyzer chamber can be connected to an open-port beamline. For XPS measurements in our laboratory in Erlangen, we used a standard X-ray tube (Omicron DAR 400) with a dual anode to generate either Al K_{α} ($h\nu = 1486.6$ eV) or Mg K_{α} ($h\nu = 1253.6$ eV) radiation. An individually pumped dosing system for liquids and solids is attached to both chambers. Furthermore, a three-stage supersonic molecular beam allows for introduction of gases into the analyzer chamber in such a way that the atoms/molecules are focused onto the sample surface, which results in a high local pressure on the sample while keeping an overall low background pressure. Up to two gases may be mixed, e.g., for seeding, with the respective gas flow being adjusted by mass flow controllers (MKS Instruments). Via seeding with light, inert gases (usually helium) and additional heating, the kinetic energy of the gas particles can be increased.

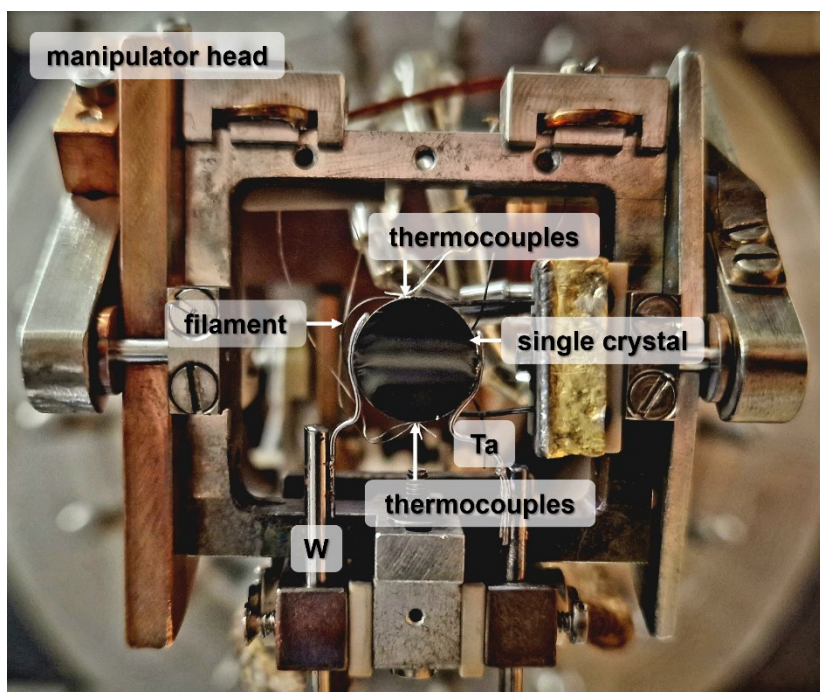


Figure 20. Photography of the manipulator head of the “Sync chamber”, showing the sample, the thermocouples attached to it and the filament mounted in the back.

3 Experimental

The manipulator enables precise movement of the sample along the x-, y- and z-axes as well as its rotation about the azimuthal and polar angle. Liquid nitrogen cooling allows for a minimum sample temperature of about 100 K. Heating, on the other hand, can either be done resistively up to 1400 K or using a tungsten filament, mounted behind the sample, up to 550 K. The latter prevents the change of the photoelectron trajectories due to disturbing electrical fields, which would arise in the case of resistive heating. It is used for TPXPS, in which XP spectra are continuously acquired while the sample temperature is increased using a heating ramp of 0.2 – 0.5 K s⁻¹. For temperature reading, K-type thermocouples are spotwelded directly to the sample. The manipulator head including sample, thermocouples and filament is shown in Figure 20.

In all experiments, a cylindrical Rh(111) single crystal purchased from MaTeck was used as substrate, which was cleaned by Ar⁺ sputtering, oxygen treatment at 900 K and annealing at 1200 K (~ 1 – 2 min). The cleanliness of the surface was checked by XPS. Prior to their use, all liquid substances were degassed by multiple freeze-pump-thaw cycles. Gases (purity of 99.95 %) were used without further purification.

All synchrotron radiation-based measurements were conducted at the electron storage ring BESSY II of the HZB. To this end, the above-described apparatus was attached to the open-port beamlines UE56/2 PGM1/2 and U49/2 PGM1[200]. During the beamtime, BESSY II was operated in multi-bunch top-up mode (300 mA ring current).

3.2 Data Acquisition and Processing

XPS was performed in normal emission with the photon incidence angle being 50°. When using synchrotron radiation, the photon energy was adjusted with regard to the core level under investigation, e.g., 380 eV for the C 1s region. Taking the high photon flux of synchrotron light into consideration, beam damage needs to be avoided, which was achieved by shifting the sample by about 0.1 mm (> X-ray beam diameter) between each measurement. NEXAFS was conducted in PEY mode at normal (0°) and grazing (70°) photon incidence angle. LEED images were recorded using a standard digital camera.

Processing of the XPS and NEXAFS data was done using custom procedures in IGOR Pro 6.22A. The XP spectra were referenced with respect to the Fermi edge. After background subtraction (mostly linear), the XP signals were fitted using a convolution of Doniach-Sunjic and Gaussian functions, thereby accounting for the asymmetry of the peaks (see Section 2.2). Coverage determination via XPS was carried out by comparison to reference samples with known surface coverage. Coverages are given in monolayers (ML) with 1 ML corresponding to one adsorbed atom/molecule per surface atom. The NEXFAS spectra were normalized regarding the ring current of the synchrotron light source, and therefrom reference spectra, taken of the clean Rh(111) single-crystal surface, were subtracted to cancel out beamline characteristics.

More detailed information regarding spectra acquisition, fitting and calibration is provided in the experimental sections and supplementary materials of [P1] – [P4].

3.3 “ARPES Chamber”

In the future, we plan to expand our repertoire of 2DMs by phosphorene and borophene. For these studies, we intend to use an UHV apparatus capable of angle-resolved PES (ARPES), XPS, UPS and LEED, the so-called “ARPES chamber”. However, this machine, which was formerly stationed at BESSY II, arrived at our laboratories in a desolate state. Hence, to proceed with our planned experiments, it was necessary to first renovate and partially reconstruct this chamber.

The “ARPES chamber” comprises an analyzer chamber, a preparation chamber, a sample garage and a load lock (Figure 21). The sample transfer between the individual chambers is performed via transfer forks and a respective sample holder. For the generation of UHV conditions, an array of pumps, including diaphragm, turbomolecular, titanium sublimation and ion getter pumps, are used. The load lock, attached to the sample garage, allows for introduction of samples into the apparatus without breaking the vacuum. In the sample garage (base pressure of $\sim 3 \times 10^{-8}$ mbar), which is connected to the preparation chamber, up to twelve samples can be stored. The preparation chamber (base

3 Experimental

pressure of $\sim 1 \times 10^{-10}$ mbar) is equipped with a manipulator, to which a voltage can be applied, a sputter gun for sample cleaning, an external filament for annealing, LEED optics and a QCM. In addition, several flanges are available to attach evaporators for the deposition of metals and other substances. The analyzer chamber (base pressure of $\sim 1 \times 10^{-10}$ mbar) houses a manipulator that allows for sample manipulation along three axes and three angles. The latter is also equipped with a filament to heat the sample from its back, thermocouples for temperature reading, a gold plate for referencing the binding energy and a QCM. Furthermore, a hemispherical electron energy analyzer capable of ARPES measurements (SPECS Phoibos 100), a UV light source (SPECS UVS 10/35), a dual-anode X-ray source (Scienta Omicron DSX400) and a QMS for residual gas analysis are attached to the analyzer chamber.

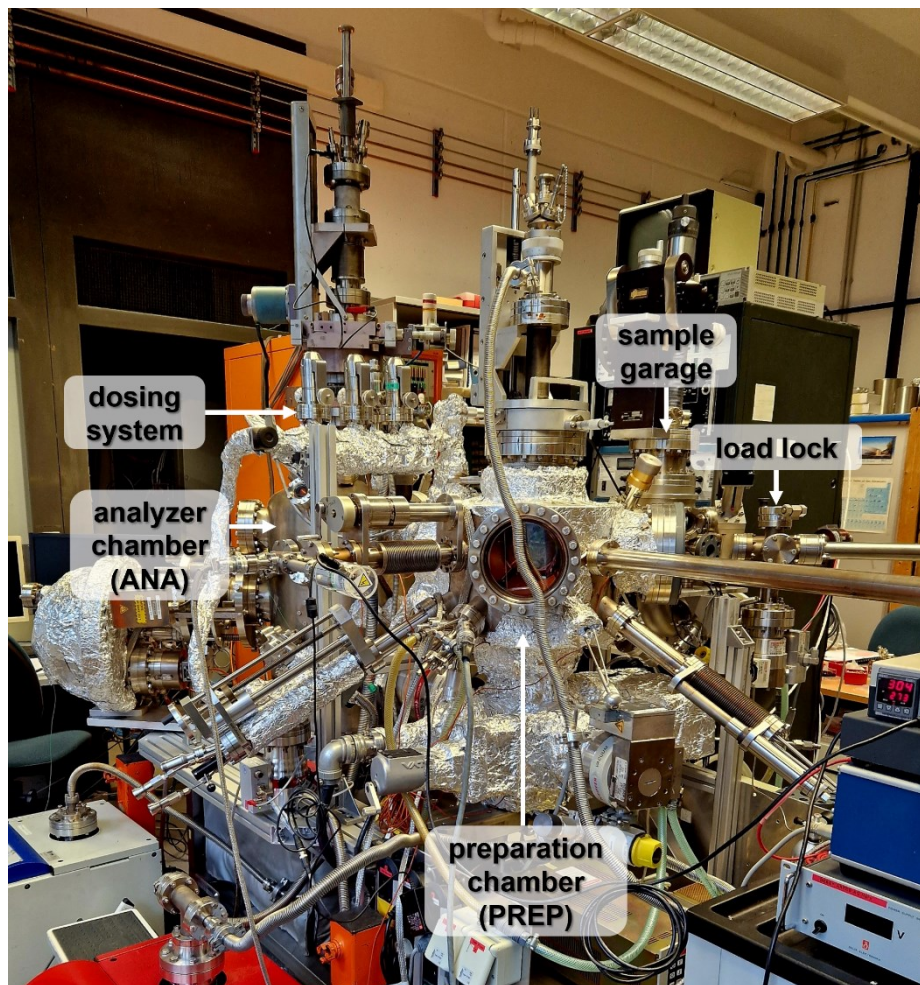


Figure 21. Photography of the “ARPES chamber”.

Figure 22 provides an insight into the preparation and analyzer chamber.

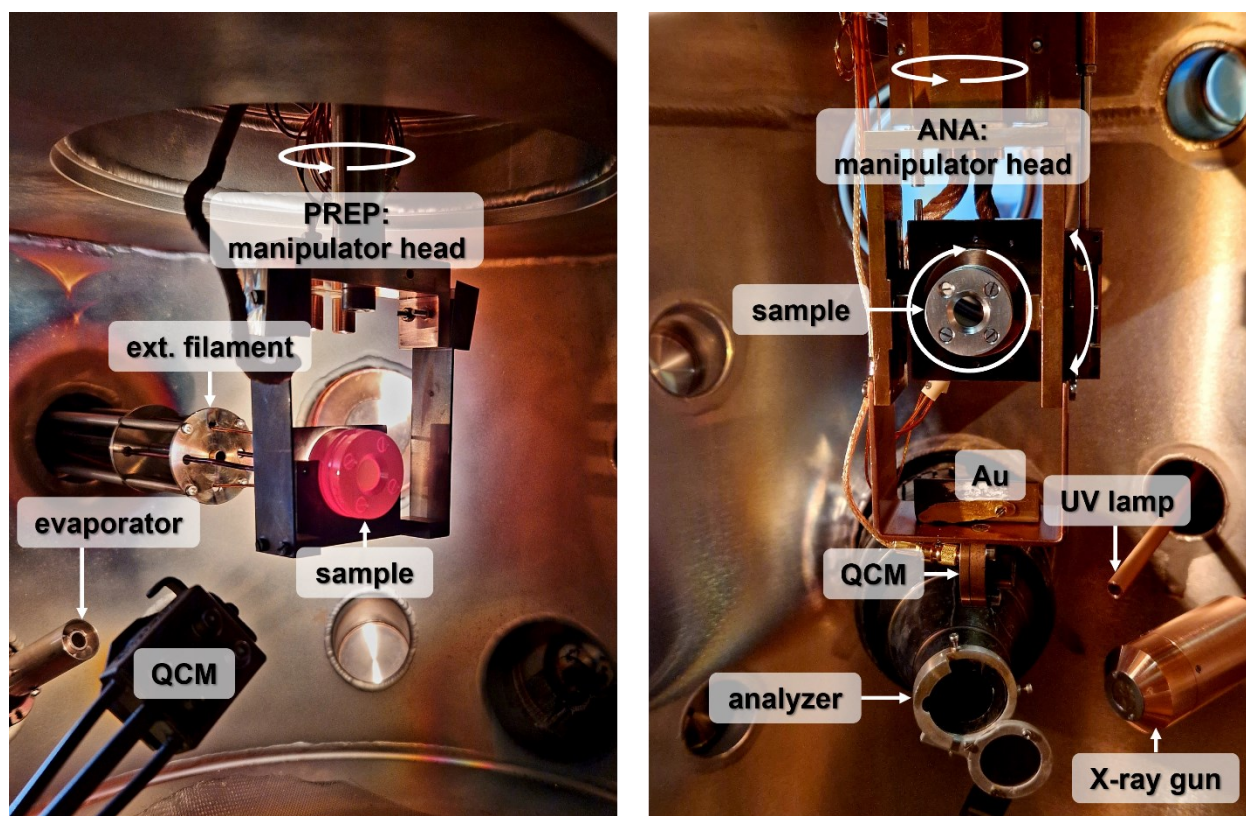


Figure 22. Insight into the preparation (left) and analyzer (right) chamber of the “ARPES chamber”.

For introduction of standard single crystals into the chamber, a new sample holder was designed and manufactured (Figure 23). The respective technical drawings are provided in Figures 34 – 36 in Appendix B. It enables mounting of square and round single crystals and heating of the sample from the back via filament heating. If the sample is too thin or too thick, additional spacers may be used to fixate the sample within the holder.

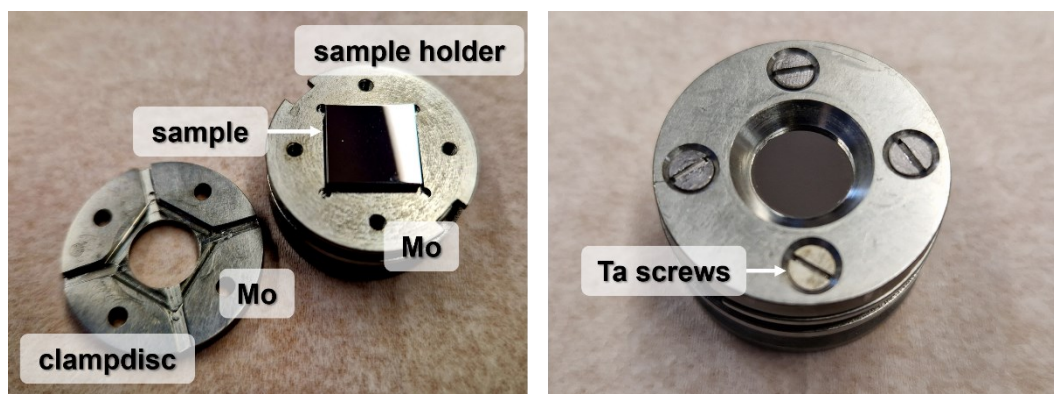


Figure 23. Sample holder designed for application in the “ARPES chamber”.

3 Experimental

Due to the limited ceiling height in our laboratories, the original cooling system for the analyzer chamber could not be applied. Thus, a new cooling lance, which can be split into several parts, was designed and manufactured (see Figures 37 and 38 in Appendix B for technical drawings). This allows for sample cooling by delivering liquid nitrogen down to the bottom of the manipulator rod using a vacuum pump.

To enhance the bakeout efficiency, bakeout blankets for the analyzer chamber were designed and purchased from HORST. The corresponding drawings can be found in Figures 39 and 40 in Appendix B.

4 The Surface Chemistry of Small Molecules on Rh(111)

For the study of complex systems, it is often of significant importance to understand the fundamental surface chemistry of each component. Ethylene and borazine are quite common precursors for the growth of transition metal-supported graphene and *h*-BN, respectively. In the context of 2DM functionalization, bromine is a promising candidate for halogenation, which can have a significant impact on the electronic properties of the 2DM and might serve as a good starting point for further modifications. To obtain a full insight into the bromination of Rh(111)-supported graphene and *h*-BN (see Chapter 5), a thorough investigation of ethylene, borazine and bromine on Rh(111) is a prerequisite. Thus, the adsorption and reaction of these small molecules on the Rh(111) single-crystal surface are addressed in the following. The insights gained in these studies, will also be useful in other research fields, such as heterogeneous catalysis and on-surface synthesis.

4.1 A High-Resolution X-Ray Photoelectron Spectroscopy Study on the Adsorption and Reaction of Ethylene on Rh(111) [P1]

This chapter summarizes the content of a published research article:[30]

E. M. Freiburger, F. Düll, C. Wichmann, U. Bauer, H.-P. Steinrück and C. Papp, A High-Resolution X-Ray Photoelectron Spectroscopy Study on the Adsorption and Reaction of Ethylene on Rh(111), *Chem. Phys. Lett.* **2022**, 797, 139595, DOI: [10.1016/j.cplett.2022.139595](https://doi.org/10.1016/j.cplett.2022.139595).

Ethylene is an important building block for the chemical industry. Thus, its reaction on metal surfaces, representing model heterogeneous catalysts, is of special interest as a detailed understanding in this regard helps to increase the efficiency of ethylene production and any processes in which ethylene is used as starting material or appears as a reaction intermediate. Apart from its important role in industry, ethylene can serve as a precursor to build up extended carbon-based nanostructures, such as graphene.[130] Rhodium can be utilized as catalytically active component in heterogeneous catalysis. For example, it is part of the three-way automotive catalyst.[201,202] In addition, rhodium-based catalysts are investigated with regard to the steam reforming of ethanol [203-205]

and selective catalytic dehydrogenation [206-208]. Due to its key role in various industrial processes and as precursor for the preparation of graphene, the surface chemistry of ethylene has been studied on many different metal surfaces, e.g., Pt(111) [209,210], Pd(111) [211,212], Ir(111) [213,214], Rh(111) [215-220], Rh(100) [221] and Rh(331) [216]. Our high-resolution *in situ* XPS study contributes to the existing literature by giving an insight into the adsorption and thermally induced reaction of ethylene on Rh(111).

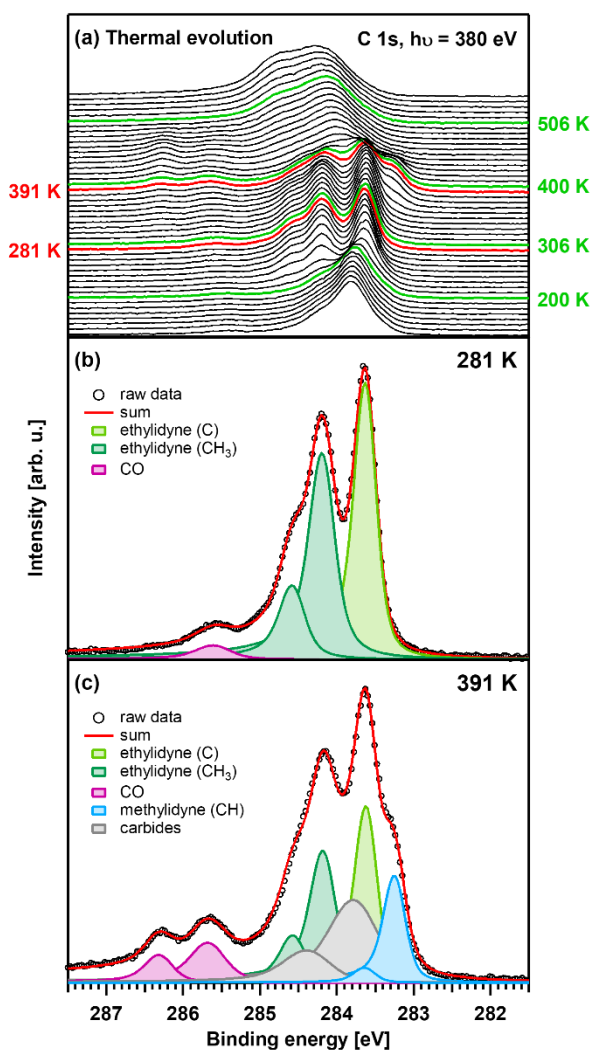


Figure 24. (a) Waterfall plot of the C 1s XP spectra recorded during heating ethylene/Rh(111) from 140 to 550 K in the scope of the TPXPS experiment. (b) and (c) Fits of C 1s spectra (marked red in (a)), visualizing the vibrational fine structure used for identification of the different surface species. Reproduced with permission from [30]. © 2022 Elsevier.

Using XPS, the low-temperature (140 K) adsorption of ethylene on Rh(111) was followed *in situ* in the C 1s core level. The use of synchrotron radiation allowed for a very high spectral resolution, enabling the vibrational fine structure of the adsorbate to be observed.

The XP spectrum revealed a dominating adiabatic peak and a smaller accompanying peak at higher binding energies, arising due to vibrational excitation. The so-called S factor equals the intensity ratio of the first vibrationally excited state and the adiabatic state.[176,178-180,222-224] For ethylene on Rh(111), we found an S factor of 0.27. The corresponding S factor per C-H bond (S/m value), which can in general be used to identify surface species [176,179], was determined to be ~ 0.14 . Since only one adiabatic peak was observed, we concluded that ethylene adsorbed molecularly in a symmetrical, bridged configuration on identical adsorption sites. TPXPS was used to monitor the thermally induced reaction of ethylene on Rh(111) in a temperature range from 140 to 550 K. The corresponding spectra are depicted as a waterfall plot in Figure 24a. Figures 24b and 24c show fits at selected temperatures. The reaction intermediates were identified according to their vibrational fine structure. Ethylene (CH_2CH_2) was found to be stable up to ~ 200 K. Above 200 K, ethylidyne (CCH_3) evolved, presumably adapting an up-standing configuration on a three-fold hollow site. This species remained stable for about 150 K. Between 350 and 440 K, ethylidyne decomposed, forming methylidyne (CH) and carbide. Methylidyne, which is also assumed to occupy a three-fold hollow site, peaked at approximately 390 K. Eventually, it also decomposed to carbides, which are the only species left at temperatures above 460 K. In heterogeneous catalysis, the early decomposition of ethylene on Rh(111) represents a severe challenge in terms of catalyst deactivation due to coking of the surface. Also, the quality of Rh(111)-supported graphene, prepared via CVD of ethylene, might suffer from this. Figure 25 shows a scheme visualizing the reaction pathway of ethylene on Rh(111).

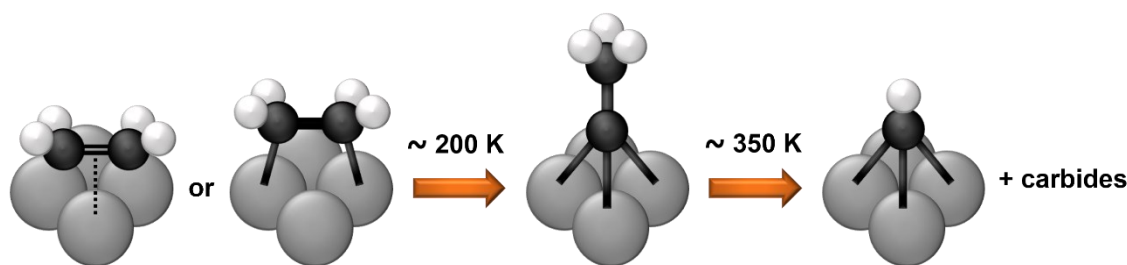


Figure 25. Proposed reaction pathway for ethylene on Rh(111). Adapted with permission from [30].
© 2022 Elsevier.

This study, providing a deep insight into the surface chemistry of ethylene on Rh(111), proved that analyzing the vibrational fine structure of XPS peaks is a highly useful tool for the identification of adsorbates.

Adapted with permission from [30]. © 2022 Elsevier.

4.2 *h*-BN in the Making: The Surface Chemistry of Borazine on Rh(111) [P2]

This chapter summarizes the content of a published research article:[54]

E. M. Freiburger, F. Düll, P. Bachmann, J. Steinhauer, F. J. Williams, H.-P. Steinrück and C. Papp, *h*-BN in the Making: The Surface Chemistry of Borazine on Rh(111), *J. Chem. Phys.* **2024**, 160, 154706, DOI: [10.1063/5.0202431](https://doi.org/10.1063/5.0202431).

Borazine, being isoelectronic and isostructural with benzene, is the most commonly used precursor molecule for the CVD growth of *h*-BN [225], whose properties are outlined in Chapter 1.3. If *h*-BN is grown on Rh(111) as substrate, a corrugation of the overlayer arises due to the lattice mismatch of Rh(111) and *h*-BN. The resulting nanomesh, in which 12×12 Rh(111) unit cells are covered with 13×13 *h*-BN unit cells, exhibits a periodicity of 3.2 nm.[226-228] As described in Chapter 1.3, this nanomesh can act as template for selective 2DM functionalization with atoms and molecules and the directed deposition of nanostructures.[132] Previous studies, aiming at elucidation of the evolution of the *h*-BN/Rh(111) nanomesh from borazine, utilized STM [229] or TPD and high-resolution electron energy loss spectroscopy (HR-EELS) [230]. We complemented this research by performing an *in situ* study on the surface chemistry of borazine on the Rh(111) single-crystal surface using high-resolution XPS, TPXPS and NEXAFS.

XPS was employed to follow the adsorption of borazine on Rh(111) at 130 K *in situ* in the B 1s and N 1s core levels. In the B 1s XP spectra, molecular borazine as well as different borazine fragments were observed. We found that the individual species differed from each other with respect to the number of nitrogen atoms bound to boron (BN₂, BN and B): the more nitrogen neighbors, the higher the observed binding energy. Also, in the N 1s region, borazine and its fragments were observed. For high exposures, the formation of a multilayer was indicated by an additional signal at the high binding energy side.

Overall, the individual XPS fingerprint of borazine on Rh(111) revealed a dominating borazine peak accompanied by smaller peaks at lower binding energies that are associated with fragments. Thus, we propose that borazine adsorbed mostly as an intact molecule. Additionally, the impact of borazine adsorption on the rhodium substrate was investigated via an analysis of the Rh 3d spectra taken prior to and after borazine adsorption. Upon adsorption, a distinct surface core level shift occurred, from which we derived a pronounced interaction between borazine and Rh(111).

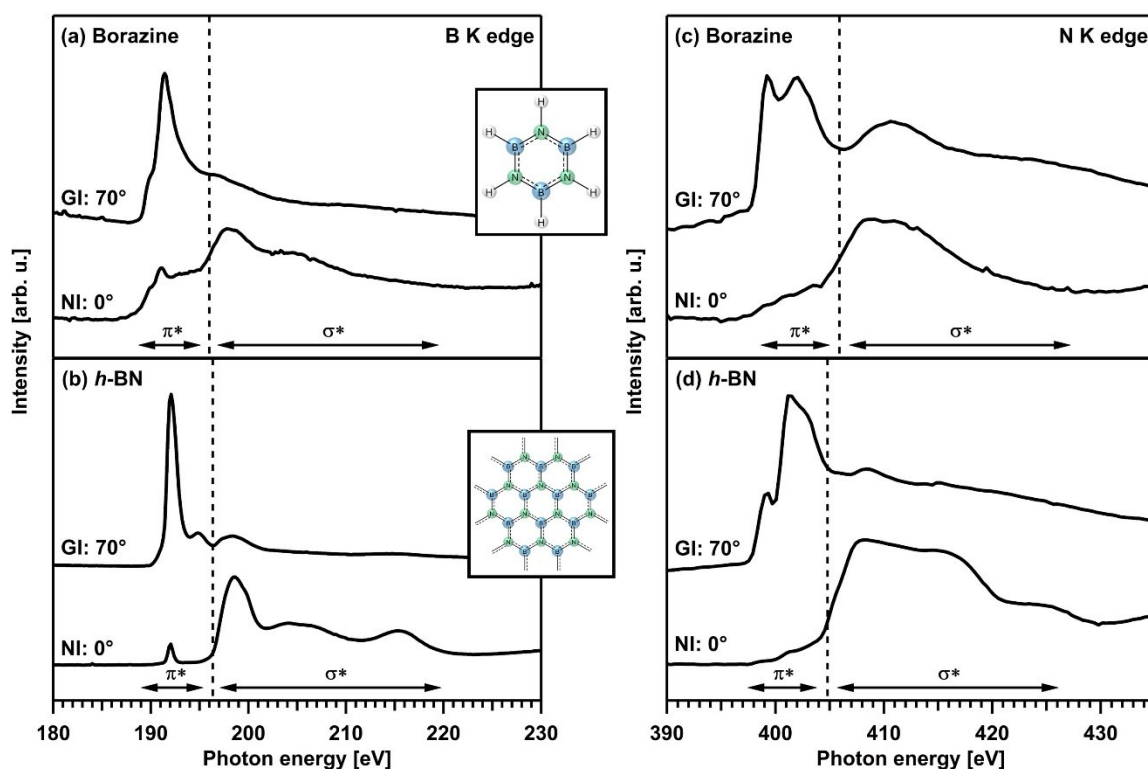


Figure 26. GI and NI NEXAFS spectra of the (a) B K-edge of borazine/Rh(111), (b) B K-edge of *h*-BN/Rh(111), (c) N K-edge of borazine/Rh(111) and (d) N K-edge of *h*-BN/Rh(111). The dashed black lines mark the onset of the σ^* region, taken as an estimate for the IP. Adapted from [54], with permission of AIP Publishing. © AIP Publishing.

The adsorption geometry of borazine on Rh(111) was examined using NEXAFS. To this end, spectra at the boron and nitrogen K-edge were recorded at NI (0°) and GI (70°). For 70° incidence, intensive signals were observed in the π^* region, which were hardly visible in the 0° incidence spectra. This indicated that borazine adsorbed with the plane of the six-membered ring oriented parallel to the surface. In Figure 26, the NEXAFS spectra of borazine and *h*-BN on Rh(111) are shown.

The thermally induced reaction of borazine on Rh(111), eventually leading to the formation of the *h*-BN/Rh(111) nanomesh, was studied by TPXPS. A careful fit of the B 1s spectra, recorded during heating from 130 to 1100 K, allowed for the identification of several surface species, that are, molecular borazine, $B_xN_yH_z$ species, dehydrogenated B_xN_y species, disordered boron nitride and *h*-BN. The corresponding spectra, selected fits and a quantitative analysis of the TPXPS experiment are provided in Figure 27.

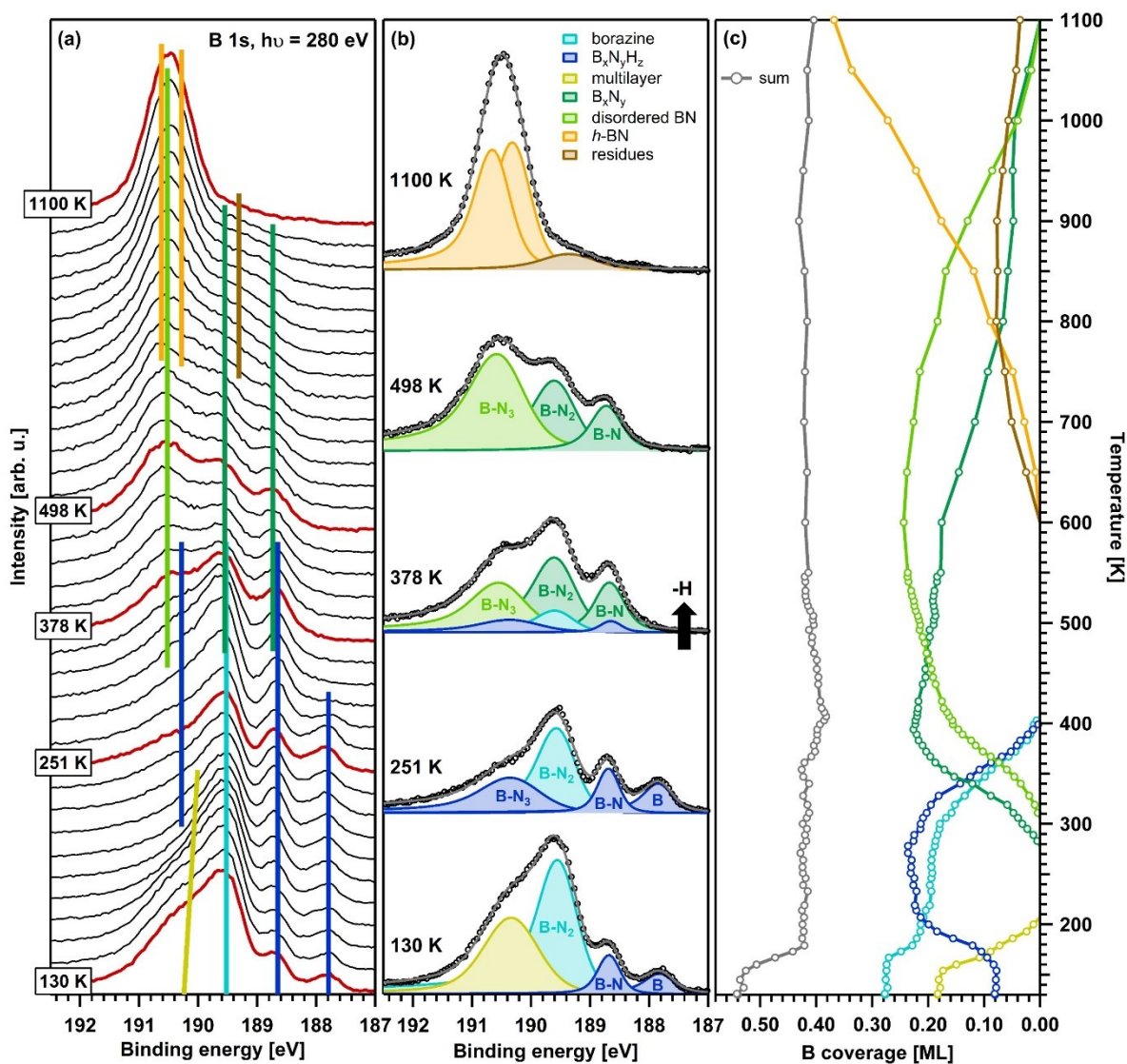


Figure 27. (a) Waterfall plot of the B 1s XP spectra recorded during heating borazine/Rh(111) from 130 to 1100 K in the scope of the TPXPS experiment. The fit species are indicated by respectively colored lines. (b) Fits at selected temperatures (marked red in (a)). (c) Quantitative analysis of the TPXPS data. Reproduced from [54], with permission of AIP Publishing. © AIP Publishing.

Upon heating, the multilayer desorbed already below 200 K. At about 250 K, borazine and borazine fragments ($B_xN_yH_z$), characterized by a varying number of nitrogen

neighbors (BN_3 , BN_2 , BN , B), were found to remain on the surface. Above room temperature, we proposed, taking a previous study by Farkas *et al.* into consideration [230], dehydrogenation to occur, resulting in B_xN_y species. Simultaneously, disordered boron nitride evolved. At 650 K, the formation of the *h*-BN nanomesh set in. The conversion to *h*-BN was seemingly complete at 1100 K (except for small amounts of boron). The obtained surface species was confirmed to be the desired 2DM by comparison with *h*-BN/Rh(111), prepared according to an established procedure [45].

By means of synchrotron radiation-based surface science, the adsorption of borazine on Rh(111) and the gradual evolution of the *h*-BN/Rh(111) nanomesh were studied *in situ*: “*h*-BN in the making”.

Adapted from [54], with permission of AIP Publishing. © AIP Publishing.

4.3 Bromine Adsorption and Thermal Stability on Rh(111): A Combined XPS, LEED and DFT Study [P3]

This chapter summarizes the content of a published research article:[74]

E. M. Freiberger, J. Steffen, N. J. Waleska-Wellnhofer, A. Harrer, F. Hemauer, V. Schwaab, A. Görling, H.-P. Steinrück and C. Papp, Bromine Adsorption and Thermal Stability on Rh(111): A Combined XPS, LEED and DFT Study, *ChemPhysChem* **2023**, 24, e202300510, DOI: [10.1002/cphc.202300510](https://doi.org/10.1002/cphc.202300510).

Halogens may be involved in various surface-related processes, e.g., as by-product in on-surface synthesis and electrochemistry or as promoter in heterogeneous catalysis, as has been emphasized in Chapter 1.2, which renders their chemistry on metal surfaces a subject of huge research interest. In our study, we shed light on the surface chemistry of bromine on Rh(111) by means of high-resolution XPS, TPXPS, LEED and density functional theory (DFT) calculations. The latter were performed by Dr. J. Steffen in the scope of a collaboration with the Chair of Theoretical Chemistry of FAU, headed by Prof. Dr. A. Görling.

The adsorption process of bromine on Rh(111) at 170 K was followed *in situ* by XPS in the Br 3d core level. A waterfall plot of the Br 3d spectra recorded in the course of the adsorption process and fits at selected coverages are shown in Figures 28a and 28b, respectively.

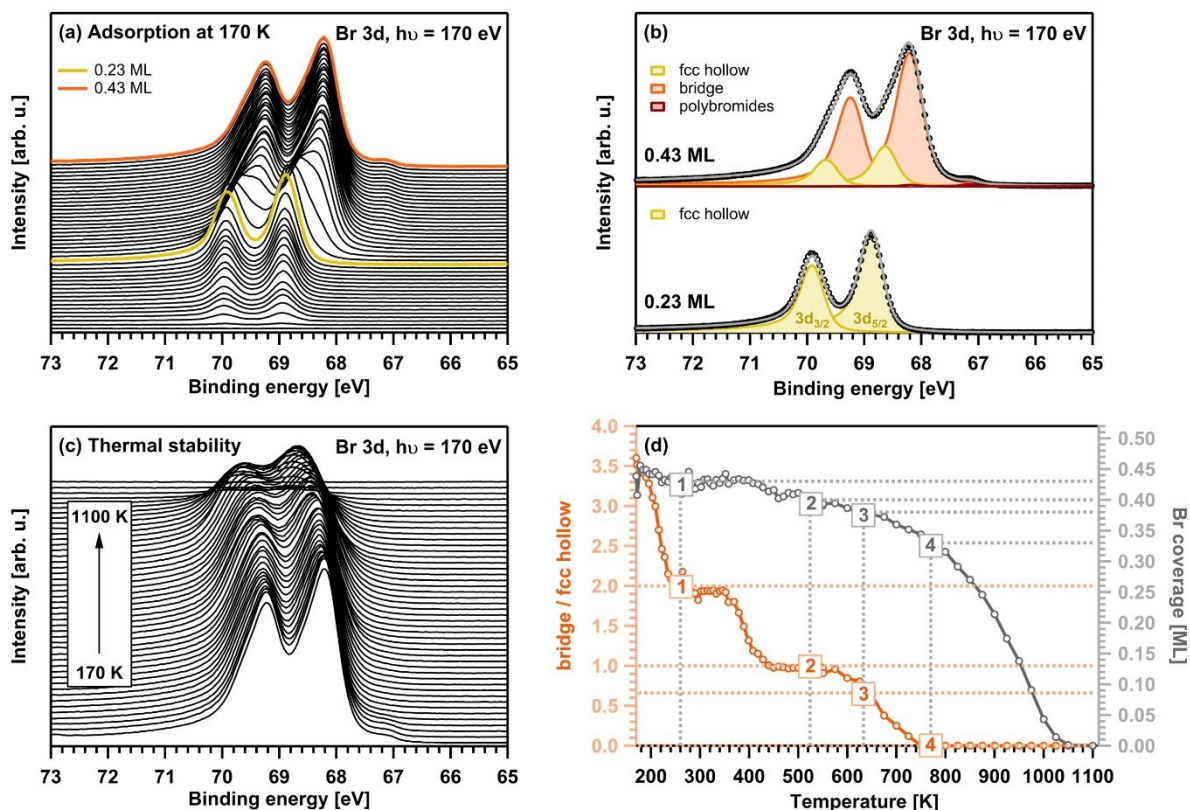


Figure 28. (a) Waterfall plot of the Br 3d spectra recorded upon bromine adsorption on Rh(111) until saturation (0.43 ML). (b) Fits at selected coverages (marked in (a)). (c) Waterfall plot of the Br 3d spectra recorded upon heating from 170 to 1100 K in the scope of the TPXPS experiment. (d) Quantitative analysis of the TPXPS experiment, showing the bromine coverage (gray) as well as the ratio between bridge- and fcc hollow-bound bromine (orange) as a function of the temperature. 1 – 4 correspond to the four LEED patterns found for Bromine on Rh(111). Reproduced with permission from [74]. © 2023 Wiley-VCH GmbH.

Since halogens usually adsorb in a dissociative manner [231], we assumed bromine to adsorb atomically. First, at low coverage, only one species characterized by a spin-orbit-split Br $3d_{3/2}/3d_{5/2}$ doublet was observed. Upon increasing bromine exposure, a second doublet, i.e., a second bromine species, appeared at lower binding energies, which became the dominating signal at saturation coverage (0.43 ML). In addition, the initial doublet was significantly shifted to lower binding energies, indicating strong adsorbate-adsorbate interaction. LEED and DFT were performed to identify the different bromine

species observed. We found that the low-coverage species (≤ 0.33 ML) belonged to bromine adsorbed on fcc hollow sites while, at higher coverages (0.33 – 0.43 ML), bromine was forced to also occupy bridge sites (= high-coverage species). In general, an fcc hollow-bound atom binds to three substrate atoms, whereas a bridge-bound atom binds to two substrate atoms.

The thermal stability of bromine/Rh(111) was then examined using TPXPS. To this end, Br 3d spectra were taken in the temperature range from 170 to 1100 K (Figure 28c). Along with heating, the coverage decreased, and the second bromine species observed upon adsorption gradually disappeared, that is, the compression-induced shift of the bromine atoms was reversed (see quantitative analysis of the TPXPS experiment in Figure 28d). Overall, a quite high thermal stability of bromine/Rh(111) up to above 1000 K was noticed, indicating strong covalent bonding.

In LEED, a complex, star-shaped diffraction pattern arose for the saturation coverage of 0.43 ML bromine (Figure 29a). By simulation using the software LEEDpat4 provided by the Fritz Haber Institute of the Max Planck Society [232], we found this pattern to result from the superposition of three symmetry-equivalent domains, rotated to each other by 120° . Upon annealing and therewith decreasing of the surface coverage, additional diffraction spots appeared and the distances between the spots became smaller (Figures 29b and 29c). Reaching 700 K, at which the surface coverage was reduced to about 0.33 ML, a sharp $(\sqrt{3} \times \sqrt{3})R30^\circ$ pattern evolved (Figure 29d). The bromine-induced diffraction spots disappeared only upon annealing at 1000 K, matching the high thermal stability determined in the TPXPS experiment. Laboratory-based XPS was used to verify the coverage-dependency of the LEED patterns. In addition, it proved the low-coverage species in XPS to be associated with the $(\sqrt{3} \times \sqrt{3})R30^\circ$ superstructure, while the star-shaped patterns could only be observed when both XPS species were present.

Depending on the respective surface coverage, we found overall four different LEED patterns for bromine on Rh(111). From simulation of these patterns, the corresponding real-space unit cells and their individual coverages were derived. Based on the unit cells

and the Br coverage, DFT was used to identify the most stable adsorption configuration for each case. The most stable adsorption site for bromine was found to be the fcc hollow site. At low coverages (≤ 0.33 ML), all bromine atoms were located on such fcc hollow sites. However, for higher coverages, a compression-induced shift of the bromine atoms to the energetically less favorable bridge sites occurred. Finally, at saturation coverage, 2/3 of the bromine atoms occupied bridge sites while only 1/3 remained on the fcc hollow sites. Figure 29 provides the four LEED patterns along with the corresponding LEEDpat4 simulations and the calculated real-space structures.

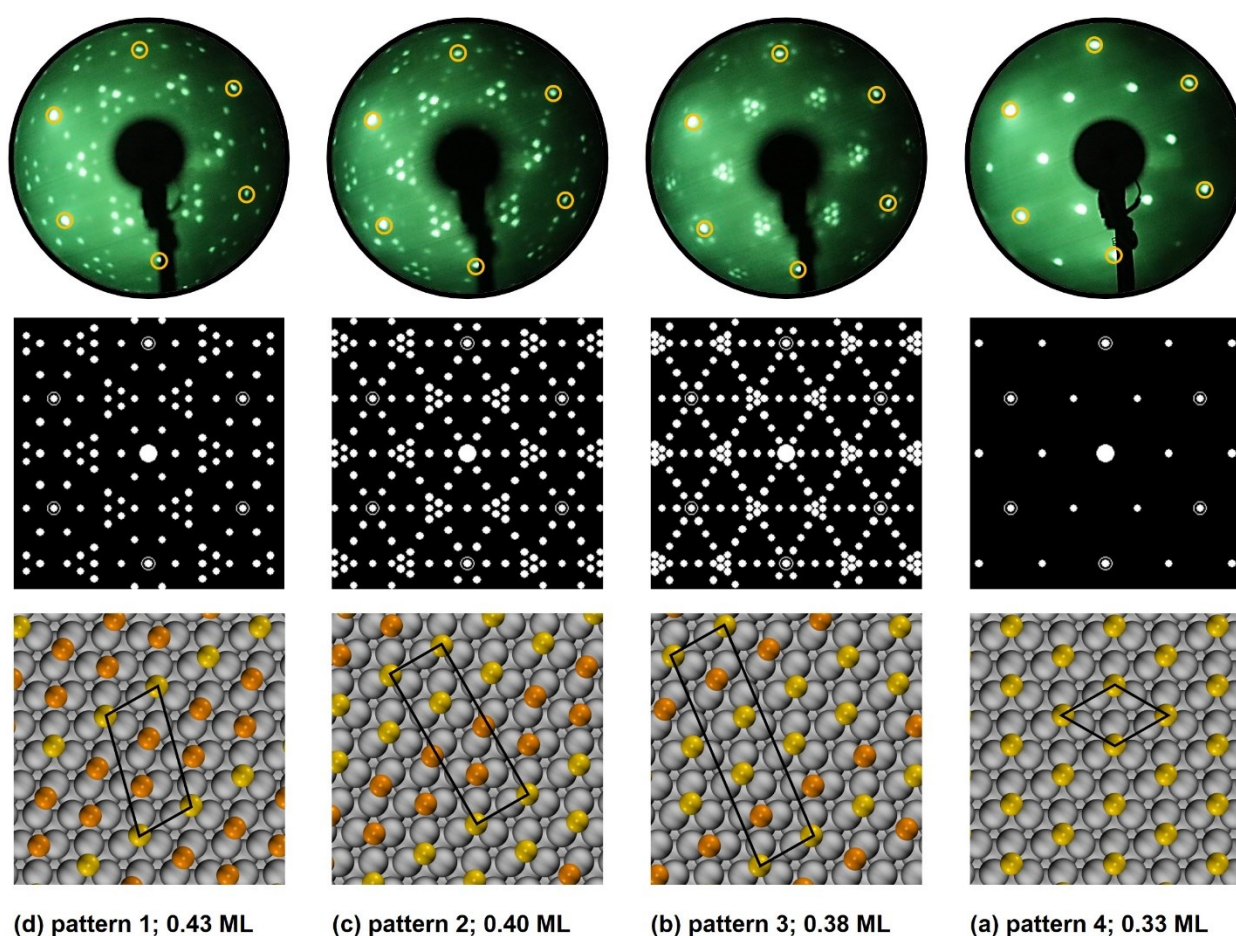


Figure 29. (a) – (d) Experimental LEED patterns (substrate diffraction spots marked by yellow circles), corresponding LEEDpat4 simulations (reciprocal space) and most stable real-space models for four different coverages. Fcc hollow- and bridge-bound bromine atoms are colored yellow and orange, respectively. The respective unit cells are indicated in black. Adapted with permission from [74]. © 2023 Wiley-VCH GmbH.

This study on the surface chemistry of bromine on Rh(111) demonstrated the synergistic effect of the combination of several experimental and theoretical surface science

techniques for the investigation of surface processes on the molecular level. Using XPS, LEED and DFT, we accessed adsorption sites, adsorption energies, the long-range order and the thermal stability. In this context, the coverage-dependent compression of the bromine adlayer on Rh(111) was observed for the first time.

Figure 30 illustrates the findings of this study in an abstract fashion. This graphic was used for a ChemPhysChem cover feature published along with the research article.[233]

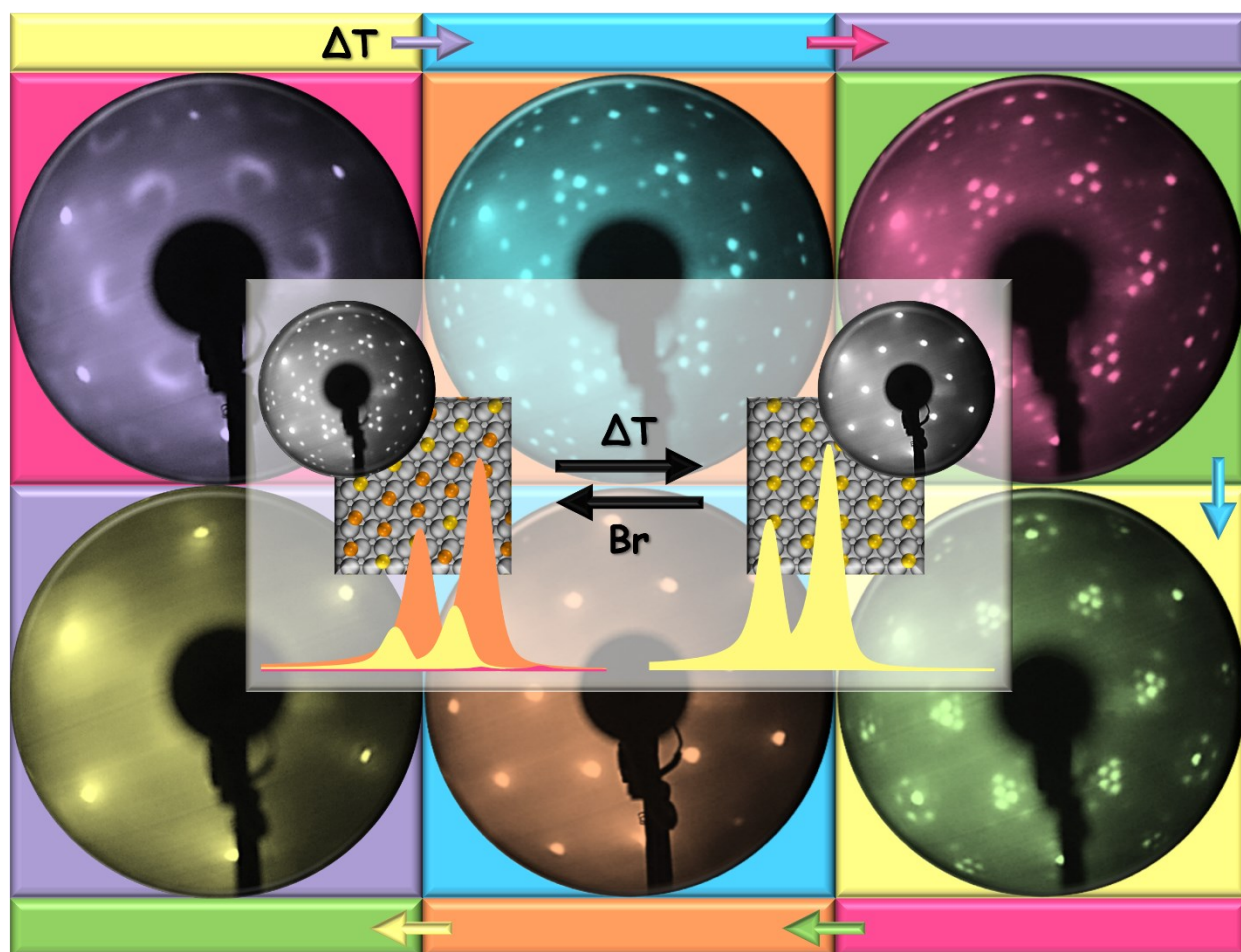


Figure 30. Illustration of the main findings of the study on bromine adsorption and thermal stability on Rh(111). Reproduced with permission from [74]. © 2023 Wiley-VCH GmbH.

Adapted with permission from [74]. © 2023 Wiley-VCH GmbH. All rights reserved, including rights for text and data mining and training of artificial intelligence technologies or similar technologies.

5 Bromination of 2D Materials [P4]

This chapter summarizes the content of a published research article:[165]

E. M. Freiberger, J. Steffen, N. J. Waleska-Wellnhofer, F. Hemauer, V. Schwaab, A. Görling, H.-P. Steinrück and C. Papp, Bromination of 2D Materials, *Nanotechnology* **2024**, 35, 145703, DOI: [10.1088/1361-6528/ad1201](https://doi.org/10.1088/1361-6528/ad1201).

This research article addresses the bromine functionalization of Rh(111)-supported graphene, grown from ethylene, and *h*-BN, grown from borazine, which combines the knowledge gained in the three publications summarized in Chapter 4 in the scope of a more complex surface science study.

Graphene and *h*-BN (see Chapter 1.3 for an overview of their synthesis, properties and applications) exhibit a corrugated structure on Rh(111), commonly referred to as moiré/nanomesh.[133,134] The valleys/pores are in close contact to the substrate and thus strongly interact with the Rh(111) surface, from which a pronounced reactivity of these regions is expected. The hills/wires, on the other hand, behave more like the free-standing 2DMs. Therefore, the moiré/nanomesh can be used as a template for confined nanostructures [132,135], but also for the directed, selective functionalization of the 2DMs [164]. Functionalization is a versatile tool to achieve tuning of the intrinsic properties of 2DMs, which is crucial to their application in real-world devices, as has been thoroughly discussed in Chapter 1.3. In this context, the halogenation of a 2DM, e.g., with bromine, is a promising approach to alter the electronic properties of the respective 2DM and to arrive at a good starting point for further functionalization with small molecules [234]. Combining high-resolution *in situ* XPS and TPXPS and a comprehensive theoretical study, including DFT calculations and molecular dynamics (MD), we presented a detailed study on the reactivity of Rh(111)-supported *h*-BN and graphene towards bromine, providing exclusive insights into these systems on the molecular level. The theoretical study was carried out by Dr. J. Steffen (shared first author) in the scope of a collaboration with the Chair of Theoretical Chemistry of FAU, headed by Prof. Dr. A. Görling.

First, the adsorption and reaction of bromine on the *h*-BN/Rh(111) nanomesh was probed experimentally via XPS and TPXPS in the N 1s, B 1s and Br 3d core levels. The N 1s and B 1s spectra of pristine *h*-BN/Rh(111) are usually characterized by two contributions for the pores and wires of the nanomesh, which could also be observed in our data recorded prior to bromine exposure. Upon bromine adsorption, we found, in the N 1s as well as B 1s spectra, distinct changes in the pore region: A new peak associated with the functionalized pore evolved and gradually replaced the original pristine pore peak. Simultaneously, the wire region remained largely unaffected. Thus, we concluded that, at least for low coverages, bromine functionalization was confined to the pores, demonstrating the template effect of the nanomesh. After heating to 800 K, the N 1s and B 1s spectra regained their original appearance, i.e., were identical with the spectra of pristine *h*-BN/Rh(111), indicating that the selective functionalization was fully reversible upon annealing. In the Br 3d core level, the adsorption of two different coverages of bromine were investigated. For low coverages, only one spin-orbit-split Br 3d_{3/2}/3d_{5/2} doublet was found, corresponding to a single bromine species on the surface. Taking the N 1s and B 1s data into consideration, this species was attributed to molecular bromine selectively adsorbed in the pores of the nanomesh. Exceeding a surface coverage of 0.14 ML bromine, the pores were saturated and further doublets started to grow that were assigned to adsorption on the wires (or polybromides) and multilayer formation. To examine the surface chemistry of bromine adsorbed in the pores, a TPXPS experiment was conducted in the Br 3d region right after low-coverage bromine adsorption (<0.14 ML, exclusively pore species). Figures 31a and 31b show the Br 3d spectra recorded during heating of Br/*h*-BN/Rh(111) from 170 to 800 K as a waterfall plot and the corresponding density plot, respectively. For a better understanding of the ongoing processes, a thorough fit (Figure 31c) and a quantitative analysis of the TPXPS experiment (Figure 31d) were performed. Upon heating, molecular bromine (Br₂) underwent an on-surface reaction, and two additional doublets developed at lower binding energies, which were attributed to polybromides, presumably Br³⁻ and Br⁵⁻. The latter were observed between 170 and 240 K until they decomposed to bromide (Br⁻), the fourth doublet

appearing in the course of the TPXPS experiment. Bromide remained on the surface up to about 640 K, indicating a rather strong covalent bonding to *h*-BN/Rh(111). Interestingly, the observed desorption temperature decreased with increasing initial surface coverage. Thus, at low coverages, diffusion limitation seemed to play a role for desorption.

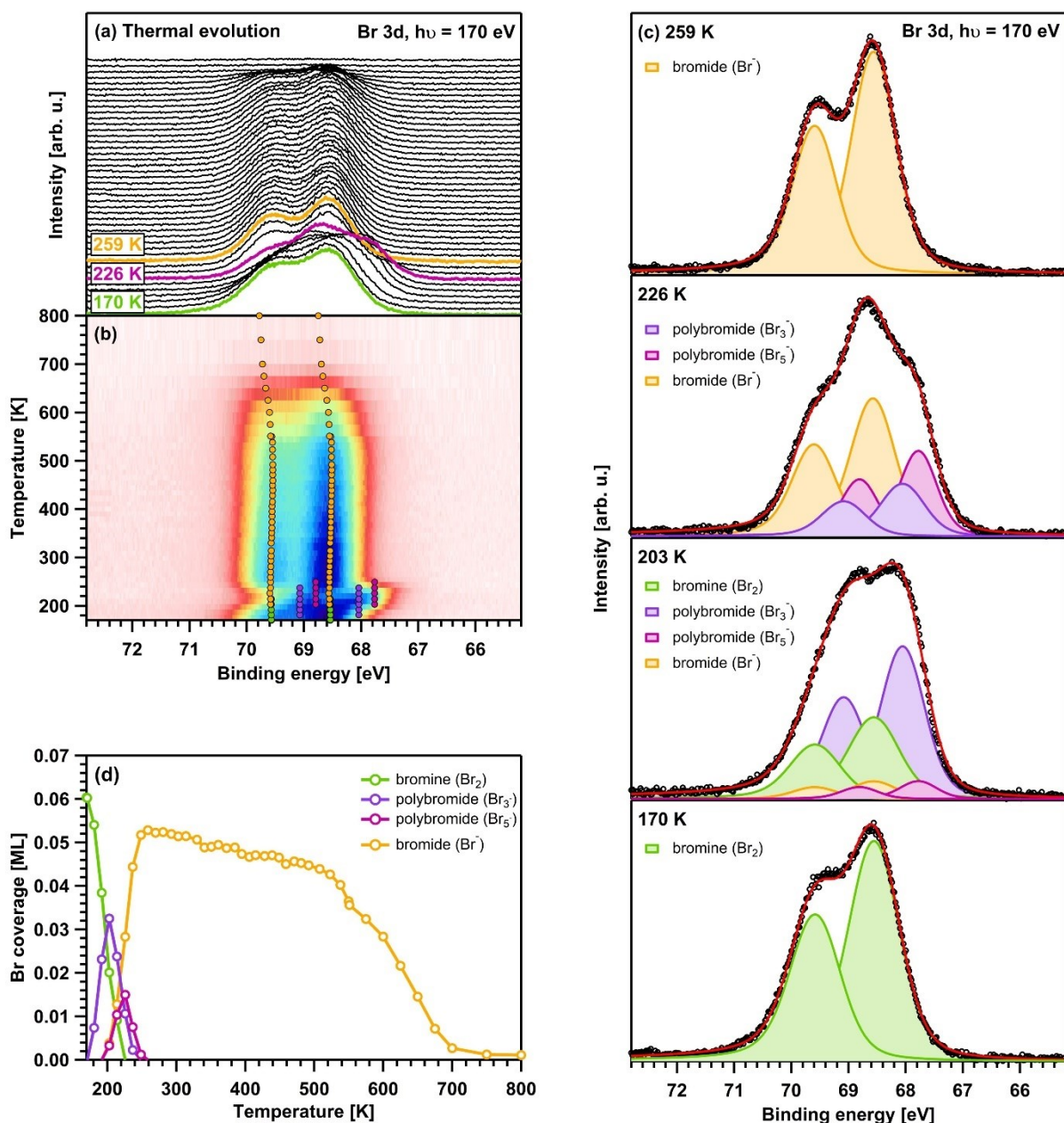


Figure 31. (a) Waterfall plot of the Br 3d spectra recorded upon heating from 170 to 800 K in the scope of the TPXPS experiment. (b) Corresponding density plot with the fit species being indicated by respective colored dots. (c) Fits at selected temperatures. (d) Quantitative analysis of the TPXPS data. Reproduced from [165] under license CC BY 4.0 DEED. © IOP Publishing.

In addition, the bromination of graphene/Rh(111) was studied. The C 1s spectra showed no pronounced changes regarding the valleys. Instead, all components revealed a shift to lower binding energies, induced by doping, and an overall dampening of their intensities. Moreover, an additional signal at higher binding energies was observed that stemmed from interaction of graphene and bromine. Thus, from the C 1s data, no spatial selectivity of the bromine adsorption on the graphene moiré was deduced. In the Br 3d core level, several doublets, assigned to bromine in the valleys, bromine on the hills and multilayer formation, evolved almost simultaneously. This also indicated that the graphene moiré did not serve as a template for selective functionalization. Upon heating, most bromine already desorbed below room temperature, and the adsorbate-induced effects observed in the C 1s spectra were reversed, which showed reversibility of the adsorption process and a rather low thermal stability of the bromine species adsorbed on graphene/Rh(111).

The experimental findings were supported by a theoretical study to learn about the above-investigated systems in even greater detail. Using DFT, optimized structural models of the *h*-BN/Rh(111) nanomesh and the graphene/Rh(111) moiré were obtained. For the *h*-BN nanomesh, a stronger buckling of the overlayer was found than for the graphene moiré, which we proposed to cause a pronounced difference regarding the chemical reactivity of the pores and wires, enabling selective adsorption. In addition, the binding energies of boron molecules and atoms on Rh(111)-supported graphene and *h*-BN were calculated. For *h*-BN/Rh(111), the outcome of these calculations suggested that bromine molecules and atoms bind preferentially to boron atoms in the pores of the nanomesh (Figure 32) while wire adsorption was shown to be energetically unfavorable. A Bader charge analysis showed that the nanomesh is indeed polarized in such a way that the boron atoms are positively, and the nitrogen atoms are negatively charged, which we supposed to be the driving force for boron being the preferential adsorption site. In the case of graphene/Rh(111), the adsorption in the valleys was found to be more stable than on the hills. However, for both regions, negative binding energies were determined, indicating that valley as well as hill adsorption are energetically feasible. Collectively,

these observations matched the experimental results and provided a tangible explanation for the selectivity found for bromination of *h*-BN/Rh(111).

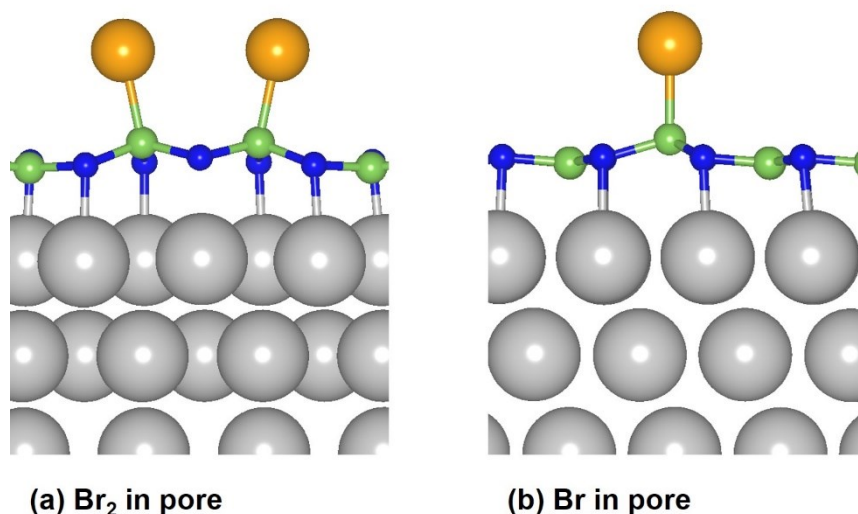


Figure 32. Optimized structures of (a) molecular boron and (b) atomic boron bound in the pores of the *h*-BN/Rh(111) nanomesh. Boron, nitrogen, bromine and rhodium atoms are colored green, blue, orange and gray, respectively. Reproduced from [165] under license CC BY 4.0 DEED. © IOP Publishing.

In the scope of the theoretical study, the pore adsorption of bromine on *h*-BN/Rh(111) was further investigated. Placing an increasing number of bromine molecules into the pores, we observed individual bromine molecules up to a coverage of 0.13 ML, bromine clusters (polybromides) for coverages > 0.13 ML and eventually wire adsorption and multilayer formation after reaching pore saturation at approximately 0.18 – 0.19 ML. Additionally, the desorption energetics of bromine were examined, revealing wire adsorption and multilayers to be thermally rather unstable. In terms of pore adsorption, a significantly higher thermal stability was found, which decreased with increasing pore coverage. These additional results regarding the adsorption of bromine in the *h*-BN pores were almost perfectly in line with our experimental findings.

Finally, the adsorption behavior of bromine on the *h*-BN nanomesh was simulated by means of MD using a machine-learning force field. This represented a novel approach, demonstrating the possibility to perform MD of such expanded systems in a feasible

manner. The MD simulation also confirmed the pore selectivity of the bromine functionalization (Figure 33).

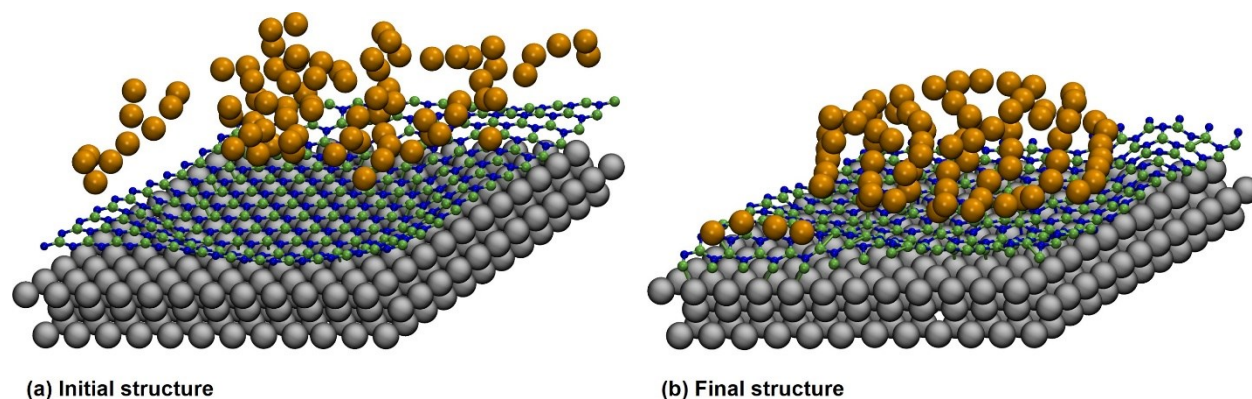


Figure 33. MD simulation starting from (a) 40 bromine molecules placed above the empty pore and resulting in (b) pore adsorption and multilayer formation. Boron, nitrogen, bromine and rhodium atoms are colored green, blue, orange and gray, respectively. Reproduced from [165] under license CC BY 4.0 DEED. © IOP Publishing.

The reactivity of Rh(111)-supported graphene and *h*-BN towards bromine was studied in vast detail using a combination of experimental and theoretical surface science tools. For the *h*-BN/Rh(111) nanomesh, selective covalent functionalization of the pores was achieved. The possibility to perform chemical modification of 2DMs in a selective way is key to the fine tuning of their unique properties and hence inevitable for their use in real-world applications.

Adapted from [165] under license CC BY 4.0 DEED. © IOP Publishing.

6 Summary and Outlook

This cumulative dissertation is dedicated to fundamental surface science studies on the adsorption and reaction of small molecules on the Rh(111) single-crystal surface and Rh(111)-supported 2DMs under UHV conditions. Experimental and theoretical methods were combined to gather comprehensive insights on the molecular level, that is, to elucidate individual surface species, adsorption geometries, adsorption sites, long-range periodicity, thermally induced reaction pathways and thermal stabilities. Knowledge in this regard is helpful for the investigation of complex systems and to eventually understand and improve real-world industrial applications. The main technique used in the present work was synchrotron radiation-based high-resolution *in situ* XPS. Depending on the respective system under investigation, XPS was complemented by NEXAFS, LEED and/or theory. Four research articles (see Appendix A) constitute this dissertation:

[P1] (see Chapter 4.1) dealt with the adsorption and thermally induced reaction of ethylene (C_2H_4) on Rh(111), studied *in situ* by means of XPS and TPXPS. Small hydrocarbons, such as ethylene, adsorbed on metal surfaces are insightful reference systems for heterogeneous catalysis as well as readily available precursors for graphene growth. At 140 K, ethylene adsorbed molecularly in a bridged configuration on identical surface sites, which was deduced from the C 1s spectrum acquired upon adsorption. In the TPXPS experiment, ethylene/Rh(111) was heated to 550 K, which was monitored by continuously recorded XP spectra in the C 1s core level. Reaction intermediates that evolved during the thermally induced reaction of ethylene were identified according to the vibrational fine structure of their XPS signals. Upon heating, ethylene remained stable up to approximately 200 K. At this temperature, a new surface species developed, which we assigned to ethylidyne (CCH_3), adapting an up-standing adsorption geometry. Starting at about 350 K, ethylidyne decomposed to form methylidyne (CH) and carbides. Above 460 K, only carbides were observed to remain on the surface. The early decomposition to carbides represents a severe challenge since coking deactivates the

catalytic Rh(111) surface, which is undesirable for the design of rhodium-based real-world catalysts. Also, in the case of CVD growth of graphene from ethylene, carbides are often observed as unwanted by-products, lowering the quality of the 2D layer.

In [P2] (see Chapter 4.2), we studied the adsorption and reaction of borazine, a well-established *h*-BN precursor, on Rh(111), aiming for a better understanding regarding the formation of the *h*-BN/Rh(111) nanomesh from the precursor borazine. At low temperatures (130 K), borazine adsorbed on Rh(111) mainly as an intact molecule, as we deduced from its spectral fingerprint in the B 1s and N 1s XP spectra. To learn about its adsorption geometry, NEXAFS measurements were employed, suggesting that borazine adsorbed flat-lying, i.e., the plane of the six-membered ring is oriented parallel to the Rh(111) surface. In addition, analysis of the Rh 3d spectra revealed a pronounced interaction between borazine and the rhodium surface, indicated by the adsorbate-induced surface core level shift. After the investigation of the adsorption process, TPXPS in the B 1s core level was utilized to follow the thermally induced reaction of borazine on Rh(111) between 130 and 1100 K *in situ*. First, already below 200 K, borazine multilayers desorbed. Thereupon, molecular borazine and several borazine fragments were left on the surface. Exceeding room temperature, dehydrogenation of borazine and its fragments took place. Also, formation of disordered boron nitride set in, which became the dominant species above 500 K. Starting at approximately 650 K, we observed the evolution of the *h*-BN nanomesh. Except for small amounts of boron residues, borazine was fully converted to *h*-BN at 1100 K, which was confirmed by comparison to *h*-BN/Rh(111) prepared according to an established growth protocol.

[P3] (see Chapter 4.3) combined XPS, LEED and DFT in a comprehensive study on the adsorption and thermal stability of elemental bromine on Rh(111), which shows the synergy of these methods in the surface science approach. The adsorption was followed at 170 K *in situ* in the Br 3d core level. At low coverages, only one bromine species appeared, which was, according to LEED and DFT, assigned to atomic bromine adsorbed on fcc hollow surface sites (binding to three rhodium atoms). Upon increasing the surface

coverage, a second, compression-induced bromine species, associated with bridge-bound atomic bromine (binding to two rhodium atoms), evolved. Additionally, a coverage-dependent shift of the initial species to lower binding energies in the Br 3d spectrum indicated strong adsorbate-adsorbate interaction. In the TPXPS experiment, we found bromine on Rh(111) to be thermally very stable (up to 1000 K), which suggested strong covalent bonding. LEED was used to determine the long-range order of the bromine overlayer, which we found to be coverage-dependent: For coverages up to 0.33 ML, a $(\sqrt{3} \times \sqrt{3})R30^\circ$ superstructure was observed while, for higher coverages from 0.33 to 0.43 ML (= saturation coverage), more complex, star-shaped compression structures arose. For each observed LEED pattern, the real-space unit cell and corresponding surface coverage could be derived from XPS and LEED. Based on this, it was possible to visualize the real-space structures for different bromine coverages on Rh(111) by DFT calculations, which illustrate the compression-induced shift of atomic bromine from fcc hollow to bridge sites upon an increasing surface coverage.

[P4] (see Chapter 5) addressed the reactivity of Rh(111)-supported *h*-BN and graphene towards elemental bromine. High-resolution XPS and TPXPS allowed for the *in situ* investigation of these systems, yielding a detailed insight on the molecular level. The distinct chemical modification of 2DMs paves the way for rational tailoring of their unique properties, which is crucial to access the full potential of 2DMs in future. For low-coverage bromine adsorption on the *h*-BN/Rh(111) nanomesh at 170 K, we found selective functionalization of the pores with molecular bromine, confirming the template effect of the nanomesh. Immediately upon annealing, an on-surface reaction of molecular bromine to form polybromides was observed. The latter decomposed at about 240 K to bromide, which remained stable on the surface until its desorption at ~ 640 K. Taking this high thermal stability into consideration, we suggested bromide to bind covalently to the pores of the nanomesh. Notably, the desorption temperature of bromide decreased for high pore coverages, indicating a diffusion-limited desorption mechanism at low coverages. Also, TPXPS proved bromine functionalization of *h*-BN/Rh(111) to be fully reversible. In the case of graphene/Rh(111), bromine adsorption at 170 K did not proceed

in a spatially selective manner. Annealing, moreover, revealed a rather low thermal stability of bromine adsorbed on the graphene/Rh(111) moiré (physisorption). To support and better understand the experimental findings, a DFT- and MD-based theoretical study was performed. The DFT-optimized structures of Rh(111)-supported graphene and *h*-BN showed a stronger buckling for the *h*-BN nanomesh than for the graphene moiré, that is, the pores and wires of *h*-BN strongly differ regarding their reactivity. In addition, adsorption energies for molecular and atomic bromine on the 2DMs were calculated. For the *h*-BN nanomesh, only adsorption in the pores was found to be energetically feasible, with the boron atoms being the preferential adsorption sites for bromine. The stronger corrugation of the nanomesh and the beneficial interaction of bromine with boron might serve as an explanation for the experimentally observed selectivity regarding bromine functionalization of *h*-BN/Rh(111). In a novel approach, MD using a machine-learning force field was used to simulate bromine adsorption on the *h*-BN nanomesh, also confirming its pore selectivity.

Future work will focus on the synthesis, characterization and chemical modification of 2DMs beyond graphene and *h*-BN. As a first step, our group aims at developing reliable strategies for the preparation of transition metal-supported phosphorene and borophene under UHV conditions by means of CVD and/or physical vapor deposition (PVD). To be more precise, we plan to grow phosphorene on Au(111) from an elemental phosphorus source. Borophene, on the other hand, might be prepared from borazine or elemental boron on an Ir(111) substrate. For these studies, we will use an UHV apparatus capable of ARPES, XPS, UPS and LEED (see Chapter 3.3).

7 Zusammenfassung und Ausblick

Die vorliegende kumulative Dissertation befasst sich mit grundlegenden oberflächenwissenschaftlichen Studien der Adsorption und Reaktion von kleinen Molekülen auf der Rh(111)-Einkristalloberfläche und auf Rh(111) gewachsenen zweidimensionalen (2D) Materialien. Experimentelle und theoretische Methoden wurden kombiniert, um einen umfassenden Einblick in diese Systeme auf der molekularen Ebene zu erhalten, d.h. um einzelne Oberflächenspezies, Adsorptionsgeometrien, Adsorptionsplätze, die langreichweitige strukturelle Ordnung, thermisch induzierte Reaktionswege und thermische Stabilitäten aufzuklären. Diesbezügliche Erkenntnisse sind hilfreich für die Untersuchung komplexerer Systeme und, um schließlich reale industrielle Prozesse zu verstehen und zu verbessern. Im Rahmen dieser Arbeit wurde als experimentelle Methode hauptsächlich hochaufgelöste *in situ* Röntgenphotoelektronenspektroskopie (XPS) unter Verwendung von Synchrotronstrahlung angewandt. Abhängig vom untersuchten System wurden die XPS-Experimente durch Röntgen-Nahkanten-Absorptionsspektroskopie (NEXAFS), Beugung langsamer Elektronen (LEED) und/oder theoretische Berechnungen ergänzt. Die Dissertation umfasst vier Publikationen (siehe Anhang A):

[P1] (siehe Kapitel 4.1) behandelte die Adsorption und thermisch induzierte Reaktion von Ethylen (C_2H_4) auf Rh(111), welche mittels XPS- und TPXPS-Messungen *in situ* untersucht wurden. Auf Metalloberflächen adsorbierte kleine Kohlenwasserstoffe wie zum Beispiel Ethylen sind aufschlussreiche Referenzsysteme für die heterogene Katalyse und zugleich leicht verfügbare Ausgangsmoleküle für die Präparation von Graphen. Bei 140 K adsorbierte Ethylen molekular mit der Molekülachse parallel zur Oberfläche auf identischen Adsorptionsplätzen, was aus dem nach der Adsorption aufgenommenen C 1s-XP-Spektrum abgeleitet wurde. Im TPXPS-Experiment wurde das auf der Rh(111)-Oberfläche adsorbierte Ethylen auf 550 K geheizt, wobei kontinuierlich C 1s-XP-Spektren gemessen wurden. Intermediate, die im Verlauf der thermisch induzierten Reaktion auftraten, wurden unter Bezugnahme auf die Schwingungsfeinstruktur ihrer XPS-Signale identifiziert. Beim Erhitzen blieb Ethylen bis ca. 200 K stabil. Bei dieser

Temperatur entwickelte sich eine neue Spezies, welche wir Ethylidin (CCH_3) in einer aufrechtstehenden Adsorptionsgeometrie zuordneten. Beginnend bei 350 K zerfiel Ethylidin unter Bildung von Methylidin und Carbiden. Ab 460 K befanden sich nur noch Carbide auf der Oberfläche. Der früh auftretende Zerfall zu Carbiden stellt eine große Herausforderung dar, da Verkokung die katalytische Rh(111)-Oberfläche deaktiviert, was eine praktische Anwendung Rhodium-basierter Katalysatoren stark erschwert. Auch beim CVD-Wachstum von Graphen ausgehend von Ethylen treten Carbide oft als ungewollte Nebenprodukte auf, wodurch die Qualität der 2D-Schicht vermindert wird.

In [P2] (siehe Kapitel 4.2) untersuchten wir die Adsorption und Reaktion von Borazin, einem häufig verwendeten Ausgangsmolekül für die Synthese von *h*-BN auf Rh(111), mit dem Ziel ein besseres Verständnis bezüglich der Entstehung des *h*-BN/Rh(111)-Nanomesh ausgehend von Borazin zu erhalten. Bei niedrigen Temperaturen (130 K) adsorbierte Borazin vorwiegend als intaktes Molekül auf Rh(111), was wir von seinem spektralen Fingerabdruck in den B 1s- und N 1s-XP-Spektren ableiten konnten. Um seine Adsorptionsgeometrie aufzuklären, wurden NEXAFS-Messungen durchgeführt, welche zeigten, dass Borazin flach auf der Rh(111)-Oberfläche adsorbierte. Darüber hinaus zeigte eine Analyse der Rh 3d-XP-Spektren, dass Borazin stark mit der Rhodium-Oberfläche wechselwirkte, da ein ausgeprägter Adsorbat-induzierter Peak beobachtet wurde. Nach der umfassenden Untersuchung des Adsorptionsprozesses, wurde die thermisch induzierte Reaktion von Borazin auf Rh(111) zwischen 130 und 1100 K mittels TPXPS im B 1s-Bereich *in situ* verfolgt. In Multilag adsorbiertes Borazin desorbierte bereits unter 200 K. Daraufhin blieben molekulares Borazin und einige Borazin-Fragmente auf der Oberfläche zurück. Oberhalb von Raumtemperatur kam es zu Dehydrierung von Borazin und seinen Fragmenten. Zudem setzte die Bildung von ungeordnetem Bornitrid ein, welches bei Temperaturen über 500 K zur dominierenden Spezies wurde. Beginnend bei ~ 650 K beobachteten wir die Entstehung des *h*-BN-Nanomesh. Bei 1100 K war Borazin vollständig zu *h*-BN umgesetzt worden mit Ausnahme geringer Mengen an Bor. Dies wurde durch den Vergleich mit *h*-BN/Rh(111), das gemäß eines etablierten Syntheseweges hergestellt wurde, bestätigt.

[P3] (siehe Kapitel 4.3) kombinierte XPS, LEED und DFT-Berechnungen für eine ausführliche Untersuchung der Adsorption und thermischen Stabilität von elementarem Brom auf Rh(111), was die Synergie dieser Methoden hinsichtlich dieser Art von Untersuchungen unterstrich. Die Adsorption wurde bei 170 K *in situ* im Br 3d-Bereich verfolgt. Bei niedrigen Bedeckungen, erschien nur eine Brom-Spezies, welche unter Berücksichtigung der LEED- und DFT-Ergebnisse Bromatomen zugeordnet wurde, die „fcc hollow“-Adsorptionsplätze (Bindung zu drei Rhodium-Atomen) besetzten. Eine zunehmende Oberflächen-Bedeckung führte aufgrund von Kompression zu einer zweiten Brom-Spezies, welche Bromatomen auf „bridge“-Adsorptionsplätzen (Bindung zu zwei Rhodium-Atomen) zugeschrieben wurde. Zusätzlich wurde ein bedeckungsabhängiger Verschiebung der ersten Brom-Spezies zu niedrigeren Bindungsenergien im Br 3d-Spektrum beobachtet, was auf starke Adsorbat-Adsorbat-Wechselwirkungen hindeutete. Im TPXPS-Experiment stellten wir fest, dass Brom auf Rh(111) thermisch sehr stabil ist (bis zu 1000 K). Daraus wurde geschlossen, dass Brom kovalent zur Rh(111)-Oberfläche bindet. LEED wurde verwendet, um die langreichweitige Ordnung der adsorbierten Brom-Schicht zu bestimmen, wobei diese abhängig von der jeweiligen Oberflächenbedeckung war: Für Bedeckungen bis zu 0.33 ML wurde eine $(\sqrt{3} \times \sqrt{3})R30^\circ$ -Überstruktur gefunden, während sich für höhere Bedeckungen von 0.33 bis 0.43 ML (= Sättigungsbedeckung) komplexere, sternförmige Kompressions-Strukturen herausbildeten. Für jedes beobachtete LEED-Muster konnten mittels XPS und LEED die Realraum-Einheitszellen und die zugehörigen Oberflächenbedeckungen bestimmt werden. Darauf basierende DFT-Berechnungen führten zu den Realraum-Strukturen für verschiedene Brom-Bedeckungen auf Rh(111), welche die bei steigender Bedeckung auftretende kompressionsbedingte Verdrängung der Brom-Atome von „fcc hollow“- zu „bridge“-Adsorptionsplätzen veranschaulichte.

[P4] (siehe Kapitel 5) befasste sich mit der Reaktivität von *h*-BN und Graphen auf Rh(111) gegenüber elementarem Brom. Hochaufgelöste XPS- und TPXPS-Messungen ermöglichten die *in situ*-Untersuchung dieser Systeme und damit einen detaillierten Einblick auf molekularer Ebene. Die gezielte chemische Modifikation von 2D-Materialien

ermöglicht die rationale Anpassung ihrer einzigartigen Eigenschaften, wodurch künftig das volle Potential von 2D-Materialien ausgeschöpft werden könnte. Die Adsorption von niedrigen Brom-Bedeckungen auf dem *h*-BN/Rh(111)-Nanomesh bei 170 K führte zu selektiver Funktionalisierung der Poren mit molekularem Brom, wodurch der erwartete „Template-Effekt“ des Nanomesh bestätigt wurde. Im Rahmen des TPXPS-Experiments wurde das Brom-funktionalisierte *h*-BN bis 800 K geheizt. Unmittelbar zu Beginn reagierte molekulares Brom unter der Entstehung von Polybromiden. Letztere zerfielen bei ungefähr 240 K zu Bromid, welches bis zu seiner Desorption bei ca. 640 K auf der Oberfläche stabil blieb. Diese hohe thermische Stabilität unterstützte die Annahme, dass das Bromid kovalent zu den Poren des Nanomesh bindet. Interessanterweise nahm die Desorptionstemperatur bei steigender Bedeckung in den Poren ab, was auf einen diffusionslimitierten Desorptionsmechanismus bei niedrigen Bedeckungen hinwies. TPXPS zeigte auch, dass die Brom-Funktionalisierung von *h*-BN/Rh(111) vollständig reversibel ist. Im Falle von Graphen auf Rh(111) verlief die Brom-Adsorption bei 170 K nicht räumlich selektiv. Zudem offenbarten TPXPS-Experimente eine niedrigere thermische Stabilität von auf Graphen/Rh(111) adsorbiertem Brom (Physisorption). Als Ergänzung zu den experimentellen Ergebnissen und, um weitere Einblicke zu erhalten, wurde eine auf DFT und MD basierende theoretische Studie ausgeführt. Die DFT-optimierten Strukturen von Graphen und *h*-BN auf Rh(111) zeigten eine deutlichere Wellung für *h*-BN als für Graphen, d.h. die tiefer und höher liegenden Regionen des Nanomesh unterscheiden sich vermutlich stark hinsichtlich ihrer Reaktivität. Des Weiteren wurden Adsorptionsenergien für molekulares und atomares Brom auf den 2D-Materialien berechnet. Im Falle des *h*-BN-Nanomesh war nur die Adsorption in den Poren energetisch möglich, wobei sich die Boratome als die bevorzugten Adsorptionsplätze für Brom herausstellten. Die stärkere Wellung und die vorteilhafte Wechselwirkung von Brom mit Bor könnten die experimentell beobachtete Selektivität der Brom-Funktionalisierung von *h*-BN/Rh(111) erklären. In einem neuartigen Ansatz, wurde MD unter Verwendung eines „machine-learning force field“ genutzt, um die

Adsorption von Brom auf dem *h*-BN-Nanomesh zu simulieren, was ebenfalls die Poren-Selektivität bestätigte.

Die zukünftige Forschung unsere Arbeitsgruppe wird sich auf die Synthese, Charakterisierung und chemische Modifizierung von 2D-Materialien jenseits von Graphen und *h*-BN konzentrieren. Dafür zielen wir zunächst darauf ab, zuverlässige Strategien für die Präparation von Phosphoren und Borophen auf Übergangsmetall-Oberflächen unter UHV-Bedingungen mittels CVD und/oder PVD zu entwickeln. Genauer gesagt planen wir Phosphoren-Wachstum ausgehend von einer elementaren Phosphor-Quelle auf Au(111). Borophen dagegen könnte ausgehend von Borazin oder elementarem Bor auf einem Ir(111)-Substrat synthetisiert werden. Für diese Untersuchungen werden wir eine UHV-Apparatur verwenden, die über winkelaufgelöste Photoelektronenspektroskopie (ARPES), XPS, Ultraviolettphotoelektronenspektroskopie (UPS) und LEED verfügt (siehe Kapitel 3.3).

8 Bibliography

- [1] G. A. Somorjai, Modern Concepts in Surface Science and Heterogeneous Catalysis, *J. Phys. Chem.* **1990**, 94, 1013-1023.
- [2] G. A. Somorjai, Modern Surface Science and Surface Technologies: An Introduction, *Chem. Rev.* **1996**, 96, 1223-1236.
- [3] K. W. Kolasinski, *Surface Science: Foundations of Catalysis and Nanoscience*, John Wiley & Sons Ltd, Chichester, 2008.
- [4] P. Woodruff, *Modern Techniques of Surface Science*, Cambridge University Press, Cambridge, 2016.
- [5] H. P. Bonzel, The Role of Surface Science Experiments in Understanding Heterogeneous Catalysis, *Surf. Sci.* **1977**, 68, 236-258.
- [6] G. A. Somorjai, Catalysis and Surface Science, *Surf. Sci.* **1979**, 89, 496-524.
- [7] D. W. Goodman, Single Crystals as Model Catalysts, *J. Vac. Sci. Technol.* **1982**, 20, 522-526.
- [8] G. A. Somorjai, Surface Science and Catalysis, *Science* **1985**, 227, 902-908.
- [9] G. A. Somorjai, The Surface Science of Heterogeneous Catalysis, *Surf. Sci.* **1994**, 299-300, 849-866.
- [10] V. P. Zhdanov, Impact of Surface Science on the Understanding of Kinetics of Heterogeneous Catalytic Reactions, *Surf. Sci.* **2002**, 500, 966-985.
- [11] G. Rupprechter, *Surface Science Approach to Heterogeneous Catalysis*, in *Surface and Interface Science: Solid-Gas Interfaces I*, edited by K. Wandelt (WILEY-VCH, Weinheim, 2015), pp. 459-528.
- [12] M. P. Soriaga, Ultra-High Vacuum Techniques in the Study of Single-Crystal Electrode Surfaces, *Prog. Surf. Sci.* **1992**, 39, 325-443.
- [13] D. M. Kolb, Electrochemical Surface Science, *Angew. Chem., Int. Ed.* **2001**, 40, 1162-1181.
- [14] D. M. Kolb, An Atomistic View of Electrochemistry, *Surf. Sci.* **2002**, 500, 722-740.
- [15] C. Papp, P. Wasserscheid, J. Libuda and H.-P. Steinrück, Liquid Organic Hydrogen Carriers: Surface Science Studies of Carbazole Derivatives, *Chem. Rec.* **2014**, 14, 879-896.
- [16] P. Preuster, C. Papp and P. Wasserscheid, Liquid Organic Hydrogen Carriers (LOHCs): Toward a Hydrogen-Free Hydrogen Economy, *Acc. Chem. Res.* **2017**, 50, 74-85.
- [17] E. Pomerantseva, F. Bonaccorso, X. Feng, Y. Cui and Y. Gogotsi, Energy Storage: The Future Enabled by Nanomaterials, *Science* **2019**, 366, eaan8285.
- [18] F. Hemauer, H.-P. Steinrück and C. Papp, The Norbornadiene/Quadricyclane Pair as Molecular Solar Thermal Energy Storage System: Surface Science Investigations, *ChemPhysChem* **2024**, e202300806.
- [19] M. Bieri *et al.*, Porous Graphenes: Two-Dimensional Polymer Synthesis with Atomic Precision, *Chem. Commun.* **2009**, 6919-6921.
- [20] J. Cai *et al.*, Atomically Precise Bottom-Up Fabrication of Graphene Nanoribbons, *Nature* **2010**, 466, 470-473.
- [21] J. R. Sanchez-Valencia, T. Dienel, O. Gröning, I. Shorubalko, A. Mueller, M. Jansen, K. Amsharov, P. Ruffieux and R. Fasel, Controlled Synthesis of Single-Chirality Carbon Nanotubes, *Nature* **2014**, 512, 61-64.
- [22] L. Dong, P. N. Liu and N. Lin, Surface-Activated Coupling Reactions Confined on a Surface, *Acc. Chem. Res.* **2015**, 48, 2765-2774.
- [23] Q. Fan, J. M. Gottfried and J. Zhu, Surface-Catalyzed C-C Covalent Coupling Strategies Toward the Synthesis of Low-Dimensional Carbon-Based Nanostructures, *Acc. Chem. Res.* **2015**, 48, 2484-2494.

- [24] C. Steiner, J. Gebhardt, M. Ammon, Z. Yang, A. Heidenreich, N. Hammer, A. Göring, M. Kivala and S. Maier, Hierarchical On-Surface Synthesis and Electronic Structure of Carbonyl-Functionalized One- and Two-Dimensional Covalent Nanoarchitectures, *Nat. Commun.* **2017**, 8, 14765.
- [25] M. Ammon, T. Sander and S. Maier, On-Surface Synthesis of Porous Carbon Nanoribbons from Polymer Chains, *J. Am. Chem. Soc.* **2017**, 139, 12976-12984.
- [26] Z. Cai, B. Liu, X. Zou and H.-M. Cheng, Chemical Vapor Deposition Growth and Applications of Two-Dimensional Materials and Their Heterostructures, *Chem. Rev.* **2018**, 118, 6091-6133.
- [27] P. Forzatti and L. Lietti, Catalyst Deactivation, *Catal. Today* **1999**, 52, 165-181.
- [28] T. Fuhrmann, M. Kinne, B. Tränkenschuh, C. Papp, J. F. Zhu, R. Denecke and H.-P. Steinrück, Activated Adsorption of Methane on Pt(1 1 1) - An In Situ XPS Study, *New J. Phys.* **2005**, 7, 107.
- [29] R. Streber, C. Papp, M. P. A. Lorenz, O. Höfert, E. Darlatt, A. Bayer, R. Denecke and H.-P. Steinrück, SO₂ Adsorption and Thermal Evolution on Clean and Oxygen Precovered Pt(111), *Chem. Phys. Lett.* **2010**, 494, 188-192.
- [30] E. M. Freiburger, F. Düll, C. Wichmann, U. Bauer, H.-P. Steinrück and C. Papp, A High-Resolution X-Ray Photoelectron Spectroscopy Study on the Adsorption and Reaction of Ethylene on Rh(111), *Chem. Phys. Lett.* **2022**, 797, 139595.
- [31] C. Gleichweit *et al.*, Dehydrogenation of Dodecahydro-N-ethylcarbazole on Pt(111), *ChemSusChem* **2013**, 6, 974-977.
- [32] C. Gleichweit *et al.*, Surface Reactions of Dicyclohexylmethane on Pt(111), *J. Phys. Chem. C* **2015**, 119, 20299-20311.
- [33] P. Bachmann *et al.*, Dehydrogenation of the Liquid Organic Hydrogen Carrier System Indole/Indoline/Octahydroindole on Pt(111), *J. Phys. Chem. C* **2018**, 122, 4470-4479.
- [34] J. Steinhauer, P. Bachmann, U. Bauer, F. Düll, H.-P. Steinrück and C. Papp, Model Catalytic Studies of the LOHC System 2,2'-Bipiperidine/2,2'-Bipyridine on Ni(111), *J. Phys. Chem. C* **2021**, 125, 8216-8223.
- [35] V. Schwaab, F. Hemauer, E. M. Freiburger, N. J. Waleska-Wellnhofer, H.-P. Steinrück and C. Papp, Liquid Organic Hydrogen Carriers: Model Catalytic Studies on the Thermal Dehydrogenation of 1-Cyclohexylethanol on Pt(111), *J. Phys. Chem. C* **2023**, 127, 11058-11066.
- [36] U. Bauer *et al.*, Surface Chemistry of 2,3-Dibromosubstituted Norbornadiene/Quadricyclane as Molecular Solar Thermal Energy Storage System on Ni(111), *J. Chem. Phys.* **2019**, 150, 184706.
- [37] F. Hemauer *et al.*, Surface Chemistry of the Molecular Solar Thermal Energy Storage System 2,3-Dicyano-Norbornadiene/Quadricyclane on Ni(111), *ChemPhysChem* **2022**, 23, e202200199.
- [38] C. Papp, From Flat Surfaces to Nanoparticles: In Situ Studies of the Reactivity of Model Catalysts, *Catal. Lett.* **2017**, 147, 2-19.
- [39] A. B. Preobrajenski, A. S. Vinogradov, M. L. Ng, E. Čavar, R. Westerström, A. Mikkelsen, E. Lundgren and N. Mårtensson, Influence of Chemical Interaction at the Lattice-Mismatched *h*-BN/Rh(111) and *h*-BN/Pt(111) Interfaces on the Overlayer Morphology, *Phys. Rev. B* **2007**, 75, 245412.
- [40] P. Sutter, J. T. Sadowski and E. Sutter, Graphene on Pt(111): Growth and Substrate Interaction, *Phys. Rev. B* **2009**, 80, 245411.

- [41] W. Zhao, S. M. Kozlov, O. Höfert, K. Gotterbarm, M. P. A. Lorenz, F. Viñes, C. Papp, A. Görling and H.-P. Steinrück, Graphene on Ni(111): Coexistence of Different Surface Structures, *J. Phys. Chem. Lett.* **2011**, 2, 759-764.
- [42] P. Bachmann, F. Düll, F. Späth, U. Bauer, H.-P. Steinrück and C. Papp, A HR-XPS Study of the Formation of h-BN on Ni(111) from the Two Precursors, Ammonia Borane and Borazine, *J. Chem. Phys.* **2018**, 149, 164709.
- [43] S.-Y. Kwon, C. V. Ciobanu, V. Petrova, V. B. Shenoy, J. Bareño, V. Gambin, I. Petrov and S. Kodambaka, Growth of Semiconducting Graphene on Palladium, *Nano Lett.* **2009**, 9, 3985-3990.
- [44] P. Arias, A. Ebnoussair, C. V. Ciobanu and S. Kodambaka, Growth Kinetics of Two-Dimensional Hexagonal Boron Nitride Layers on Pd(111), *Nano Lett.* **2020**, 20, 2886-2891.
- [45] M. Corso, W. Auwärter, M. Muntwiler, A. Tamai, T. Greber and J. Osterwalder, Boron Nitride Nanomesh, *Science* **2004**, 303, 217-220.
- [46] K. Gotterbarm, W. Zhao, O. Höfert, C. Gleichweit, C. Papp and H.-P. Steinrück, Growth and Oxidation of Graphene on Rh(111), *Phys. Chem. Chem. Phys.* **2013**, 15, 19625-19631.
- [47] A. T. N'Diaye, J. Coraux, T. N. Plasa, C. Busse and T. Michely, Structure of Epitaxial Graphene on Ir(111), *New J. Phys.* **2008**, 10, 043033.
- [48] F. Orlando, R. Larciprete, P. Lacovig, I. Boscarato, A. Baraldi and S. Lizzit, Epitaxial Growth of Hexagonal Boron Nitride on Ir(111), *J. Phys. Chem. C* **2012**, 116, 157-164.
- [49] A. Goriachko, Y. He, M. Knapp, H. Over, M. Corso, T. Brugger, S. Berner, J. Osterwalder and T. Greber, Self-Assembly of a Hexagonal Boron Nitride Nanomesh on Ru(0001), *Langmuir* **2007**, 23, 2928-2931.
- [50] D. Martocchia *et al.*, Graphene on Ru(0001): A 25 x 25 Supercell, *Phys. Rev. Lett.* **2008**, 101, 126102.
- [51] T. Brugger, S. Günther, B. Wang, J. H. Dil, M.-L. Bocquet, J. Osterwalder, J. Winterlin and T. Greber, Comparison of Electronic Structure and Template Function of Single-Layer Graphene and a Hexagonal Boron Nitride Nanomesh on Ru(0001), *Phys. Rev. B* **2009**, 79, 045407.
- [52] L. Gao, J. R. Guest and N. P. Guisinger, Epitaxial Graphene on Cu(111), *Nano Lett.* **2010**, 10, 3512-3516.
- [53] S. Joshi *et al.*, Boron Nitride on Cu(111): An Electronically Corrugated Monolayer, *Nano Lett.* **2012**, 12, 5821-5828.
- [54] E. M. Freiburger, F. Düll, P. Bachmann, J. Steinhauer, F. J. Williams, H.-P. Steinrück and C. Papp, h-BN in the Making: The Surface Chemistry of Borazine on Rh(111), *J. Chem. Phys.* **2024**, 160, 154706.
- [55] J. Björk, F. Hanke and S. Stafström, Mechanisms of Halogen-Based Covalent Self-Assembly on Metal Surfaces, *J. Am. Chem. Soc.* **2013**, 135, 5768-5775.
- [56] D. Peyrot and F. Silly, On-Surface Synthesis of Two-Dimensional Covalent Organic Structures versus Halogen-Bonded Self-Assembly: Competing Formation of Organic Nanoarchitectures, *ACS Nano* **2016**, 10, 5490-5498.
- [57] Q. Sun, R. Zhang, J. Qiu, R. Liu and W. Xu, On-Surface Synthesis of Carbon Nanostructures, *Adv. Mater.* **2018**, 30, 1705630.
- [58] S. Clair and D. G. de Oteyza, Controlling a Chemical Coupling Reaction on a Surface: Tools and Strategies for On-Surface Synthesis, *Chem. Rev.* **2019**, 119, 4717-4776.
- [59] N. J. Tao and S. M. Lindsay, In Situ Scanning Tunneling Microscopy Study of Iodine and Bromine Adsorption on Gold(111) under Potential Control, *J. Phys. Chem.* **1992**, 96, 5213-5217.

- [60] O. M. Magnussen, B. M. Ocko, J. X. Wang and R. R. Adzic, In-Situ X-Ray Diffraction and STM Studies of Bromide Adsorption on Au(111) Electrodes, *J. Phys. Chem.* **1996**, 100, 5500-5508.
- [61] T. Yamada, K. Ogaki, S. Okubo and K. Itaya, Continuous Variation of Iodine Adlattices on Ag(111) Electrodes: In Situ STM and Ex Situ LEED Studies, *Surf. Sci.* **1996**, 369, 321-335.
- [62] O. Endo, D. Matsumura, K. Kohdate, M. Kiguchi, T. Yokoyama and T. Ohta, In-Situ XAFS Studies of Br Adsorption on the Silver(111) Electrode, *J. Electroanal. Chem.* **2000**, 494, 121-126.
- [63] I. T. McCrum, S. A. Akhade and M. J. Janik, Electrochemical Specific Adsorption of Halides on Cu 111, 100, and 211: A Density Functional Theory Study, *Electrochim. Acta* **2015**, 173, 302-309.
- [64] Q. Zhu and S.-q. Wang, Trends and Regularities for Halogen Adsorption on Various Metal Surfaces, *J. Electrochem. Soc.* **2016**, 163, H796.
- [65] C. T. Campbell, Chlorine Promoters in Selective Ethylene Epoxidation over Ag(111): A Comparison with Ag(110), *J. Catal.* **1986**, 99, 28-38.
- [66] B. Shen, Z. Fang, K. Fan and J. Deng, Effect of Halogen Atoms (Cl, Br, I) on the Structure and Catalytic Behavior of Ag(111) Surface: A Density Functional Theory Study, *Surf. Sci.* **2000**, 459, 206-212.
- [67] R. M. Lambert, R. L. Cropley, A. Husain and M. S. Tikhov, Halogen-Induced Selectivity in Heterogeneous Epoxidation is an Electronic Effect - Fluorine, Chlorine, Bromine and Iodine in the Ag-Catalysed Selective Oxidation of Ethene, *Chem. Commun.* **2003**, 1184-1185.
- [68] D. Torres, F. Illas and R. M. Lambert, Towards an Understanding of Promoter Action in Heterogeneously Catalyzed Ethene Epoxidation: Why Chlorine is the Best Halogen, *J. Catal.* **2008**, 260, 380-383.
- [69] E. Bertel, K. Schwaha and F. P. Netzer, The Adsorption of Bromine on Pt(111): Observation of an Irreversible Order-Disorder Transition, *Surf. Sci.* **1979**, 83, 439-452.
- [70] W. T. Tysse and R. M. Lambert, Surface Chemistry of the Metal-Halogen Interface: Bromine Chemisorption and Dibromide Formation on Palladium (111), *Surf. Sci.* **1982**, 115, 37-47.
- [71] R. G. Jones and M. Kadodwala, Bromine Adsorption on Cu(111), *Surf. Sci.* **1997**, 370, L219-L225.
- [72] T. W. Fishlock, J. B. Pethica, A. Oral, R. G. Egdell and F. H. Jones, Interaction of Bromine with Ni(110) Studied by Scanning Tunnelling Microscopy, *Surf. Sci.* **1999**, 426, 212-224.
- [73] A. Seliverstov, D. Muzychenko, A. Volodin, E. Janssens and C. V. Haesendonck, Atomic Structure and Peculiarities of the Electronic Properties of Br Layers on Ag(111) at Different Coverages, *Surf. Sci.* **2023**, 734, 122304.
- [74] E. M. Freiburger, J. Steffen, N. J. Waleska-Wellnhofer, A. Harrer, F. Hemauer, V. Schwaab, A. Görling, H.-P. Steinrück and C. Papp, Bromine Adsorption and Thermal Stability on Rh(111): A Combined XPS, LEED and DFT Study, *ChemPhysChem* **2023**, 24, e202300510.
- [75] K. S. Novoselov, A. K. Geim, S. V. Morozov, D. Jiang, Y. Zhang, S. V. Dubonos, I. V. Grigorieva and A. A. Firsov, Electric Field Effect in Atomically Thin Carbon Films, *Science* **2004**, 306, 666-669.
- [76] K. S. Novoselov, Graphene: Materials in the Flatland (Nobel Lecture), *Angew. Chem. Int. Ed.* **2011**, 50, 6986-7002.
- [77] A. K. Geim and K. S. Novoselov, The Rise of Graphene, *Nature Mater.* **2007**, 6, 183-191.
- [78] K. S. Novoselov *et al.*, Electronic Properties of Graphene, *phys. stat. sol. (b)* **2007**, 244, 4106-4111.

-
- [79] A. A. Balandin, S. Ghosh, W. Bao, I. Calizo, D. Teweldebrhan, F. Miao and C. N. Lau, Superior Thermal Conductivity of Single-Layer Graphene, *Nano Lett.* **2008**, 8, 902-907.
- [80] Y. Zhang, Y.-W. Tan, H. L. Stormer and P. Kim, Experimental Observation of the Quantum Hall Effect and Berry's Phase in Graphene, *Nature* **2005**, 438, 201-204.
- [81] K. S. Novoselov *et al.*, Room-Temperature Quantum Hall Effect in Graphene, *Science* **2007**, 315, 1379-1379.
- [82] J. S. Bunch, S. S. Verbridge, J. S. Alden, A. M. van der Zande, J. M. Parpia, H. G. Craighead and P. L. McEuen, Impermeable Atomic Membranes from Graphene Sheets, *Nano Lett.* **2008**, 8, 2458-2462.
- [83] C. Lee, X. Wei, J. W. Kysar and J. Hone, Measurement of the Elastic Properties and Intrinsic Strength of Monolayer Graphene, *Science* **2008**, 321, 385-388.
- [84] K. S. Kim *et al.*, Large-Scale Pattern Growth of Graphene Films for Stretchable Transparent Electrodes, *Nature* **2009**, 457, 706-710.
- [85] P. Avouris, Graphene: Electronic and Photonic Properties and Devices, *Nano Lett.* **2010**, 10, 4285-4294.
- [86] F. Bonaccorso, Z. Sun, T. Hasan and A. C. Ferrari, Graphene Photonics and Optoelectronics, *Nature Photon.* **2010**, 4, 611-622.
- [87] F. Schwierz, Graphene Transistors, *Nature Nanotech.* **2010**, 5, 487-496.
- [88] Q. Bao and K. P. Loh, Graphene Photonics, Plasmonics, and Broadband Optoelectronic Devices, *ACS Nano* **2012**, 6, 3677-3694.
- [89] F. Schwierz, Graphene Transistors: Status, Prospects, and Problems, *Proc. IEEE* **2013**, 101, 1567-1584.
- [90] Z. Liu, S. P. Lau and F. Yan, Functionalized Graphene and Other Two-Dimensional Materials for Photovoltaic Devices: Device Design and Processing, *Chem. Soc. Rev.* **2015**, 44, 5638-5679.
- [91] M. Romagnoli *et al.*, Graphene-Based Integrated Photonics for Next-Generation Datacom and Telecom, *Nat. Rev. Mater.* **2018**, 3, 392-414.
- [92] S. Navalon, A. Dhakshinamoorthy, M. Alvaro and H. Garcia, Carbocatalysis by Graphene-Based Materials, *Chem. Rev.* **2014**, 114, 6179-6212.
- [93] M. S. Ahmad and Y. Nishina, Graphene-Based Carbocatalysts for Carbon-Carbon Bond Formation, *Nanoscale* **2020**, 12, 12210-12227.
- [94] V. Tozzini and V. Pellegrini, Prospects for Hydrogen Storage in Graphene, *Phys. Chem. Chem. Phys.* **2013**, 15, 80-89.
- [95] J. Zhu, D. Yang, Z. Yin, Q. Yan and H. Zhang, Graphene and Graphene-Based Materials for Energy Storage Applications, *Small* **2014**, 10, 3480-3498.
- [96] R. Raccichini, A. Varzi, S. Passerini and B. Scrosati, The Role of Graphene for Electrochemical Energy Storage, *Nature Mater.* **2015**, 14, 271-279.
- [97] L. Huang, M. Zhang, C. Li and G. Shi, Graphene-Based Membranes for Molecular Separation, *J. Phys. Chem. Lett.* **2015**, 6, 2806-2815.
- [98] G. Liu, W. Jin and N. Xu, Graphene-Based Membranes, *Chem. Soc. Rev.* **2015**, 44, 5016-5030.
- [99] L. Nilsson, M. Andersen, R. Balog, E. Lægsgaard, P. Hofmann, F. Besenbacher, B. Hammer, I. Stensgaard and L. Hornekær, Graphene Coatings: Probing the Limits of the One Atom Thick Protection Layer, *ACS Nano* **2012**, 6, 10258-10266.
- [100] D. Prasai, J. C. Tuberquia, R. R. Harl, G. K. Jennings and K. I. Bolotin, Graphene: Corrosion-Inhibiting Coating, *ACS Nano* **2012**, 6, 1102-1108.
- [101] G. Cui, Z. Bi, R. Zhang, J. Liu, X. Yu and Z. Li, A Comprehensive Review on Graphene-Based Anti-Corrosive Coatings, *Chem. Eng. J.* **2019**, 373, 104-121.

- [102] F. Yavari and N. Koratkar, Graphene-Based Chemical Sensors, *J. Phys. Chem. Lett.* **2012**, 3, 1746-1753.
- [103] O. Moldovan, B. Iñiguez, M. J. Deen and L. F. Marsal, Graphene Electronic Sensors – Review of Recent Developments and Future Challenges, *IET Circuits Devices Syst.* **2015**, 9, 446-453.
- [104] D. Bitounis, H. Ali-Boucetta, B. H. Hong, D.-H. Min and K. Kostarelos, Prospects and Challenges of Graphene in Biomedical Applications, *Adv. Mater.* **2013**, 25, 2258-2268.
- [105] A. Servant, A. Bianco, M. Prato and K. Kostarelos, Graphene for Multi-Functional Synthetic Biology: The last 'Zeitgeist' in Nanomedicine, *Bioorg. Med. Chem. Lett.* **2014**, 24, 1638-1649.
- [106] Graphene Steps into Biomedicine, *Nature Mater.* **2016**, 15, 485-485.
- [107] G. Reina, J. M. González-Domínguez, A. Criado, E. Vázquez, A. Bianco and M. Prato, Promises, Facts and Challenges for Graphene in Biomedical Applications, *Chem. Soc. Rev.* **2017**, 46, 4400-4416.
- [108] B. Lalmi, H. Oughaddou, H. Enriquez, A. Kara, S. Vizzini, B. Ealet and B. Aufray, Epitaxial Growth of a Silicene Sheet, *Appl. Phys. Lett.* **2010**, 97, 223109.
- [109] M. E. Dávila, L. Xian, S. Cahangirov, A. Rubio and G. Le Lay, Germanene: A Novel Two-Dimensional Germanium Allotrope Akin to Graphene and Silicene, *New J. Phys.* **2014**, 16, 095002.
- [110] A. J. Mannix *et al.*, Synthesis of Borophenes: Anisotropic, Two-Dimensional Boron Polymorphs, *Science* **2015**, 350, 1513-1516.
- [111] H. Liu, A. T. Neal, Z. Zhu, Z. Luo, X. Xu, D. Tománek and P. D. Ye, Phosphorene: An Unexplored 2D Semiconductor with a High Hole Mobility, *ACS Nano* **2014**, 8, 4033-4041.
- [112] S. Manzeli, D. Ovchinnikov, D. Pasquier, O. V. Yazyev and A. Kis, 2D Transition Metal Dichalcogenides, *Nat. Rev. Mater.* **2017**, 2, 17033.
- [113] A. Pakdel, Y. Bando and D. Golberg, Nano Boron Nitride Flatland, *Chem. Soc. Rev.* **2014**, 43, 934-959.
- [114] K. Zhang, Y. Feng, F. Wang, Z. Yang and J. Wang, Two Dimensional Hexagonal Boron Nitride (2D-hBN): Synthesis, Properties and Applications, *J. Mater. Chem. C* **2017**, 5, 11992-12022.
- [115] L. Song *et al.*, Large Scale Growth and Characterization of Atomic Hexagonal Boron Nitride Layers, *Nano Lett.* **2010**, 10, 3209-3215.
- [116] A. Falin *et al.*, Mechanical Properties of Atomically Thin Boron Nitride and the Role of Interlayer Interactions, *Nature Commun.* **2017**, 8, 15815.
- [117] K. Watanabe, T. Taniguchi and H. Kanda, Direct-Bandgap Properties and Evidence for Ultraviolet Lasing of Hexagonal Boron Nitride Single Crystal, *Nature Mater.* **2004**, 3, 404-409.
- [118] Z. Liu *et al.*, Ultrathin High-Temperature Oxidation-Resistant Coatings of Hexagonal Boron Nitride, *Nature Commun.* **2013**, 4, 2541.
- [119] L. H. Li, J. Cervenka, K. Watanabe, T. Taniguchi and Y. Chen, Strong Oxidation Resistance of Atomically Thin Boron Nitride Nanosheets, *ACS Nano* **2014**, 8, 1457-1462.
- [120] L. H. Li, T. Xing, Y. Chen and R. Jones, Boron Nitride Nanosheets for Metal Protection, *Adv. Mater. Interfaces* **2014**, 1, 1300132.
- [121] S. Jia *et al.*, CVD Growth of High-Quality and Large-Area Continuous h-BN Thin Films Directly on Stainless-Steel as Protective Coatings, *Mater. Today Nano* **2021**, 16, 100135.

- [122] G. Giovannetti, P. A. Khomyakov, G. Brocks, P. J. Kelly and J. van den Brink, Substrate-Induced Band Gap in Graphene on Hexagonal Boron Nitride: Ab Initio Density Functional Calculations, *Phys. Rev. B* **2007**, 76, 073103.
- [123] C. R. Dean *et al.*, Boron Nitride Substrates for High-Quality Graphene Electronics, *Nature Nanotech.* **2010**, 5, 722-726.
- [124] C. Dean *et al.*, Graphene Based Heterostructures, *Solid State Commun.* **2012**, 152, 1275-1282.
- [125] K. Watanabe and T. Taniguchi, Hexagonal Boron Nitride as a New Ultraviolet Luminescent Material and Its Application, *Int. J. Appl. Ceram. Technol.* **2011**, 8, 977-989.
- [126] K. E. Whitener and P. E. Sheehan, Graphene Synthesis, *Diam. Relat. Mater.* **2014**, 46, 25-34.
- [127] K. S. Novoselov, V. I. Fal'ko, L. Colombo, P. R. Gellert, M. G. Schwab and K. Kim, A Roadmap for Graphene, *Nature* **2012**, 490, 192-200.
- [128] S. Roy *et al.*, Structure, Properties and Applications of Two-Dimensional Hexagonal Boron Nitride, *Adv. Mater.* **2021**, 33, 2101589.
- [129] A. F. Rigosi, A. L. Levy, M. R. Snure and N. R. Glavin, Turn of the Decade: Versatility of 2D Hexagonal Boron Nitride, *J. Phys. Mater.* **2021**, 4, 032003.
- [130] J. Wintterlin and M. L. Bocquet, Graphene on Metal Surfaces, *Surf. Sci.* **2009**, 603, 1841-1852.
- [131] M. Batzill, The Surface Science of Graphene: Metal Interfaces, CVD Synthesis, Nanoribbons, Chemical Modifications, and Defects, *Surf. Sci. Rep.* **2012**, 67, 83-115.
- [132] W. Auwärter, Hexagonal Boron Nitride Monolayers on Metal Supports: Versatile Templates for Atoms, Molecules and Nanostructures, *Surf. Sci. Rep.* **2019**, 74, 1-95.
- [133] A. B. Preobrajenski, M. A. Nesterov, M. L. Ng, A. S. Vinogradov and N. Mårtensson, Monolayer h-BN on Lattice-Mismatched Metal Surfaces: On the Formation of the Nanomesh, *Chem. Phys. Lett.* **2007**, 446, 119-123.
- [134] A. B. Preobrajenski, M. L. Ng, A. S. Vinogradov and N. Mårtensson, Controlling Graphene Corrugation on Lattice-Mismatched Substrates, *Phys. Rev. B* **2008**, 78, 073401.
- [135] B. Wang and M.-L. Bocquet, Monolayer Graphene and h-BN on Metal Substrates as Versatile Templates for Metallic Nanoclusters, *J. Phys. Chem. Lett.* **2011**, 2, 2341-2345.
- [136] M. L. Ng, A. B. Preobrajenski, A. S. Vinogradov and N. Mårtensson, Formation and Temperature Evolution of Au Nanoparticles Supported on the h-BN Nanomesh, *Surf. Sci.* **2008**, 602, 1250-1255.
- [137] Y. Pan, M. Gao, L. Huang, F. Liu and H. J. Gao, Directed Self-Assembly of Monodispersed Platinum Nanoclusters on Graphene Moiré Template, *Appl. Phys. Lett.* **2009**, 95, 093106.
- [138] H. P. Koch, R. Laskowski, P. Blaha and K. Schwarz, Adsorption of Gold Atoms on the h-BN/Rh(111) Nanomesh, *Phys. Rev. B* **2011**, 84, 245410.
- [139] K. Gotterbarm, C. Steiner, C. Bronnbauer, U. Bauer, H.-P. Steinrück, S. Maier and C. Papp, Graphene-Templated Growth of Pd Nanoclusters, *J. Phys. Chem. C* **2014**, 118, 15934-15939.
- [140] F. Düll, V. Schwaab, F. Späth, U. Bauer, P. Bachmann, J. Steinhauer, H.-P. Steinrück and C. Papp, Sulfur Oxidation on Graphene-Supported Platinum Nanocluster Arrays, *Chem. Phys. Lett.* **2018**, 708, 165-169.
- [141] F. Düll *et al.*, Growth and Stability of Pt Nanoclusters from 1 to 50 Atoms on h-BN/Rh(111), *Phys. Chem. Chem. Phys.* **2019**, 21, 21287-21295.
- [142] N. J. Waleska, F. Düll, P. Bachmann, F. Hemauer, J. Steinhauer and C. Papp, Reactivity and Passivation of Fe Nanoclusters on h-BN/Rh(111), *Chem. Eur. J.* **2021**, 27, 17087-17093.
- [143] W. S. Hummers Jr and R. E. Offeman, Preparation of Graphitic Oxide, *J. Am. Chem. Soc.* **1958**, 80, 1339-1339.

- [144] D. C. Marcano, D. V. Kosynkin, J. M. Berlin, A. Sinitskii, Z. Sun, A. Slesarev, L. B. Alemany, W. Lu and J. M. Tour, Improved Synthesis of Graphene Oxide, *ACS Nano* **2010**, 4, 4806-4814.
- [145] C. E. Halbig, O. Martin, F. Hauke, S. Eigler and A. Hirsch, Oxo-Functionalized Graphene: A Versatile Precursor for Alkylated Graphene Sheets by Reductive Functionalization, *Chem. Eur. J.* **2018**, 24, 13348-13354.
- [146] W. Feng, P. Long, Y. Feng and Y. Li, Two-Dimensional Fluorinated Graphene: Synthesis, Structures, Properties and Applications, *Adv. Sci.* **2016**, 3, 1500413.
- [147] T. Wei, S. Al-Fogra, F. Hauke and A. Hirsch, Direct Laser Writing on Graphene with Unprecedented Efficiency of Covalent Two-Dimensional Functionalization, *J. Am. Chem. Soc.* **2020**, 142, 21926-21931.
- [148] T. Wei *et al.*, Molecular Stacking on Graphene, *Angew. Chem. Int. Ed.* **2022**, 61, e202201169.
- [149] J. M. Englert *et al.*, Covalent Bulk Functionalization of Graphene, *Nature Chem.* **2011**, 3, 279-286.
- [150] A. Hirsch, J. M. Englert and F. Hauke, Wet Chemical Functionalization of Graphene, *Acc. Chem. Res.* **2013**, 46, 87-96.
- [151] J. Malig, N. Jux and D. M. Guldi, Toward Multifunctional Wet Chemically Functionalized Graphene - Integration of Oligomeric, Molecular, and Particulate Building Blocks that Reveal Photoactivity and Redox Activity, *Acc. Chem. Res.* **2013**, 46, 53-64.
- [152] S. Eigler and A. Hirsch, Chemistry with Graphene and Graphene Oxide - Challenges for Synthetic Chemists, *Angew. Chem., Int. Ed.* **2014**, 53, 7720-7738.
- [153] G. Bottari *et al.*, Chemical Functionalization and Characterization of Graphene-Based Materials, *Chem. Soc. Rev.* **2017**, 46, 4464-4500.
- [154] Z. Zheng, M. Cox and B. Li, Surface Modification of Hexagonal Boron Nitride Nanomaterials: A Review, *J. Mater. Sci.* **2018**, 53, 66-99.
- [155] R. J. Koch *et al.*, Growth and Electronic Structure of Nitrogen-Doped Graphene on Ni(111), *Phys. Rev. B* **2012**, 86, 075401.
- [156] W. Zhao, O. Höfert, K. Gotterbarm, J. F. Zhu, C. Papp and H.-P. Steinrück, Production of Nitrogen-doped Graphene by Low-Energy Nitrogen Implantation, *J. Phys. Chem. C* **2012**, 116, 5062-5066.
- [157] J. Gebhardt *et al.*, Growth and Electronic Structure of Boron-Doped Graphene, *Phys. Rev. B* **2013**, 87, 155437.
- [158] D. Usachov, V. K. Adamchuk, D. Haberer, A. Grüneis, H. Sachdev, A. B. Preobrajenski, C. Laubschat and D. V. Vyalikh, Quasifreestanding Single-Layer Hexagonal Boron Nitride as a Substrate for Graphene Synthesis, *Phys. Rev. B* **2010**, 82, 075415.
- [159] T. Brugger, H. Ma, M. Iannuzzi, S. Berner, A. Winkler, J. Hutter, J. Osterwalder and T. Greber, Nanotexture Switching of Single-Layer Hexagonal Boron Nitride on Rhodium by Intercalation of Hydrogen Atoms, *Angew. Chem. Int. Ed.* **2010**, 49, 6120-6124.
- [160] R. Balog *et al.*, Bandgap Opening in Graphene Induced by Patterned Hydrogen Adsorption, *Nature Mater.* **2010**, 9, 315-319.
- [161] W. Zhao, J. Gebhardt, F. Späth, K. Gotterbarm, C. Gleichweit, H.-P. Steinrück, A. Görling and C. Papp, Reversible Hydrogenation of Graphene on Ni(111) - Synthesis of "Graphone", *Chem. Eur. J.* **2015**, 21, 3347-3358.
- [162] F. Späth, J. Gebhardt, F. Düll, U. Bauer, P. Bachmann, C. Gleichweit, A. Görling, H.-P. Steinrück and C. Papp, Hydrogenation and Hydrogen Intercalation of Hexagonal Boron Nitride on Ni(111): Reactivity and Electronic Structure, *2D Mater.* **2017**, 4, 035026.

- [163] F. Späth *et al.*, Oxygen Functionalization of Hexagonal Boron Nitride on Ni(111), *Chem. Eur. J.* **2019**, 25, 8884-8893.
- [164] E. M. Freiberger *et al.*, Selective Oxygen and Hydrogen Functionalization of the *h*-BN/Rh(111) Nanomesh, *Chem. Eur. J.* **2021**, 27, 13172-13180.
- [165] E. M. Freiberger, J. Steffen, N. J. Waleska-Wellnhofer, F. Hemauer, V. Schwaab, A. Görling, H.-P. Steinrück and C. Papp, Bromination of 2D Materials, *Nanotechnology* **2024**, 35, 145703.
- [166] P. Willmott, *An Introduction to Synchrotron Radiation*, John Wiley & Sons, Hoboken, New Jersey, 2019.
- [167] J. Falta and T. Möller, *Forschung mit Synchrotronstrahlung*, Vieweg+Teubner, Wiesbaden, 2010.
- [168] G. Shenoy, Basic Characteristics of Synchrotron Radiation, *Struct. Chem.* **2003**, 14, 3-14.
- [169] H. Hertz, Ueber einen Einfluss des Ultravioletten Lichtes auf die Electriche Entladung, *Ann. Phys.* **1887**, 267, 983-1000.
- [170] A. Einstein, Über einen die Erzeugung und Verwandlung des Lichtes betreffenden Heuristischen Gesichtspunkt, *Ann. Phys.* **1905**, 322, 132-148.
- [171] D. Briggs and M. P. Seah, *Practical Surface Analysis: Volume 1 - Auger and X-Ray Photoelectron Spectroscopy*, John Wiley & Sons Ltd, Chichester, 1990.
- [172] H. P. Bonzel and C. Kleint, On the History of Photoemission, *Prog. Surf. Sci.* **1995**, 49, 107-153.
- [173] S. Hüfner, *Photoelectron Spectroscopy: Principles and Applications*, Springer-Verlag, Berlin/Heidelberg/New York, 2003.
- [174] P. v. d. Heide, *X-Ray Photoelectron Spectroscopy: An Introduction to Principles and Practices*, John Wiley & Sons, Inc., Hoboken, New Jersey, 2012.
- [175] M. P. Seah and W. A. Dench, Quantitative Electron Spectroscopy of Surfaces: A Standard Data Base for Electron Inelastic Mean Free Paths in Solids, *Surf. Interface Anal.* **1979**, 1, 2-11.
- [176] C. Papp and H.-P. Steinrück, In Situ High-Resolution X-Ray Photoelectron Spectroscopy – Fundamental Insights in Surface Reactions, *Surf. Sci. Rep.* **2013**, 68, 446-487.
- [177] L. S. Cederbaum and W. Domcke, A Many-Body Approach to the Vibrational Structure in Molecular Electronic Spectra. I. Theory, *J. Chem. Phys.* **1976**, 64, 603-611.
- [178] S. J. Osborne *et al.*, The Vibrationally Resolved C 1s Core Photoelectron Spectra of Methane and Ethane, *J. Chem. Phys.* **1997**, 106, 1661-1668.
- [179] H.-P. Steinrück, T. Fuhrmann, C. Papp, B. Tränkenschuh and R. Denecke, A Detailed Analysis of Vibrational Excitations in X-Ray Photoelectron Spectra of Adsorbed Small Hydrocarbons, *J. Chem. Phys.* **2006**, 125, 204706.
- [180] L. J. Sæthre, O. Sværen, S. Svensson, S. Osborne, T. D. Thomas, J. Jauhiainen and S. Aksela, High-Resolution C 1s Photoelectron Spectra of Methane, Ethene, Propene, and 2-Methylpropene, *Phys. Rev. A* **1997**, 55, 2748-2756.
- [181] D. A. Shirley, High-Resolution X-Ray Photoemission Spectrum of the Valence Bands of Gold, *Phys. Rev. B* **1972**, 5, 4709-4714.
- [182] S. Tougaard, Quantitative Analysis of the Inelastic Background in Surface Electron Spectroscopy, *Surf. Interface Anal.* **1988**, 11, 453-472.
- [183] G. H. Major, N. Fairley, P. M. A. Sherwood, M. R. Linfood, J. Terry, V. Fernandez and K. Artyushkova, Practical Guide for Curve Fitting in X-Ray Photoelectron Spectroscopy, *J. Vac. Sci. Technol. A* **2020**, 38, 061203.

- [184] S. Doniach and M. Sunjic, Many-Electron Singularity in X-Ray Photoemission and X-Ray Line Spectra from Metals, *J. Phys. C: Solid State Phys.* **1970**, 3, 285.
- [185] K. Oura, V. G. Lifshits, A. A. Saranin, A. V. Zotov and M. Katayama, *Surface Science: An Introduction*, Springer-Verlag, Berlin/Heidelberg, 2003.
- [186] J. W. Niemantsverdriet, *Spectroscopy in Catalysis*, WILEY-VCH, Weinheim, 2007.
- [187] J. Stöhr, *NEXAFS Spectroscopy*, Springer, Berlin/Heidelberg, 1992.
- [188] G. Hähner, Near Edge X-Ray Absorption Fine Structure Spectroscopy as a Tool to Probe Electronic and Structural Properties of Thin Organic Films and Liquids, *Chem. Soc. Rev.* **2006**, 35, 1244-1255.
- [189] J. Stöhr and R. Jaeger, Absorption-Edge Resonances, Core-Hole Screening, and Orientation of Chemisorbed Molecules: CO, NO, and N₂ on Ni(100), *Phys. Rev. B* **1982**, 26, 4111-4131.
- [190] S. D. Barrett, C. A. Lucas and R. Raval, *Photon Spectroscopies*, in *Surface and Interface Science: Concepts and Methods*, edited by K. Wandelt (WILEY-VCH, Weinheim, 2012), pp. 311-369.
- [191] G. Ertl and J. Küppers, *Low Energy Electrons and Surface Chemistry*, VCH, Weinheim, 1985.
- [192] C. Davisson and L. H. Germer, The Scattering of Electrons by a Single Crystal of Nickel, *Nature* **1927**, 119, 558-560.
- [193] T. Fauster, L. Hammer, K. Heinz and A. Schneider, *Surface Physics: Fundamentals and Methods*, De Gruyter Oldenbourg, Berlin/Boston, 2020.
- [194] K. Heinz, *Low-Energy Electron Diffraction (LEED)*, in *Surface and Interface Science: Concepts and Methods*, edited by K. Wandelt (WILEY-VCH, Weinheim, 2012), pp. 93-150.
- [195] H. Ohtani, M. A. Van Hove and G. A. Somorjai, LEED Intensity Analysis of the Surface Structures of Pd(111) and of CO Adsorbed on Pd(111) in a ($\sqrt{3} \times \sqrt{3}$)R30° Arrangement, *Surf. Sci.* **1987**, 187, 372-386.
- [196] W. Braun, H.-P. Steinrück and G. Held, The Surface Geometry of Carbonmonoxide and Hydrogen Co-Adsorbed on Ni{111}, *Surf. Sci.* **2005**, 574, 193-204.
- [197] J. C. Vickerman and I. S. Gilmore, *Surface Analysis: The Principle Techniques*, John Wiley & Sons Ltd, Chichester, 2009.
- [198] M. Kinne, Dissertation, Friedrich-Alexander-Universität Erlangen-Nürnberg, 2004.
- [199] C. Gleichweit, Dissertation, Friedrich-Alexander-Universität Erlangen-Nürnberg, 2015.
- [200] Helmholtz-Zentrum Berlin für Materialien und Energie, The Plane Grating Monochromator Beamline U49/2 PGM1 at BESSY II, *JLSRF* **2016**, 2, A72.
- [201] S. H. Oh and J. E. Carpenter, Platinum-Rhodium Synergism in Three-Way Automotive Catalysts, *J. Catal.* **1986**, 98, 178-190.
- [202] M. Shelef and G. W. Graham, Why Rhodium in Automotive Three-Way Catalysts?, *Catal. Rev.* **1994**, 36, 433-457.
- [203] A. Haryanto, S. Fernando, N. Murali and S. Adhikari, Current Status of Hydrogen Production Techniques by Steam Reforming of Ethanol: A Review, *Energy Fuels* **2005**, 19, 2098-2106.
- [204] A. Resta *et al.*, Step Enhanced Dehydrogenation of Ethanol on Rh, *Surf. Sci.* **2008**, 602, 3057-3063.
- [205] M. Li, W. Guo, R. Jiang, L. Zhao, X. Lu, H. Zhu, D. Fu and H. Shan, Density Functional Study of Ethanol Decomposition on Rh(111), *J. Phys. Chem. C* **2010**, 114, 21493-21503.
- [206] D. E. Resasco and G. L. Haller, Novel Rhodium/Titania and Iridium/Titania Catalysts for n-Butane Isomerization and Dehydrogenation, *J. Phys. Chem.* **1984**, 88, 4552-4556.

- [207] O. A. Ferretti, G. J. Siri, F. Humblot, J. P. Candy, B. Didillon and J. M. Basset, Improvements in Selectivity and Stability of Rh Catalysts Modified by SnBu₄. Dehydrogenation of Isobutane to Isobutene, *React. Kinet. Catal. Lett.* **1998**, 63, 115-120.
- [208] N. Raman *et al.*, Highly Effective Propane Dehydrogenation Using Ga–Rh Supported Catalytically Active Liquid Metal Solutions, *ACS Catal.* **2019**, 9, 9499-9507.
- [209] A. M. Baró and H. Ibach, Thermal Evolution and Decomposition of Ethylene on Pt(111), *J. Chem. Phys.* **1981**, 74, 4194-4199.
- [210] T. A. Land, T. Michely, R. J. Behm, J. C. Hemminger and G. Comsa, Direct Observation of Surface Reactions by Scanning Tunneling Microscopy: Ethylene→Ethylidyne→Carbon Particles→Graphite on Pt(111), *J. Chem. Phys.* **1992**, 97, 6774-6783.
- [211] H. Gabasch, K. Hayek, B. Klötzer, A. Knop-Gericke and R. Schlögl, Carbon Incorporation in Pd(111) by Adsorption and Dehydrogenation of Ethene, *J. Phys. Chem. B* **2006**, 110, 4947-4952.
- [212] L. V. Moskaleva, H. A. Aleksandrov, D. Basaran, Z.-J. Zhao and N. Rösch, Ethylidyne Formation from Ethylene over Pd(111): Alternative Routes from a Density Functional Study, *J. Phys. Chem. C* **2009**, 113, 15373-15379.
- [213] S. Lizzit and A. Baraldi, High-Resolution Fast X-Ray Photoelectron Spectroscopy Study of Ethylene Interaction with Ir(111): From Chemisorption to Dissociation and Graphene Formation, *Catal. Today* **2010**, 154, 68-74.
- [214] H. Tetlow, J. Posthuma de Boer, I. J. Ford, D. D. Vvedensky, D. Curcio, L. Omiciuolo, S. Lizzit, A. Baraldi and L. Kantorovich, Ethylene Decomposition on Ir(111): Initial Path to Graphene Formation, *Phys. Chem. Chem. Phys.* **2016**, 18, 27897-27909.
- [215] R. J. Koestner, M. A. Van Hove and G. A. Somorjai, A LEED Crystallography Study of the (2×2)-C₂H₃ Structure obtained after Ethylene Adsorption on Rh(111), *Surf. Sci.* **1982**, 121, 321-337.
- [216] R. J. Levis, L. A. Delouise, E. J. White and N. Winograd, Defect Induced Surface Chemistry: A Comparison of the Adsorption and Thermal Decomposition of C₂H₄ on Rh{111} and Rh{331}, *Surf. Sci.* **1990**, 230, 35-46.
- [217] H. J. Borg, R. M. van Hardeveld and J. W. Niemantsverdriet, Mechanism of the Conversion of Ethene to Ethylidyne on Rhodium(111): Evidence for a Vinylic Intermediate, *J. Chem. Soc., Faraday Trans.* **1995**, 91, 3679-3684.
- [218] M. J. Calhorda, P. E. M. Lopes and C. M. Friend, Theoretical Studies of Ethylene Adsorption and Oxidation on Clean and Oxygen Covered Rhodium (111), *J. Mol. Catal. A Chem.* **1995**, 97, 157-171.
- [219] R. M. van Hardeveld, A. J. G. W. Schmidt and J. W. Niemantsverdriet, Surface Reactions of Nitrogen Oxide and Ethylene on Rhodium (111), *Catal. Lett.* **1996**, 41, 125-131.
- [220] D. C. Papageorgopoulos, Q. Ge and D. A. King, Kinetics of Ethylene Conversion to Ethylidyne on Rh{111} from Laser-Induced Thermal Desorption, *Surf. Sci.* **1998**, 397, 13-22.
- [221] A. J. Slavin, B. E. Bent, C. T. Kao and G. A. Somorjai, Thermal Fragmentation of Ethylene on the Rh(100) Single Crystal Surface in the Temperature Range of 200–800 K, *Surf. Sci.* **1988**, 206, 124-144.
- [222] J. N. Andersen, A. Beutler, S. L. Sorensen, R. Nyholm, B. Setlik and D. Heskett, Vibrational Fine Structure in the C 1s Core Level Photoemission of Chemisorbed Molecules: Ethylene and Ethylidyne on Rh(111), *Chem. Phys. Lett.* **1997**, 269, 371-377.

- [223] M. Wiklund, A. Jaworowski, F. Strisland, A. Beutler, A. Sandell, R. Nyholm, S. L. Sorensen and J. N. Andersen, Vibrational Fine Structure in the C 1s Photoemission Spectrum of the Methoxy Species Chemisorbed on Cu(100), *Surf. Sci.* **1998**, 418, 210-218.
- [224] M. Wiklund, A. Beutler, R. Nyholm and J. N. Andersen, Vibrational Analysis of the C 1s Photoemission Spectra from Pure Ethylidyne and Ethylidyne Coadsorbed with Carbon Monoxide on Rh(111), *Surf. Sci.* **2000**, 461, 107-117.
- [225] H. Wang, Y. Zhao, Y. Xie, X. Ma and X. Zhang, Recent Progress in Synthesis of Two-Dimensional Hexagonal Boron Nitride, *J. Semicond.* **2017**, 38, 031003.
- [226] S. Berner *et al.*, Boron Nitride Nanomesh: Functionality from a Corrugated Monolayer, *Angew. Chem. Int. Ed.* **2007**, 46, 5115-5119.
- [227] O. Bunk, M. Corso, D. Martocchia, R. Herger, P. R. Willmott, B. D. Patterson, J. Osterwalder, J. F. van der Veen and T. Greber, Surface X-Ray Diffraction Study of Boron-Nitride Nanomesh in Air, *Surf. Sci.* **2007**, 601, L7-L10.
- [228] L. H. de Lima, T. Greber and M. Muntwiler, The True Corrugation of a h-BN Nanomesh Layer, *2D Mater.* **2020**, 7, 035006.
- [229] G. Dong, E. B. Fourné, F. C. Tabak and J. W. M. Frenken, How Boron Nitride Forms a Regular Nanomesh on Rh(111), *Phys. Rev. Lett.* **2010**, 104, 096102.
- [230] A. P. Farkas, P. Török, F. Solymosi, J. Kiss and Z. Kónya, Investigation of the Adsorption Properties of Borazine and Characterisation of Boron Nitride on Rh(111) by Electron Spectroscopic Methods, *Appl. Surf. Sci.* **2015**, 354, 367-372.
- [231] B. V. Andryushechkin, T. V. Pavlova and K. N. Eltsov, Adsorption of Halogens on Metal Surfaces, *Surf. Sci. Rep.* **2018**, 73, 83-115.
- [232] K. E. Hermann (FHI) and M. A. Van Hove (HKBU), LEEDpat, Version 4.3, Berlin/Hongkong, 2022.
- [233] E. M. Freiburger, J. Steffen, N. J. Waleska-Wellnhofer, A. Harrer, F. Hemauer, V. Schwaab, A. Göring, H.-P. Steinrück and C. Papp, Cover Feature: Bromine Adsorption and Thermal Stability on Rh(111): A Combined XPS, LEED and DFT Study (ChemPhysChem 22/2023), *ChemPhysChem* **2023**, 24, e202300745.
- [234] R. Khan, R. Nakagawa, B. Campeon and Y. Nishina, A Simple and Robust Functionalization of Graphene for Advanced Energy Devices, *ACS Appl. Mater. Interfaces* **2020**, 12, 12736-12742.

9 Danksagung

Abschließend möchte ich mich herzlichst bei allen bedanken, die direkt oder indirekt zum Gelingen dieser Arbeit beigetragen haben:

Mein besonderer Dank gilt meinem Doktorvater Herrn Prof. Dr. Christian Papp, der mich schon in meinem Bachelor-Studium so sehr für die UHV-Technik, Synchrotronstrahlung und Oberflächenwissenschaft begeistern konnte, dass ich mich alternativlos für die PC II entschieden habe. Christian, Du warst für mich als Ansprechpartner immer zur Stelle und hast mich ansonsten oft "machen lassen", so dass ich eigene Ideen, Selbstständigkeit und nicht zuletzt Selbstvertrauen entwickeln konnte. Vielen Dank für Deine Unterstützung und Dein Vertrauen!

Auch Herrn Prof. Dr. Hans-Peter Steinrück, der mir in den letzten Jahren vielerlei spannende Möglichkeiten eröffnet hat und maßgeblich an der Betreuung meiner Promotion beteiligt war, möchte ich meinen besonderen Dank aussprechen. Ich bin sehr froh, dass ich Teil Ihres Lehrstuhls sein durfte, der sich dank Ihnen durch wissenschaftlichen Anspruch und zugleich eine wunderbare Arbeitsatmosphäre auszeichnet!

Ohne die tatkräftige und stets zuverlässige Hilfe meiner aktuellen und ehemaligen Arbeitskollegen der „Sync-Gruppe“ wäre diese Promotion zum Scheitern verurteilt gewesen. Ob im Labor in Erlangen oder in besonderem Maße am Synchrotron in Berlin, ohne sie wäre der Umgang mit den UHV-Anlagen und die Daten-Acquisition nicht möglich gewesen. Daher möchte ich Natalie Waleska-Wellnhofer, Anton Harrer, Felix Hemauer, Valentin Schwaab, Johann Steinhauer, Fabian Düll, Phiona Bachmann, Udo Bauer und Florian Späth für die wunderbare Zusammenarbeit danken. Besonders Natalie hat mir unzählige Tagungen, BESSY-Aufenthalte und Auslands-Trips durch Ihre Unternehmungslust und Spontanität versüßt.

Auch möchte ich Herrn Prof. Dr. Andreas Görling und Herrn Dr. Julien Steffen vom Lehrstuhl für Theoretische Chemie für eine äußerst fruchtbare Kollaboration danken!

Die Arbeit mit UHV-Techniken schließt naturgemäß den ein oder anderen Rückschlag ein. Bei Reparaturen oder der Umsetzung von neuen Ideen standen mir unser Ingenieur Bernd Kreß, unser Elektroniker Hans-Peter Bäumler und die fleißigen Mitglieder unserer Werkstatt, Friedhold Wölfel (Leitung), Thomas Hofmann, Bernd Hofmann, Werner Höfler, Hussein Alsaedi und Viola Ziegler, stets zur Seite, wofür ich mich gar nicht genug bedanken kann.

Der ansonsten stets reibungslose Ablauf am Lehrstuhl ist unserem akademischen Direktor Dr. Florian Maier und unserem akademischen Oberrat Dr. Andreas Bayer, unseren Sekretärinnen Susana Kreß und Andrea Meixner-Wolf, unserer System-Administration Norman Anja Schmidt und unseren technischen Angestellten Andrea Buchner, Gertrud Weiß und Martin Kolacyak zu verdanken, ohne die wir wohl aufgeschmissen wären.

Während meiner Promotion wurde ich zudem zwei Jahre lang durch das Kekulé-Stipendium des Fonds der Chemischen Industrie finanziell unterstützt. Dafür möchte ich mich beim Verband der Chemischen Industrie bedanken.

Zu guter Letzt möchte ich meinen Eltern Petra Freiberger und Martin Lüttke meinen Dank für ihre allgegenwärtige finanzielle und emotionale Unterstützung aussprechen. Meinem Ehemann Markus Freiberger, der mich seit meiner Schulzeit in guten wie in schlechten Zeiten wie kein anderer stützt, danke ich ganz besonders. Ein Dokortitel ist eine feine Sache, aber wahrlich glücklich bin ich nur an Deiner Seite!

10 List of Publications

- 1 E. M. Freiberger, F. Düll, P. Bachmann, J. Steinhauer, F. J. Williams, H.-P. Steinrück and C. Papp, *h*-BN in the Making: The Surface Chemistry of Borazine on Rh(111), *J. Chem. Phys.* **2024**, 160, 154706.
- 2 A. Ceccatto, E. M. Freiberger, N. J. Waleska-Wellnhofer, S. Jaekel, D. J. Mowbray, C. Papp, H.-P. Steinrück and A. de Siervo, Engineering Large Nanoporous Networks with Size and Shape Selected by Appropriate Precursors, *Carbon* **2024**, 221, 118945.
- 3 E. M. Freiberger, J. Steffen, N. J. Waleska-Wellnhofer, F. Hemauer, V. Schwaab, A. Görling, H.-P. Steinrück and C. Papp, Bromination of 2D Materials, *Nanotechnology* **2024**, 35, 145703.
- 4 R. Eschenbacher, F. Hemauer, E. Franz, A. Leng, V. Schwaab, N. J. Waleska-Wellnhofer, E. M. Freiberger, L. Fromm, T. Xu, A. Görling, A. Hirsch, H.-P. Steinrück, C. Papp, O. Brummel and J. Libuda, Au Catalyzed Energy Release in a Molecular Solar Thermal (MOST) System: A Combined Liquid-Phase and Surface Science Study, *ChemPhotoChem* **2024**, 8, e202300155.
- 5 N. J. Waleska-Wellnhofer, E. M. Freiberger, F. Hemauer, V. Schwaab and C. Papp, Nano-SMSI on Bimetallic FePt Clusters, *J. Phys. Chem. C* **2023**, 127, 38, 18926-18934.
- 6 E. M. Freiberger, J. Steffen, N. J. Waleska-Wellnhofer, A. Harrer, F. Hemauer, V. Schwaab, A. Görling, H.-P. Steinrück and C. Papp, Bromine Adsorption and Thermal Stability on Rh(111): A Combined XPS, LEED and DFT Study, *ChemPhysChem* **2023**, 24, e202300510.
- 7 F. Hemauer, D. Krappmann, V. Schwaab, Z. Hussain, E. M. Freiberger, N. J. Waleska-Wellnhofer, E. Franz, F. Hampel, O. Brummel, J. Libuda, A. Hirsch, H.-P. Steinrück and C. Papp, Surface Science and Liquid Phase Investigations of Oxanorbornadiene/Oxaquadricyclane Ester Derivatives as Molecular Solar Thermal Energy Storage Systems on Pt(111), *J. Chem. Phys.* **2023**, 159, 074703.
- 8 V. Schwaab, F. Hemauer, E. M. Freiberger, N. J. Waleska-Wellnhofer, H.-P. Steinrück and C. Papp, Liquid Organic Hydrogen Carriers: Model Catalytic Studies on the

- Thermal Dehydrogenation of 1-Cyclohexylethanol on Pt(111), *J. Phys. Chem.* **2023**, 127, 23, 11058-11066.
- 9 F. Hemauer, V. Schwaab, E. M. Freiberger, N. J. Waleska, A. Leng, C. Weiß, J. Steinhauer, F. Düll, P. Bachmann, A. Hirsch, H.-P. Steinrück and C. Papp, Surface Studies on the Energy Release of the MOST System 2-Carboxy-3-phenyl-norbornadiene/Quadricyclane (PENBD/PEQC) on Pt(111) and Ni(111), *Chem. Eur. J.* **2023**, 29, e202203759.
- 10 M. Freiberger, I. Solymosi, E. M. Freiberger, A. Hirsch, M. E. Pérez-Ojeda and T. Drewello, A molecular Popeye: Li⁺@C₆₀ and its Complexes with [n]Cycloparaphenylenes, *Nanoscale* **2023**, 15, 5665-5670.
- 11 E. M. Freiberger, F. Düll, C. Wichmann, U. Bauer, H.-P. Steinrück and C. Papp, A High-Resolution X-Ray Photoelectron Spectroscopy Study on the Adsorption and Reaction of Ethylene on Rh(111), *Chem. Phys. Lett.* **2022**, 797, 139595.
- 12 H. H. Ding, K. R. Yan, B. R. Li, W. P. Hu, L. B. Jia, S. Zareen, E. M. Freiberger, J. M. Huang, J. Hu, Q. Xu, Y. Li, S. F. Yang, C. Z. Li, Y. F. Ye and J. F. Zhu, In Situ Investigation of the Cu/CH₃NH₃PbI₃ Interface in Perovskite Device, *Adv. Mater. Interfaces* **2021**, 8, 2100120.
- 13 E. M. Freiberger, F. Späth, U. Bauer, F. Düll, P. Bachmann, J. Steinhauer, F. Hemauer, N. J. Waleska, V. Schwaab, H.-P. Steinrück and C. Papp, Selective Oxygen and Hydrogen Functionalization of the *h*-BN/Rh(111) Nanomesh, *Chem. Eur. J.* **2021**, 27, 13172.
- 14 J. Steinhauer, P. Bachmann, E. M. Freiberger, U. Bauer, H.-P. Steinrück and C. Papp, Model Catalytic Studies of Liquid Organic Hydrogen Carriers: Indole/Indoline/Octahydroindole on Ni(111), *J. Phys. Chem. C* **2020**, 124, 41 22559-22567.
- 15 F. Düll, E. M. Freiberger, P. Bachmann, J. Steinhauer, and C. Papp, Pt Nanoclusters Sandwiched between Hexagonal Boron Nitride and Nanographene as van der Waals Heterostructures for Optoelectronics, *ACS Appl. Nano Mater.* **2019**, 2, 11, 7019-7024.

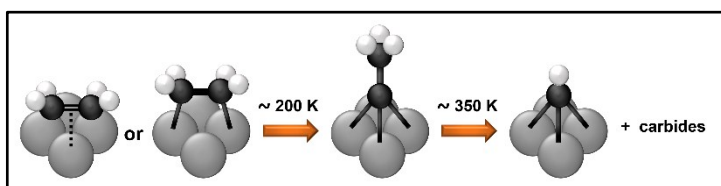
Appendix A: Full Articles [P1] – [P4]

[P1] A High-Resolution X-Ray Photoelectron Spectroscopy Study on the Adsorption and Reaction of Ethylene on Rh(111)

E. M. Freiberger, F. Düll, C. Wichmann, U. Bauer, H.-P. Steinrück and C. Papp

Chem. Phys. Lett. **2022**, 797, 139595, DOI: [10.1016/j.cplett.2022.139595](https://doi.org/10.1016/j.cplett.2022.139595).

E. M. Freiberger: Data acquisition, data evaluation, data visualization, manuscript preparation, reviewing process.

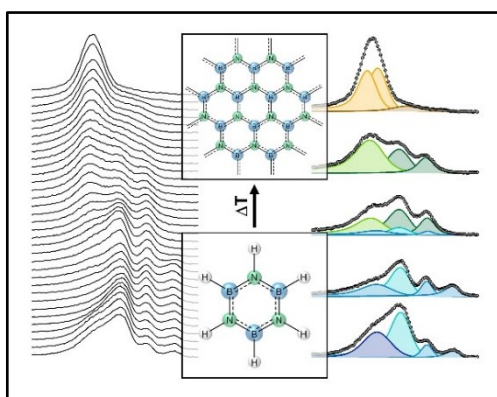


[P2] *h*-BN in the Making: The Surface Chemistry of Borazine on Rh(111)

E. M. Freiberger, F. Düll, P. Bachmann, J. Steinhauer, F. J. Williams, H.-P. Steinrück and C. Papp

J. Chem. Phys. **2024**, 160, 154706, DOI: [10.1063/5.0202431](https://doi.org/10.1063/5.0202431).

E. M. Freiberger: Data acquisition, data evaluation, data visualization, manuscript preparation, reviewing process.



[P3] Bromine Adsorption and Thermal Stability on Rh(111): A Combined XPS, LEED and DFT Study

E. M. Freiberger, J. Steffen, N. J. Waleska-Wellnhofer, A. Harrer, F. Hemauer, V. Schwaab, A. Göring, H.-P. Steinrück and C. Papp

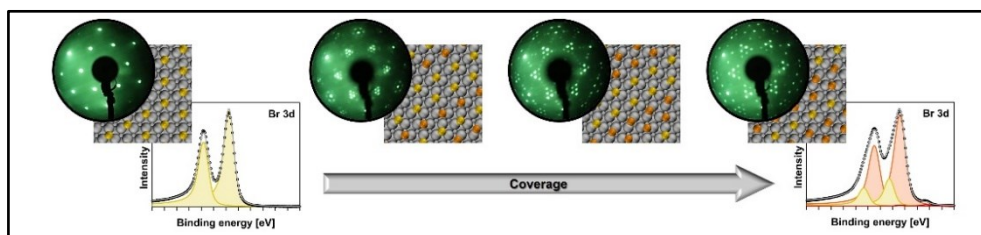
ChemPhysChem **2023**, 24, e202300510, DOI: [10.1002/cphc.202300510](https://doi.org/10.1002/cphc.202300510).

**Cover Feature: Bromine Adsorption and Thermal Stability on Rh(111):
A Combined XPS, LEED and DFT Study (ChemPhysChem 22/2023)**

E. M. Freiberger, J. Steffen, N. J. Waleska-Wellnhofer, A. Harrer, F. Hemauer,
V. Schwaab, A. Görling, H.-P. Steinrück and C. Papp

ChemPhysChem **2023**, 24, e202300745, DOI: [10.1002/cphc.202300745](https://doi.org/10.1002/cphc.202300745).

E. M. Freiberger: Experimental data acquisition, data evaluation, data visualization,
manuscript preparation, reviewing process, cover feature design.



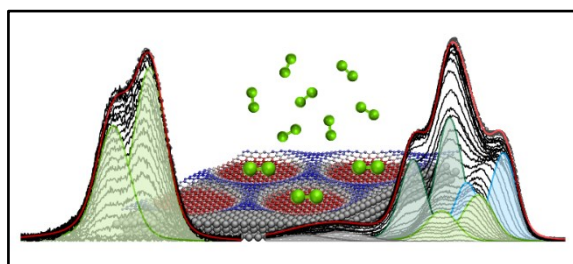
[P4] Bromination of 2D Materials

E. M. Freiberger[†], J. Steffen[†], N. J. Waleska-Wellnhofer, F. Hemauer, V. Schwaab,
A. Görling, H.-P. Steinrück and C. Papp

Nanotechnology **2024**, 35, 145703, DOI: [10.1088/1361-6528/ad1201](https://doi.org/10.1088/1361-6528/ad1201).

E. M. Freiberger: Experimental data acquisition, data evaluation, data visualization,
manuscript preparation, reviewing process.

[†] The authors contributed equally to this work (shared first author).



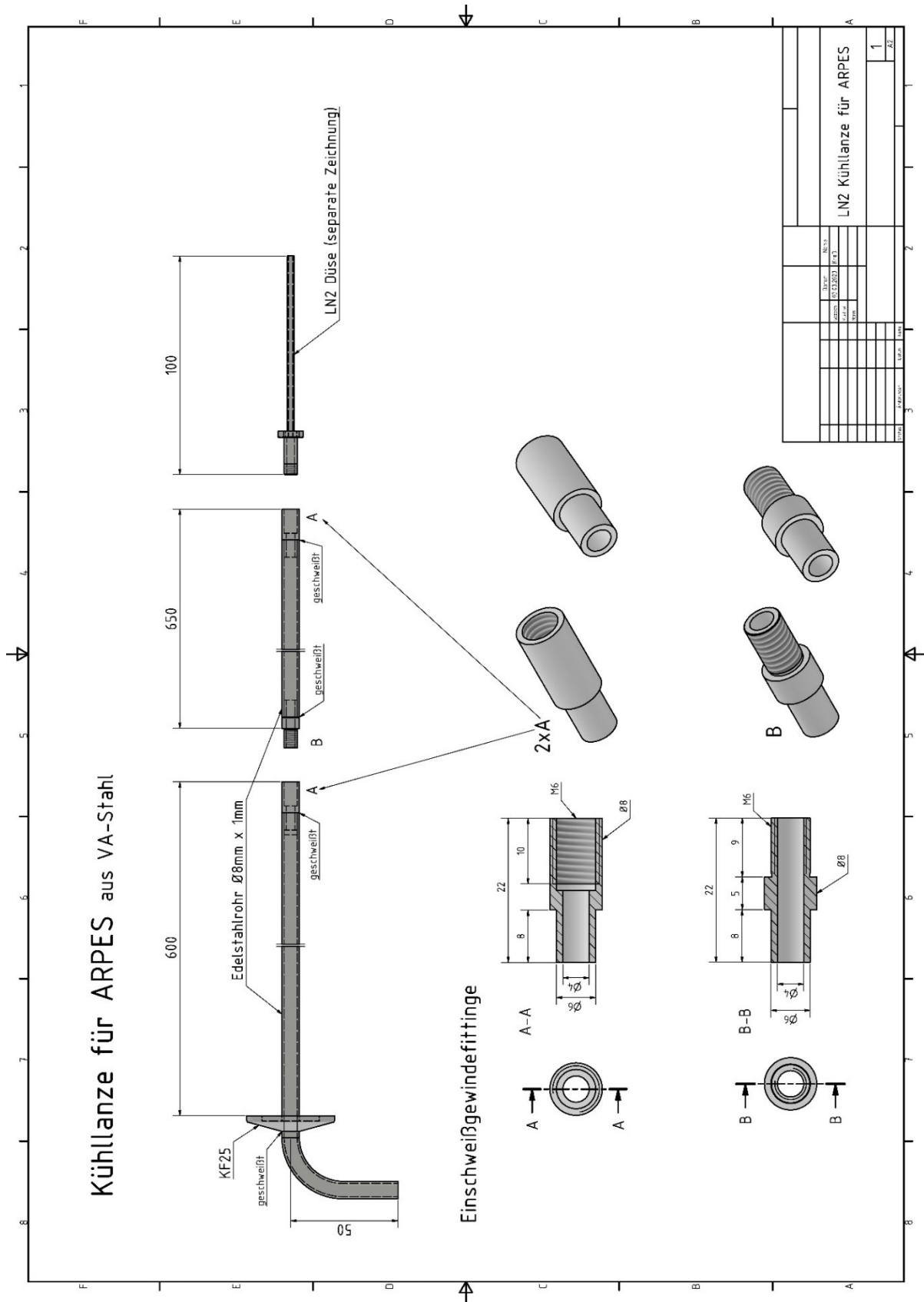


Figure 37. Cooling lance. Drawings by Bernd Kreß.

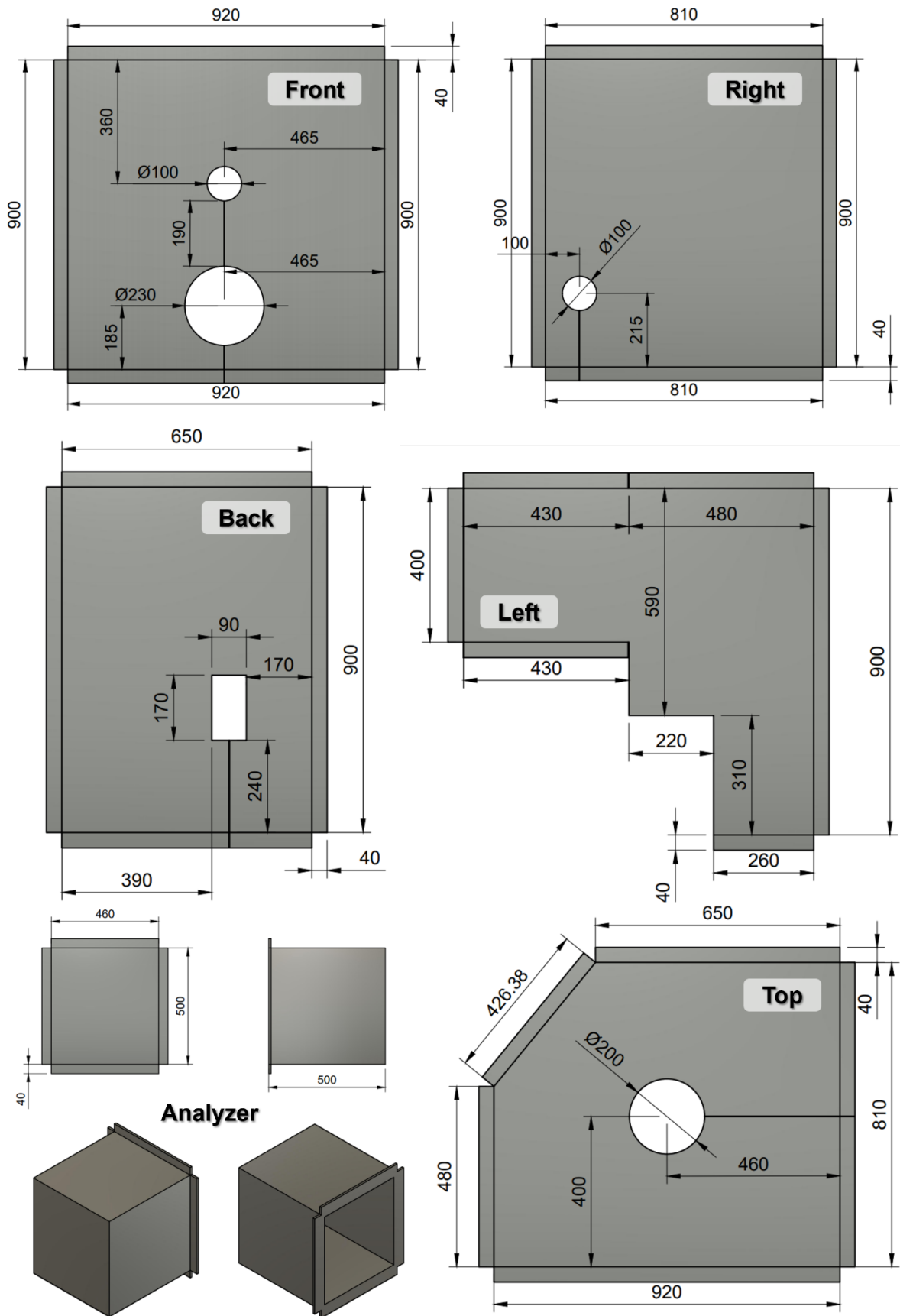


Figure 39. Bakeout blankets for the “ARPES chamber”: Front, right, left, back, top and analyzer. Drawings by Eva Marie Freiburger.

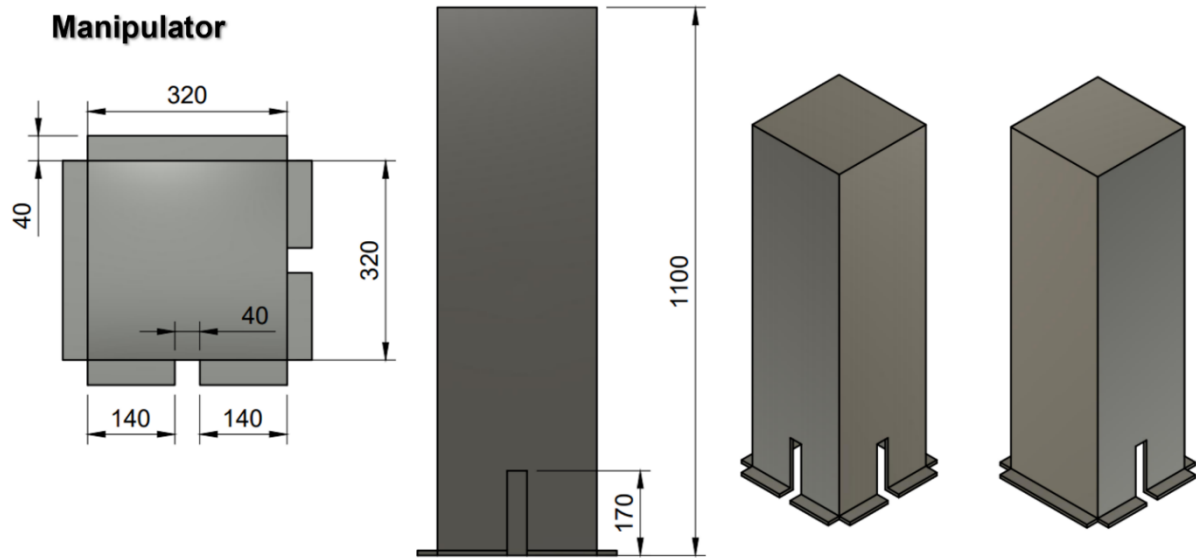


Figure 40. Bakeout blankets for the "ARPES chamber": Manipulator. Drawings by Eva Marie Freiburger.